Peak is caused by increased
sediment access

National Aeronautics and Space Administration

A period of peak subglacial sediment discharge following glacier retreat

Ian A. Delaney (329 A), Surendra Adhikari (329 A)
Jet Propulsion Laboratory, California Institute of Technology

What caused us to think about this?

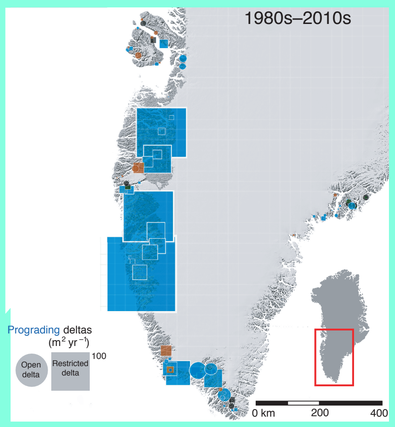

From Bendixen et al., 2018

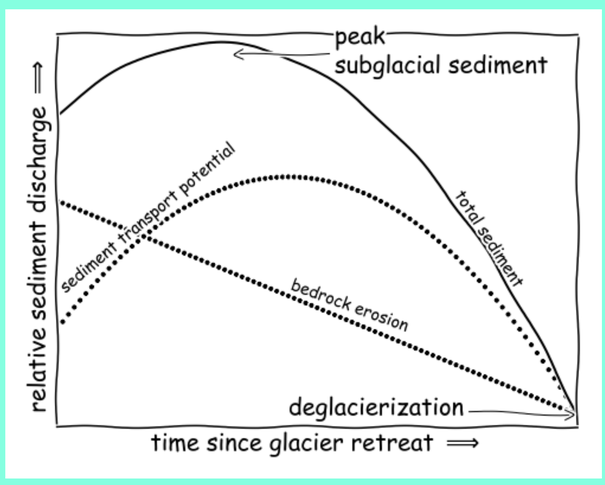

Necessary ingredients

A glacier | Sediment transport | Glacier erosion

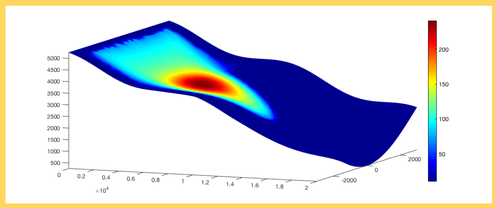

- Created with ISSM using "Higher Order" Physics
- Retreated from steady state
- Parameterized glacier **sliding**, **topography** and **melt**

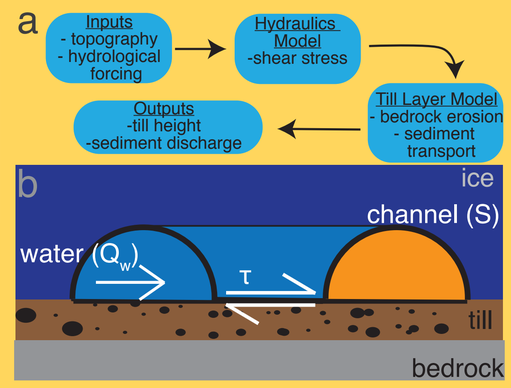

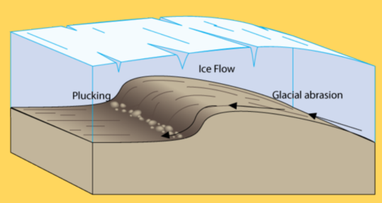

$$\dot{e} = k_g u_b^l$$

Our findings so far

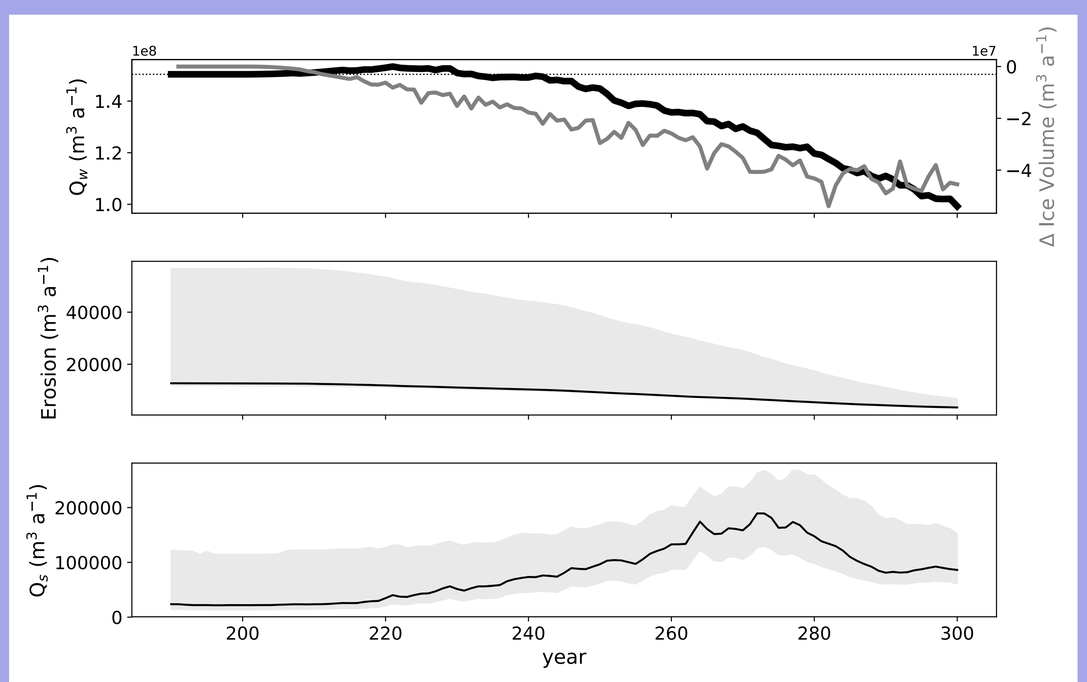

Glacier with bump in its bed

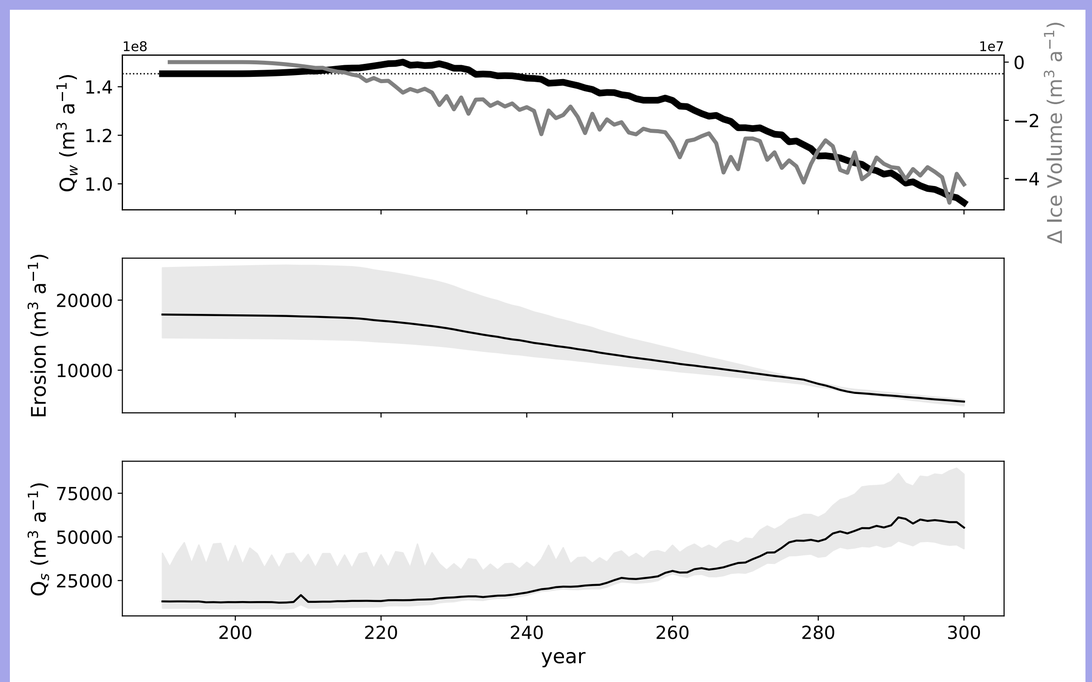

Glacier without bump in its bed

What we think is happening

- Sediment access and rising ELA's seem to be the driver.
- Process respond **differently to different glacier geometries.**

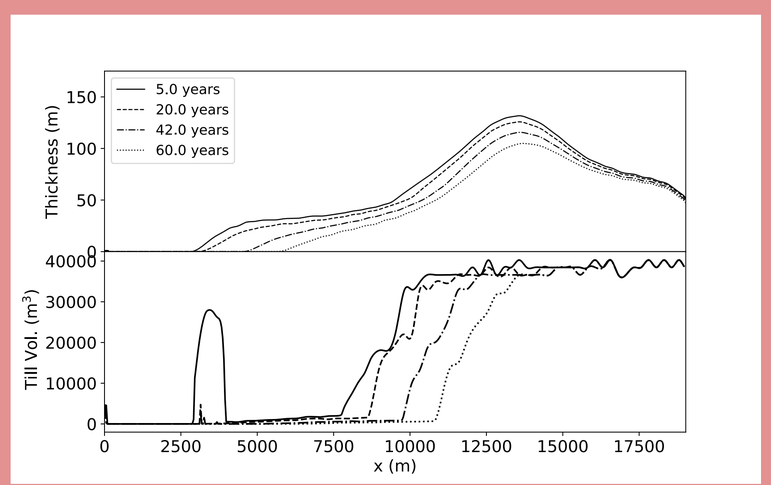

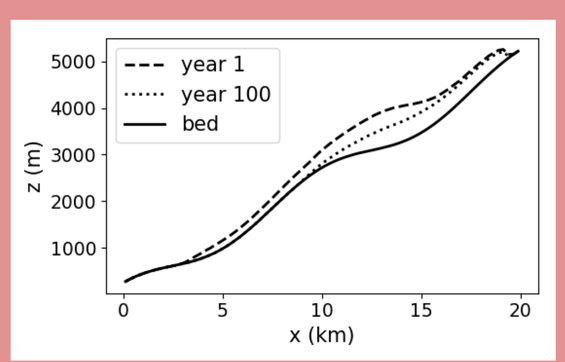

Where will this go?

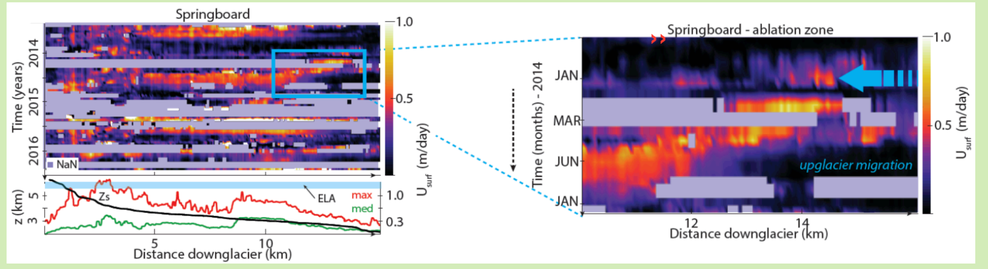

From Adhikari and Avouac

We hope to apply this to "real" glaciers *soon* using measured glacier **velocity and topography** data

National Aeronautics and Space Administration
Jet Propulsion Laboratory
California Institute of Technology
Pasadena, California
www.nasa.gov

Poster No. EB-01

National Aeronautics and Space Administration

Untangling Tectonic and Non-tectonic Signals in Satellite Radar Data Over Tibet

Robert Zinke (329-A)

G. Peltzer (329-A, UCLA), E. J. Fielding (329-A), S. S. Sangha (329-A, UCLA), and C. Liang (Caltech)

Introduction

Differential interferometric synthetic aperture radar (InSAR) can provide continuous maps of the cm/year-scale ground deformation in Tibet resulting from the India–Eurasia tectonic collision. Water vapor, ionospheric effects, and gravitational tides, however, can affect the radar data over short timescales, distorting or even obscuring the tectonic signal of interest. We seek to quantify and ultimately remove the non-tectonic components from our differential radar data in order to determine crustal motion rates across Tibet using Sentinel-1 satellite radar data. These measurements will advance our understanding of earthquake fault behavior and natural hazard.

Tectonic setting

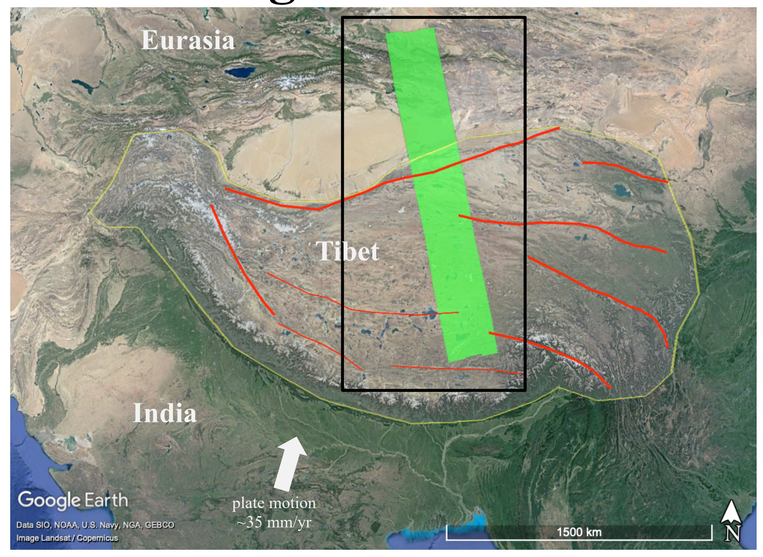

India is colliding with Eurasia at ~3.5 cm/yr, creating the high-altitude Tibetan Plateau (outlined in yellow), and a series of faults (red) along which we will measure tectonic strain accumulation rates. Green rectangle is the InSAR track analyzed below. Black box is the approximate area shown in subsequent figures.

Measured (raw) InSAR signal

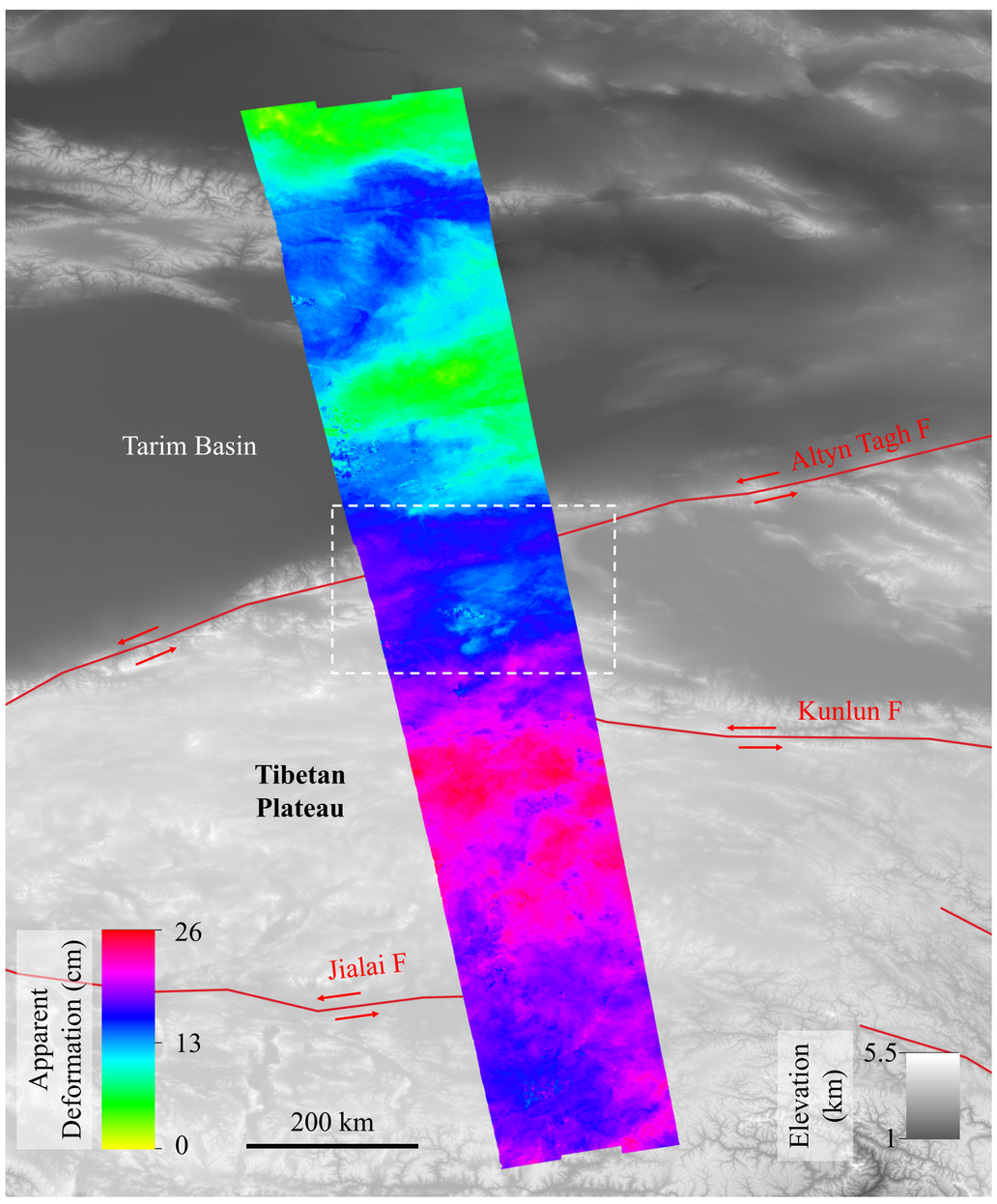

The unwrapped interferogram above shows the total difference in radar phase (apparent deformation) across the region as measured by a single pair of satellite passes 12 days apart. This measured, "raw" signal is influenced by tectonic deformation, atmospheric distortions, and other factors. Background is topography (SRTM digital elevation model). Major faults shown in red. Dashed white box shows subsection used for tropospheric analysis (*lower right*).

Non-tectonic contributions to measured signal

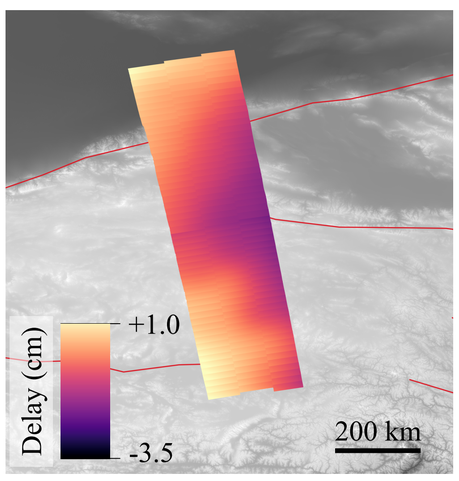

Ionospheric delays (*left*) result from the radar pulse passing through Earth's ionosphere. Delays can be measured by analyzing different parts of the radar spectrum (*Liang et al., 2019*).

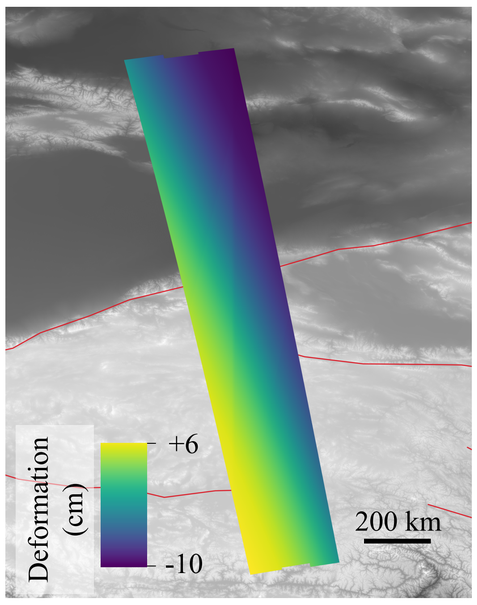

Earth body tides (*right*) are similar to ocean tides, but affect the solid earth. We quantify earth tides using established calculations based on the position of Earth relative to the Sun and Moon.

Tropospheric delays are caused by the presence of atmospheric moisture and gas concentrations. Tropospheric phase delays are usually correlated with topography (*below, right*), and can be removed using published weather models such as ERA-5.

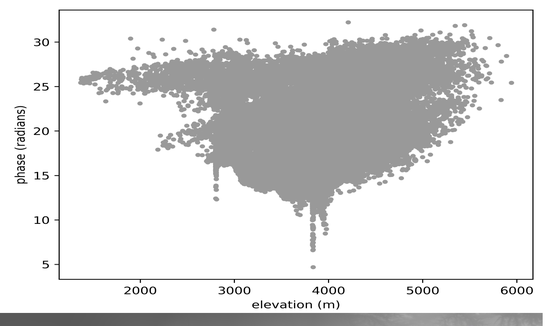

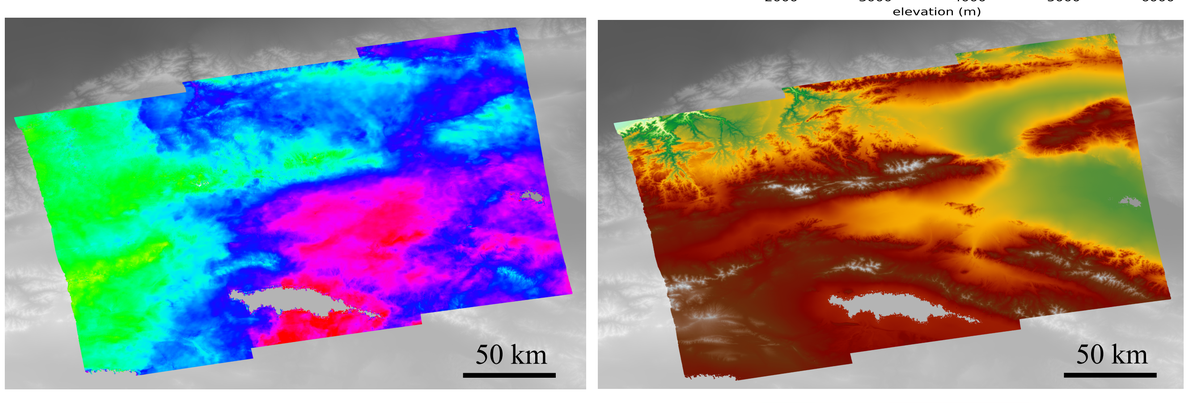

Future directions

- Continue to quantify the relative importance of non-tectonic signals in our InSAR data
- Mitigate or remove those signals using the methods above
- Develop a timeseries of tectonic deformation in Tibet

National Aeronautics and Space Administration

Jet Propulsion Laboratory
California Institute of Technology
Pasadena, California

www.nasa.gov

Poster No. EB-02

National Aeronautics and Space Administration

High-Resolution Maps of Sea Surface Height

A new method applied to the California Current system

Authors: Matthew Archer (329b), Zhijin Li (329b) and Lee Fu (3200)

IN A NUTSHELL

Motivation Satellite altimetry **sea surface height** (**SSH**) data has been the backbone of global oceanography research since the 1980s. However, the spatial resolution of mapped SSH is limited to wavelengths above ~170 km. This limit is imposed by the mapping methodology of AVISO. Motivated by NASA's upcoming SWOT mission and calibration/validation (Cal/Val) phase, our research question was: *how far can we push the resolution of the current altimetry data with a new methodology?*

Methodology To objectively map along-track data, we employ a bespoke variational data assimilation scheme for the California Current system (CCS)

Results The new methodology improves resolution of SSH maps in the CCS by 40%

Impact This high-resolution data will be utilized for Cal/Val of NASA's SWOT mission, and could significantly impact existing estimates of ocean energetics from altimetry.

AVISO (CURRENT)

Archiving, Validation, and Interpretation of Satellite Oceanographic data

2DVAR (NEW)

2-Dimensional Variational Method

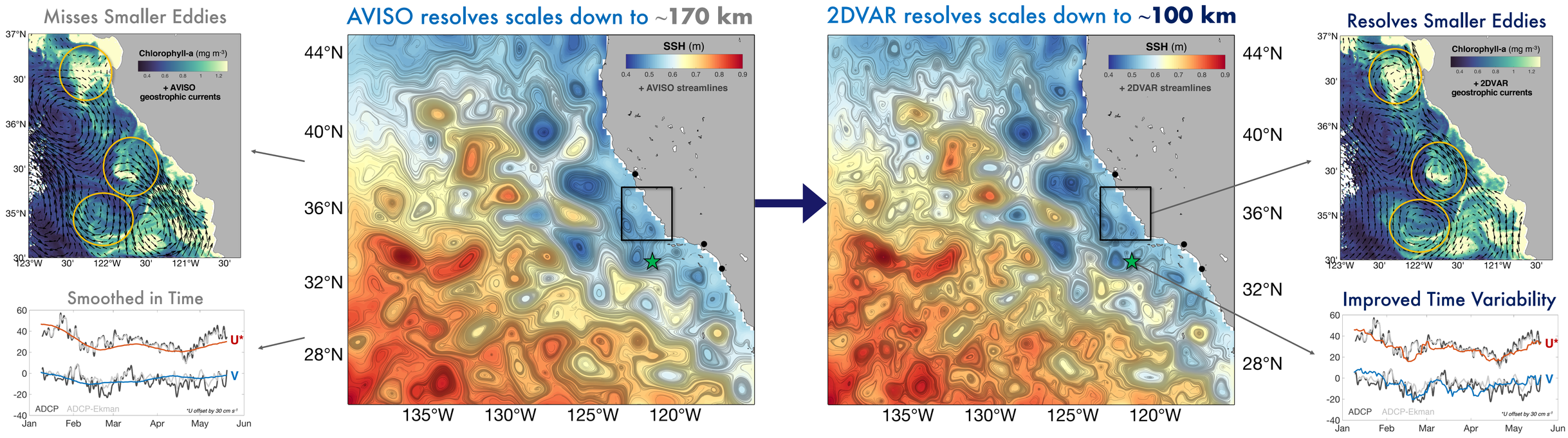

MOTIVATION

- Along-track altimeter measurements of SSH have a resolution of ~65 km
- However, data must be mapped to a regular space-time grid for scientific analysis, and the current methodology (AVISO**)** heavily smooths along-track data, resulting in a resolution of ~170 km
- **Our goal** is *to maximize the resolution of mapped SSH*, while avoiding spurious off-track variance

Cumulative Ground Tracks for 7, 11, 21 days

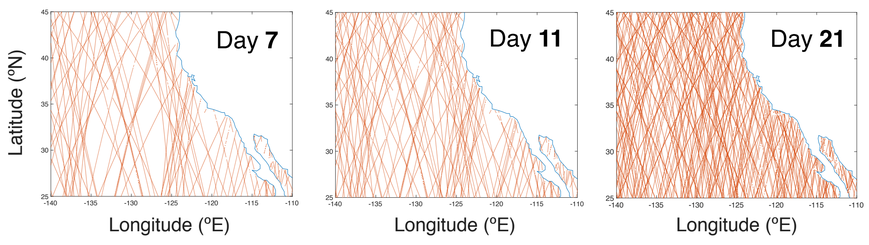

Ground Tracks show the distribution of observations ingested by the mapping algorithms. AVISO uses ± 6 weeks, 2DVAR uses ± 11 days

DATASETS

1 Jan to 31 May, 2018

5 altimeters:
- *Jason-3 (J-3)*
- *Sentinel-3A (S-3A)*
- *SARAL/AltiKa (DP*)*
- *Cryosat-2 (G†)*
- *HaiYang-2A (G†)*

**DP = Drifting phase. †G = Geodetic*

METHODOLOGY

- AVISO (Pujol et al., 2016) and 2DVAR (Li et al., 2016) solve differently for the same least squares solution: the mapped field (x) is equal to a background (x^b) plus observations (y^o), weighted by background (B) and observational (R) error covariance matrices. H is an operator to map grid points to observations.

AVISO: Optimal Interpolation

Minimizes mean squared error

$$x = x^b + BH^T(HBH^T + R)^{-1}(y^o - Hx^b)$$

2DVAR: Variational Assimilation

Minimizes cost function J

$$J(x) = \frac{1}{2}(x - x^b)^T B^{-1}(x - x^b) + \frac{1}{2}(y^o - Hx)^T R^{-1}(y^o - Hx)$$

- **Key improvements in 2DVAR** :
  1. Use of a high-resolution background field rather than the 20-year mean
  2. Regional parameters defined (smaller correlation scales, less along-track smoothing)
  3. Inclusion of representation error, removal of a time correlation function
  4. Computationally more efficient, uses all available observations, easier to add constraints

RESULTS

- 2DVAR retains more fine-scale ocean variability from the along-track data

2DVAR effective resolution shows 40% improvement over AVISO

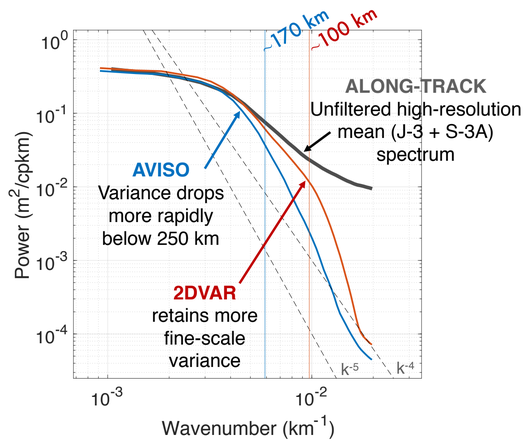

Effective Resolution (Chelton & Schlax, 2003) is the wavelength of half-power between mapped data and unfiltered mean along-track spectrum

2DVAR outperforms AVISO nearly everywhere

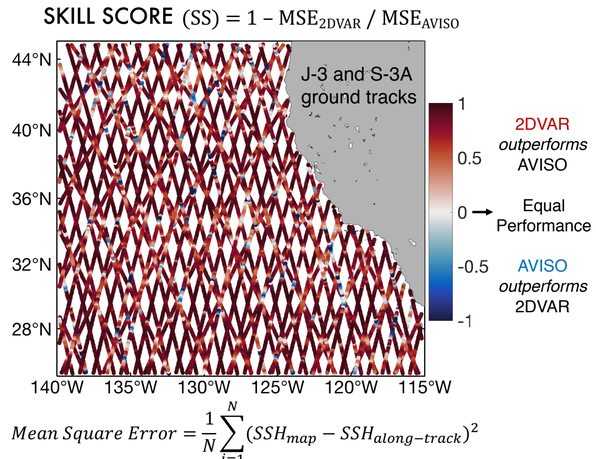

Skill Score provides a quantitative measure of performance between 2DVAR and AVISO, based on the mean square error (MSE) between the maps and along-track measurements

IMPACT & FUTURE WORK

- 2DVAR produces much higher resolution maps – which **will be used in the Cal/Val of NASA's upcoming SWOT mission**
- The resolution increase **significantly impacts scientific research** into eddy fluxes and ocean energetics
- Future work: Explore the information content of the higher resolution maps via dynamical analysis (conservation of PV and a full data assimilating model)

References

Chelton, D. B., and Schlax, M.G. (**2003**). The accuracies of smoothed sea surface height fields constructed from tandem altimeter datasets. *J. Atmos. Oceanic Technol*., 20, 1276-1302.

Li, Z., Zuffada, C., Lowe, S. T., Lee, T., and Zlotnicki, V. (**2016**). Analysis of GNSS-R altimetry for mapping ocean mesoscale sea surface heights using high-resolution model simulations. *IEEE J. of Sel. Top. in App. Earth Obs. and Rem. Sens.*, *9*(10), 4631-4642.

Pujol, M. I., Faugère, Y., Taburet, G., Dupuy, S., Pelloquin, C., Ablain, M., and Picot, N. (**2016**). DUACS DT2014: the new multi-mission altimeter data set reprocessed over 20 years. *Ocean Science*, 12(5).

National Aeronautics and Space Administration

Jet Propulsion Laboratory
California Institute of Technology
Pasadena, California

www.nasa.gov

Poster No. EB-03

National Aeronautics and Space Administration

Towards an improved estimate of mountain glaciers contribution to sea level rise since 1975

Amaury Dehecq (329C), Alex Gardner (329C), Oleg Alexandrov (Ames Center)

Context

Glaciers contribution to sea-level rise: Glaciers retreat contributed to about 1/3 of the observed sea level rise since 1971 (IPCC). However, long term estimates of glaciers volume changes rely on sparse field observations and region-wide satellite observations are available mostly after 2000 (Gardner et al., 2013; Zemp et al., 2019).

Hexagon satellites: Twenty KH-9 satellites, operated by the US National Reconnaissance Office (NRO), were placed in low Earth orbit (~170 km) between 1971 and 1986 (*Burnett*, 2012). They provided a global mapping capability with a 6-meter resolution frame camera (MCS) that collected nadir imagery on photographic film (Fig 1), with an overlap of 70% between adjacent images, enabling stereo reconstruction of the topography. Declassification of the data in 2011 open new possibilities for the observation of long-term glaciers change (*Pieczonka et al.*, 2013; *Maurer et al.*, 2019).

Research Objectives:

- ✓ Develop an automated pipeline to generate Digital Elevation Models (DEM) at 24 m resolution from the raw scanned KH9 film.
- ✓ Compare historical DEMs with recent topography (e.g. ArcticDEM) to estimate glaciers volume changes and contribution to sea level rise over the last 40 years.

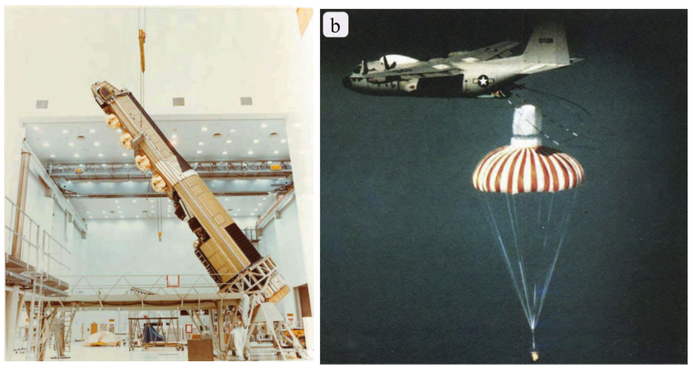

Fig. 1: KH-9 satellite. (Left) KH-9 vehicle during assembly. The canisters of exposed films (gold domes) were periodically ejected and retrieved during descent (Right).

Image preprocessing

Challenges: • Images stored on 18”x9” photographic film, scanned as two 9.5”x9” parts.
• Storing/scanning caused distortion of the film that must be corrected.

Correction of distortion: KH-9 images have 1058 fiduciary marks (crosses, Fig 2 left), or réseau grid, identifying the original image geometry at the time of exposure (*Surazakov & Aizen*, 2010). Each marker is located with subpixel precision by convoluting a cross-like kernel and looking for local regular maxima. The distance of the cross centers to a regular grid yields the image distortion at the réseau grid (Fig 2, right). A Thin-Plate-Spline interpolation is used to estimate and correct the distortion at each pixel.

Image stitching : The left/right images are stitched together using interest-point matching (SIFT) in the area of overlap. Finally the image is cropped to remove the dark bands around the film.

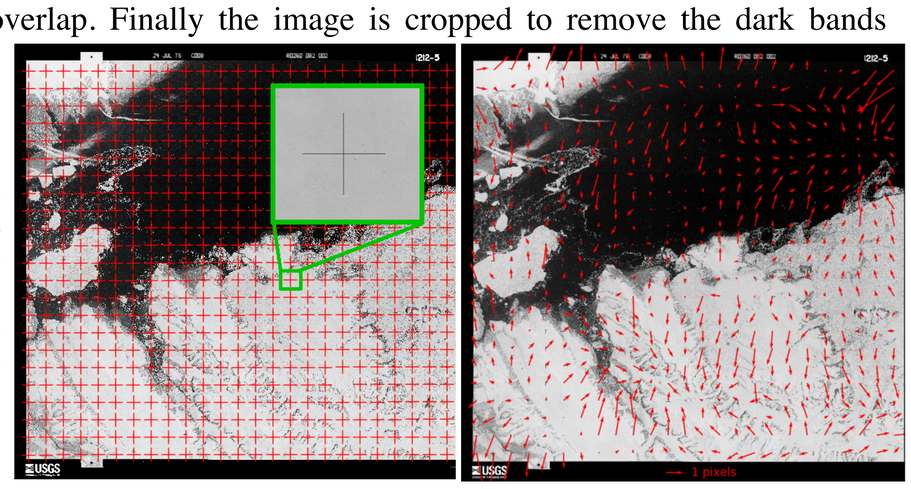

Fig. 2: Identification of the fiducial markers (left) and estimated film distortion (right), after removal of a rotation/scaling for image DZB1212-500082L001001. The fiducials are filled with white noise and the image black edges cropped before the stereo processing.

Stereo processing

From stereo pairs, we generate DEMs using the NASA AMES Stereo Pipeline (Shean et al., 2016).

Challenges: • Images are very crudely geolocated, no existing Ground Control Points (GCPs)
• Satellite position and lens characteristics are unknown/classified.

Solving for camera: (1) An initial camera position/orientation is estimated from the crude corner coordinates provided by the USGS, using a Pinhole camera model (focal length = 12”)
(2) Interest Points are automatically generated in all images. By minimizing the elevation of such points to a reference terrain (e.g. SRTM), we can optimize the unknown camera position/orientation, lens distortion and focal length for each image pair (bundle adjustment).

Topography reconstruction: (1) A disparity map (pixel displacement) is calculated for each image pair, using the Semi-Global Matching algorithm, with 7x7 pixels correlation windows.
(2) A Point-Cloud and DEM are generated from the disparity map using triangulation.
(3) The output DEM is coregistered to a reference DEM using Iterative Closest Point.
The process is ran at 1/2 the resolution to reduce computation time. The output DEM is then used to map-project the images at full resolution, reducing the disparity and improving the correlation.

National Aeronautics and Space Administration
Jet Propulsion Laboratory
California Institute of Technology
Pasadena, California
www.nasa.gov

Results – Application to Alaskan glaciers

Context: Glaciers in Alaska are the largest contributors to sea-level rise over 2006-2016, with an average 0.22 mm/yr (Zemp et al., 2019). Their total estimated volume, 12% of the total glaciers’ volume, has the potential to raise sea level by 51 mm.

Glacier elevation change: Example of application of our methodology to 54 image pairs over South Alaska (Fig 3). The retreat and thinning of the glaciers is clearly visible in red, with thinning reaching 100 m over the 40 year period

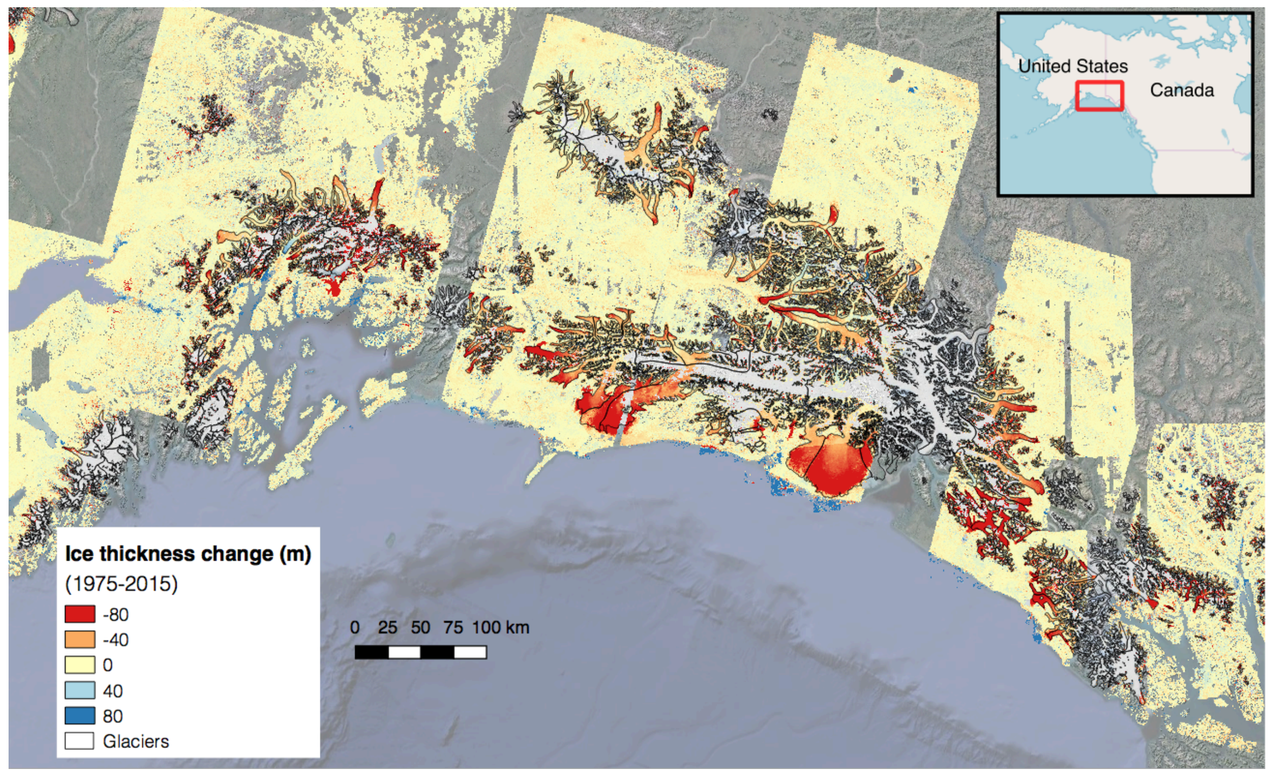

Fig. 3: Elevation change between the KH-9 DEM obtained with our automated workflow and ArcticDEM (WorldView). Large gaps in the observations occur in areas of saturation in high altitude (grey areas).

Volume change: To estimate the total glacier volume/mass change, we calculate an average elevation change by altitude bin (thinning is stronger at low elevation where temperatures are higher) and multiply by the glacier area in that bin (Fig. 4). Volume is converted to mass change using an ice density of 900 kg/m^3 and to sea-level rise equivalent (SLE) assuming an ocean area of 3.62x10^8 km^2.

Results: Alaskan glaciers thinned an average 0.5 m/yr over the 40 year period, twice as much as the global average over 1961-2016 (Zemp et al., 2019).
This is equivalent to a mass loss of 1680 Gt or 5.2 mm SLE.

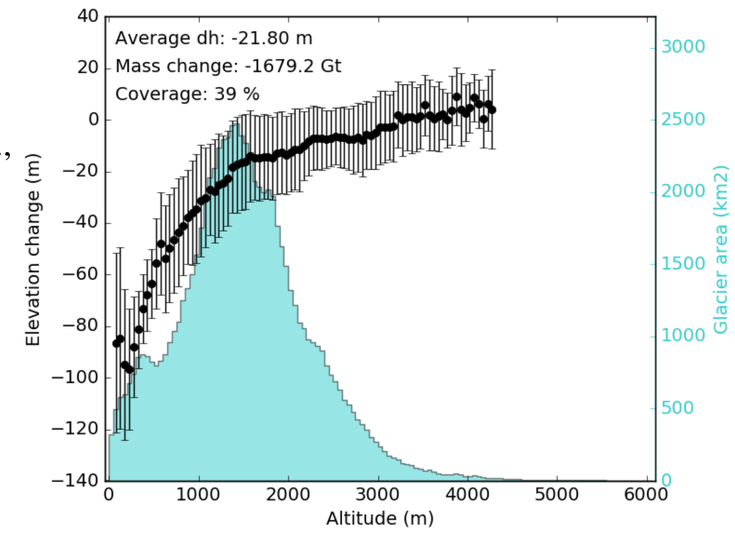

Fig. 4: Average elevation change of Alaskan glaciers with altitude (black curve, error bars represent the interquartile range) and glacier area in each altitude band (blue histogram). Gt (giga-tonne) = 10^{12} kg

Next steps:

- The results were obtained by processing the images at half-resolution. A processing at full resolution, using the previous results to reduce computation time and improve the image correlation should highly increase the coverage of the observations.
- The methodology will be applied to all other glacierized regions of the world in order to estimate the total glacier contribution to sea level rise.

❖ We developed an automated preprocessing workflow able to convert the scanned film into undistorted digital images and Digital Elevation Models. To date >600 images have been processed, with a global coverage of glaciers, which will ultimately provide unprecedented information on glacier mass changes over the last 4 decades.

❖ A first application of the methods to Alaska glacier yield a total mass change of 1680 Gt or 5.2 mm of sea-level rise over 1975-2015. This is larger than any other mountain range in the world.

References: Burnett, M. G. (2012), *Hexagon (KH-9) Mapping Camera Program and Evolution*, 364 pp., Center for the study of National Reconnaissance Chantilly, VA.
Gardner, A.S., Moholdt, G., Cogley, J.G., et al., 2013. A Reconciled Estimate of Glacier Contributions to Sea Level Rise: 2003 to 2009. Science **340**, 852–857.
Maurer, J.M., Schaefer, J.M., Rupper, S., Corley, A., 2019. Acceleration of ice loss across the Himalayas over the past 40 years. Science Advances **5**, eaav7266.
Pieczonka, T., Bolch, T., Junfeng, W. & Shiyin, L. Heterogeneous mass loss of glaciers in the Aksu-Tarim Catchment (Central Tien Shan) revealed by 1976 KH-9 Hexagon and 2009 SPOT-5 stereo imagery. *Remote Sensing of Environment* **130,** 233–244 (2013).
Shean, D.E., Alexandrov, O., Moratto, et al., 2016. An automated, open-source pipeline for mass production of digital elevation models (DEMs) from very-high-resolution commercial stereo satellite imagery. ISPRS Journal of Photogrammetry and Remote Sensing 116, 101–117.
Surazakov, A. & Aizen, V. Positional Accuracy Evaluation of Declassified Hexagon KH-9 Mapping Camera Imagery. *Photogrammetric Engineering & Remote Sensing* **76,** 603–608 (2010).
Zemp, M., Huss, M., Thibert, E., et al., 2019. Global glacier mass changes and their contributions to sea-level rise from 1961 to 2016. Nature 568, 382.

Poster No. EB-04

National Aeronautics and Space Administration

25 years of Antarctic ice shelf melt measured from space

Fernando Paolo (329C) Johan Nilsson (329C) Alex Gardner (329C)

A key limitation in our ability to predict future sea level lies in our insufficient understanding of the processes at the interface between the ice sheet and the ocean. At this boundary, the warming oceans exchange mass and heat with the ice shelves, the floating extensions of the ice sheet that fringe ~75% of the Antarctic continent. These ice shelves act as “dams” for the flow of grounded ice from the continent’s interior towards the sea. As the oceans melt away the ice shelves, their capacity to restrain the flow of glaciers and ice streams is reduced, leading to an acceleration in ice discharge to the ocean. This meltwater production directly changes the properties of the surrounding water masses; freshening the Southern Ocean, impacting the vertical stratification of the water column, and altering local-to-regional circulation.

We are synthetizing over 25 years of satellite observations to estimate the changes in meltwater production (ice-shelf melt rates) since 1992 to present. We incorporate data from ESA’s ERS-1, ERS-2, Envisat and CryoSat-2 radar altimeters (1992-present) and NASA's ICESat laser altimeter (2003-2009) and Operation IceBridge (2009-present), as well as ice velocities derived from Landsat optical imagery (2014-present). We improved the methods for the synthesis of heterogeneous measurements of ice-shelf surface height and uncertainty estimation, and subsequent inversion to ice-shelf melt rates. We are constructing a record of Antarctica-wide meltwater production with unprecedented resolution in time and space.

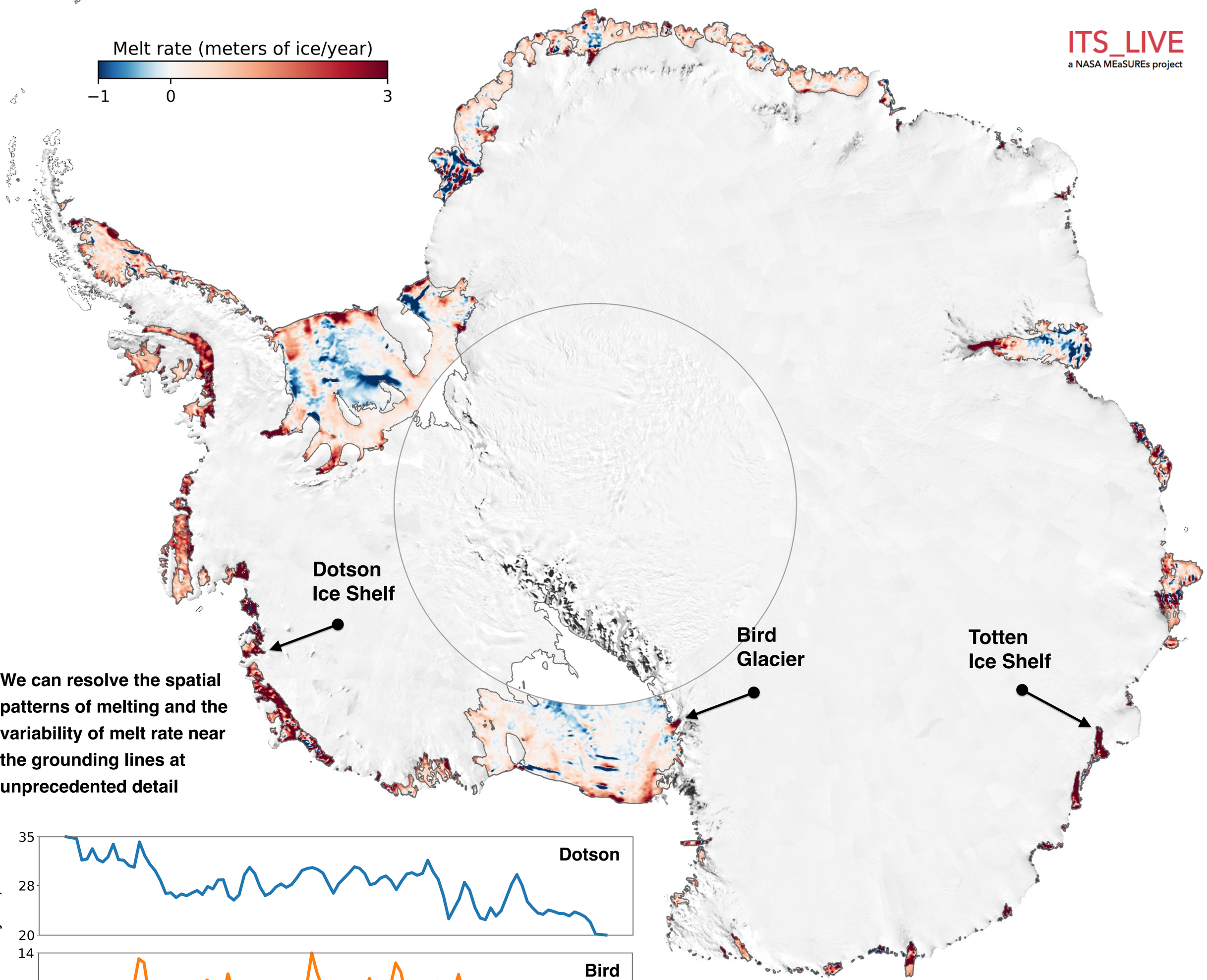

We can resolve the spatial patterns of melting and the variability of melt rate near the grounding lines at unprecedented detail

$$\dot{b} = \frac{\partial H}{\partial t} + \mathbf{u} \cdot \nabla H + H \nabla \cdot \mathbf{u} + \dot{a}$$

where $\dot{b}$ is basal melt rate, $\dot{a}$ is surface accumulation rate, $\frac{\partial H}{\partial t}$ is thickness change, $\mathbf{u} \cdot \nabla H$ is advection of thickness gradient and $H \nabla \cdot \mathbf{u}$ is ice-flow divergence, with $\mathbf{u}$ being ice velocity.

National Aeronautics and Space Administration
Jet Propulsion Laboratory
California Institute of Technology

Poster No. EB-05

National Aeronautics and Space Administration

Relationships between tropical ascent and high cloud fraction changes with warming revealed by perturbation physics experiments in CESM

Kathleen Schiro (329D)

Hui Su (329D), Baird G. Langenbrunner (UC Irvine), Yuan Wang (Caltech), Jonathan H. Jiang (329J), and J. David Neelin (UCLA)

Introduction

Key Research Question: What physical processes are responsible for the large uncertainty in climate model projections of tropical cloud, circulation, and precipitation changes under global warming?

Motivation:

- Uncertainty in global precipitation change under warming ("hydrological sensitivity") strongly coupled to uncertainty in change in outgoing longwave radiation (OLR; Su et al. 2017, *Nat. Comm.*)
- Tropical mean OLR strongly coupled to tropical high clouds

Goals:

1. Identify climate model physics responsible for the large CMIP5 inter-model spread in the response of high clouds, circulation, and radiation to warming
2. Improve our understanding of cloud-circulation-radiation interactions

***Relevance to NASA:** Constraining the response of clouds and precipitation to warming using satellite observations is imperative to reducing uncertainty in the response of climate to greenhouse-gas warming.

Data and Methods

Atmosphere-only GCM (NCAR CAM5.3), deep tropics only (20°S-20°N)

Category	Symbol	Description	Values (units)
convection "CONV"	1-3	Downdraft fraction	0.25, 0.5, 0.75
	4-8	Fractional rate of entrainment	0.08, 0.16, 0.25, 0.5, 1.5 (km^{-1})
	9-11	Convective timescale	30, 120, 180 (min)
	12-15	Evaporation efficiency	0.1, 0.5, 5, 10
			$(10^{-6}$ kg m^{-2} $s^{-1})^{-1/2}$ s^{-1}
macrophysics	a, b	Threshold RH for high clouds	0.65, 0.85
	c, d	Threshold RH for low clouds	0.8, 0.99
microphysics	e, f	Fall speed for stratiform ice	350, 1400 (s^{-1})
	g, h	Fall speed for stratiform snow	5.86, 23.44 ($m^{0.59}$ s^{-1})
"CLOUD"	i, j	Autoconversion size ice - snow	1e-4, 5e-4 (m)
	k, l	Collection efficiency, ice	0.001, 1
	m, n	Inverse variance of cloud water	0.5, 5
	o, p	Max w for ice nucleation	0.1, 1 (m s^{-1})
	q, r	Min w for liquid nucleation	0, 1 (m s^{-1})
	s, t	Radius of detrained ice	10, 50 (μm)

Results

Figure 1

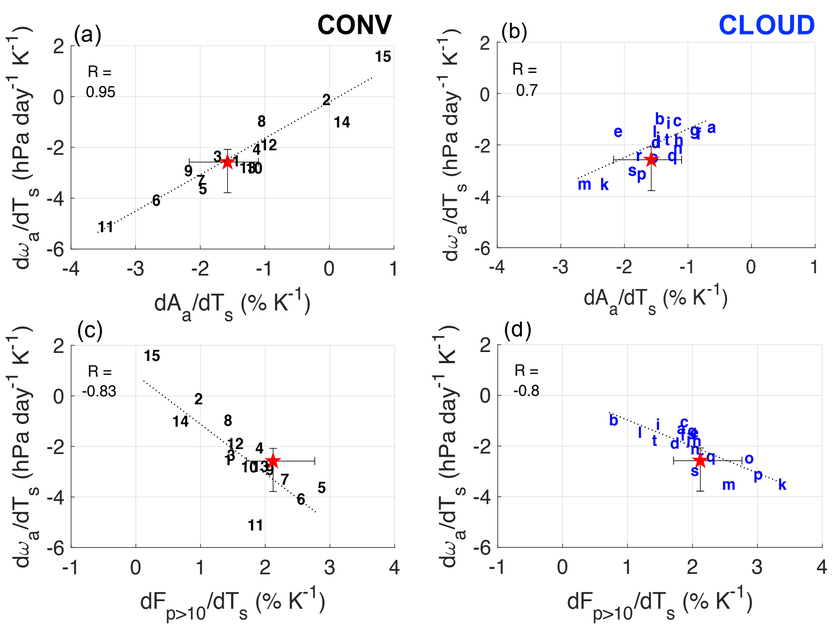

1. Circulation changes more sensitive to perturbing convective parameters than perturbing cloud parameters (ranges and slopes, Fig. 1a-b).
2. More strong precipitation per degree warming ($\frac{dF_{p>10}}{dT_s}$) corresponds to stronger ascent ($\frac{d\omega_a}{dT_s}$; Figs. 1 c-d) and a narrower ascent area ($\frac{dA_a}{dT_s}$; Figs. 1a-b) in the tropics.

Results

3. A narrower ascent area ($\frac{dA_a}{dT_s}$) corresponds to a greater reduction of high cloud fraction per degree warming ($\frac{dHCF}{dT_s}$) in **CONV**, but not in **CLOUD** (Fig. 2) – **WHY?** (Cloud radiative effects – see Fig. 3)

Figure 2

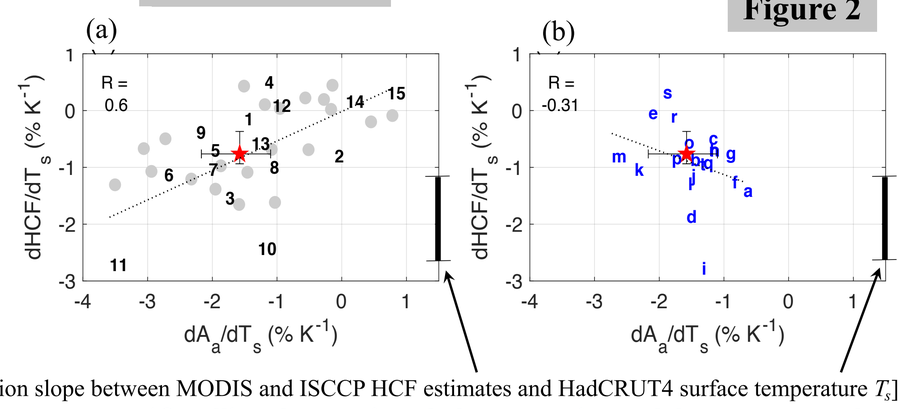

[95% confidence interval of the regression slope between MODIS and ISCCP HCF estimates and HadCRUT4 surface temperature T_s]

***Satellite observations help constrain model parameter values**

4. The **CONV** ensemble has remarkably similar spread, slope, and correlation compared to the CMIP5 models (Fig. 2a; gray dots).

Figure 3

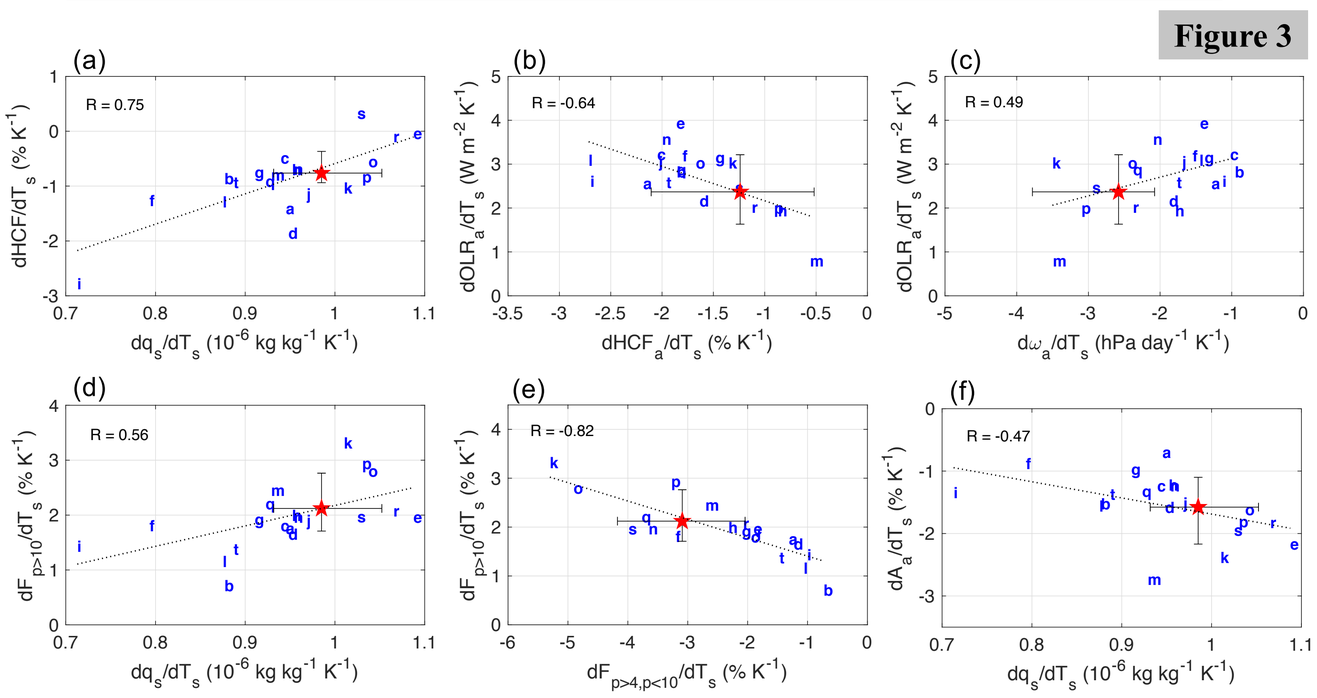

5. Less HCF reduction with warming = greater tropospheric stability (Fig. 3a).
6. Less HCF reduction over ascending region = less OLR (Fig. 3b) and greater energy flux into the atmospheric column, promoting an increase in ascent strength (Fig. 3c).
7. Strong convection (P > 10 mm day^{-1}) becomes more frequent (Fig. 3d) at the expense of weaker convection (P > 4, P < 10 mm day^{-1}; Fig. 3e) - increased convective threshold.

Summary of high cloud radiative effects on tropical ascent response to warming:

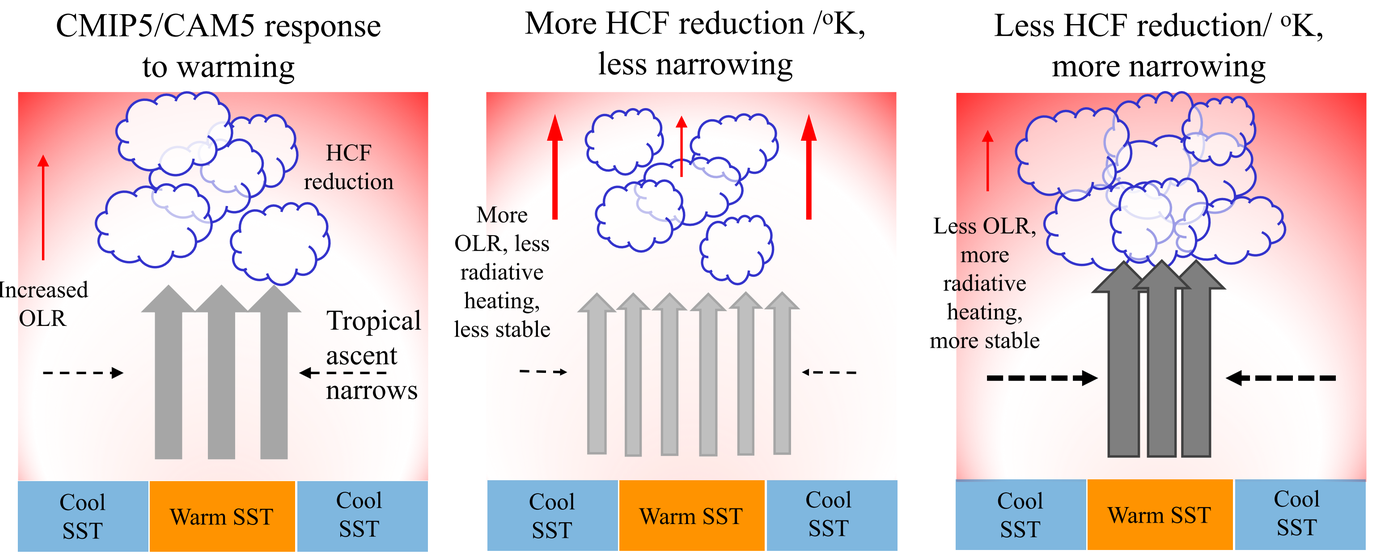

Conclusions

1. Reduction of tropical ascent area with interannual warming is more sensitive to convective processes than cloud physics in CESM (Fig. 1).
2. Different convective physics may explain the wide range of tropical high cloud and ascent area responses to warming among climate models (Fig. 2).
3. Decreases in high cloud fraction and cloud radiative heating may act to reduce tropical ascent narrowing with warming (Fig. 3).

Acknowledgments:
Funding for this project was provided by NASA NEWS, TASNPP, and ACMAP-AST.

Poster No. EB-06

National Aeronautics and Space Administration
Jet Propulsion Laboratory
California Institute of Technology
Pasadena, California
www.nasa.gov

National Aeronautics and Space Administration

Early Results of the CYGNSS Surface Heat Flux Product

Author: Juan A. Crespo (329E)
Derek J. Posselt (329E)

Introduction & Motivation

- **Latent (LHF) & sensible (SHF) heat fluxes aid in transport of heat and energy between the lower atmosphere and ocean surface.**
  - Primarily driven by winds/air-sea differences in temperature & humidity
- Increase baroclinicity & instability within boundary layer, influencing systems like:
  - Tropical Cyclones (TC)
  - Extratropical Cyclones (ETC)
  - Tropical Convection (e.g. MJO)
- **Spaceborne instruments don't consistently provide LHF/SHF estimates due to:**
  - **Signal attenuation from precipitation**
  - **Low spatial/temporal frequency**
- The **Cyclone Global Navigation Satellite System (CYGNSS)** provides improved surface wind speeds observations over tropical and subtropical oceans
  - Combined with MERRA-2 for temperature and humidity, can be used to estimate LHF/SHF
- While CYGNSS is a tropical mission, its orbit will allow it to observe a large number of the high surface heat fluxes observed over the oceans (**Fig. 1**)

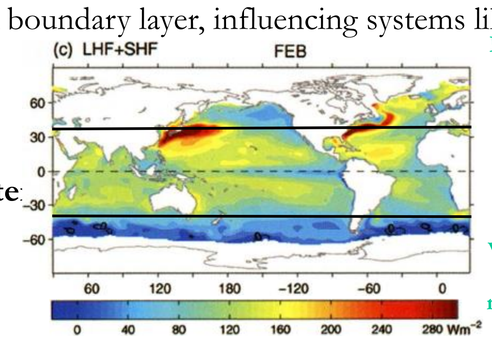

Fig. 1: Adapted from *Yu and Weller (2007, BAMS)*, combined LHF+SHF in February over world's oceans. Black lines represent range of CYGNSS observations.

The resulting surface heat flux estimates from CYGNSS have be used to develop a Level-2 (L2) Surface Heat Flux Product. It will be made publically available by Fall 2019; will provide LHF and SHF estimates throughout the entire CYGNSS mission.

Data & Methods

Cyclone Global Navigation Satellite System (CYGNSS)

- 8 observatories (**Fig. 2**), low-orbit inclination of 35°
- Observes GPS signals scattered off ocean surface
  - L1 Channel, 1575 MHz, 19-cm wavelength
- Two wind speed products used for LHF (**Eq. 1**) & SHF (**Eq. 2**) estimates:
  - **Fully Developed Seas (FDS):** Assumes sea state in equilibrium with wind speed
  - **Young Seas Limited Fetch (YSLF):** Assumes sea states not in equilibrium with the local wind; matched with Stepped Frequency Microwave Radiometer (SFMR) observations from the NOAA P-3 Hurricane Hunters.

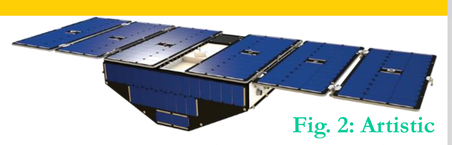

Fig. 2: Artistic visualization of a deployed CYGNSS observatory. *(Source: NASA)*

Modern-Era Retrospective Analysis for Research and Applications, Ver. 2 (MERRA-2)

- Combines in-situ & satellite observations with initial estimate of atmospheric state provided by global atmospheric models
- Source for air density, temperature/specific humidity (10m & surface)
- Temporal resolution: 1 hour | Spatial resolution: 0.5°x0.625°
- Co-located w/ CYGNSS specular points using nearest-neighbor method

Coupled Ocean-Atmosphere Response Experiment (COARE) Algorithm

- Based on Monin-Obukhov Stability Theory (MOST) to estimate LHF and SHF over the ocean surfaces using the bulk aerodynamic formulas (**Eqs. 1 & 2**)
- Uses winds from CYGNSS and thermodynamic variables from MERRA-2
- Parameterizes surface heat flux drag coefficients (C_D) as a function of gustiness, surface roughness, & atmospheric stability (**Eq. 3**).
- COARE 3.5 verified up to 25 m/s. Fluxes not used when winds surpass 25 m/s.

$$LHF = \rho_a L_v C_{DE} U(q_s - q_a) \quad \text{(Eq. 1)}$$

$$SHF = \rho_a c_p C_{DH} U(T_s - T_a) \quad \text{(Eq. 2)}$$

$$C_D(z/z_o, z/L, G) = \frac{-\overline{uw}}{U_r s_r} = \frac{-\overline{uw}}{U_r^2 G} = \left[\frac{\kappa}{ln(z/z_o) - \psi_m(z/L)}\right]^2 \quad \text{(Eq. 3)}$$

Preliminary Results: Hurricane Florence

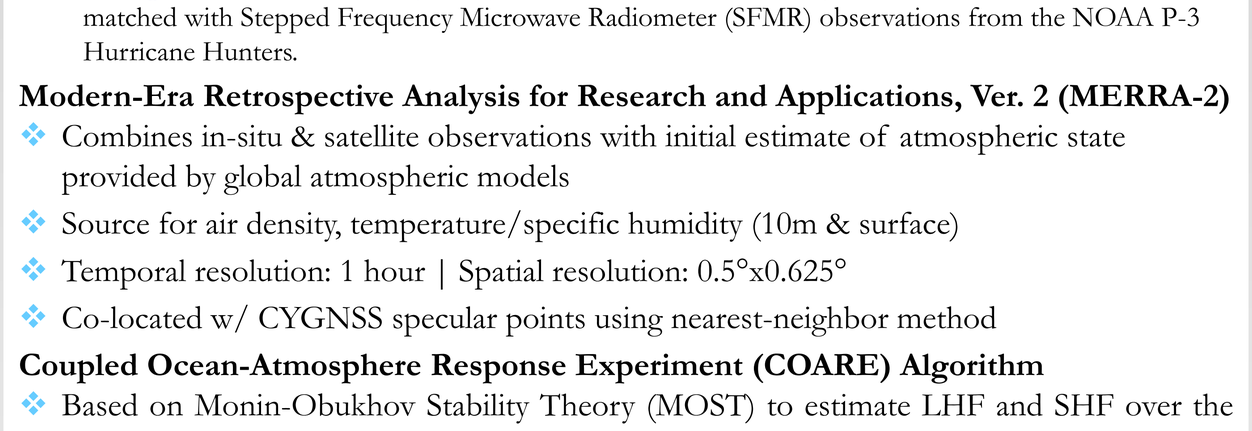

Fig. 3: Latent heat flux estimated with FDS winds (left) and with YSLF winds (right) for Hurricane Florence on 2018-09-14. MSLP (black contours) at 1800 UTC, with CYGNSS Observations ±3 hours from this time.

As Florence made landfall in Sept. 2018, its center remained along the coast traveling to the southwest, causing major coastal flooding. LHF surpassed over 300 W/m^2 as its center remained along the coast, possibly impacting the storm's development (**Fig. 3**). Given that CYGNSS's YSLF winds are higher than FDS winds and surpass the 25 m/s limit of the COARE algorithm, there's less observations associated with LHF w/ YSLF winds product.

Preliminary Results: Jan. 2018 *'Bomb Cyclone'*

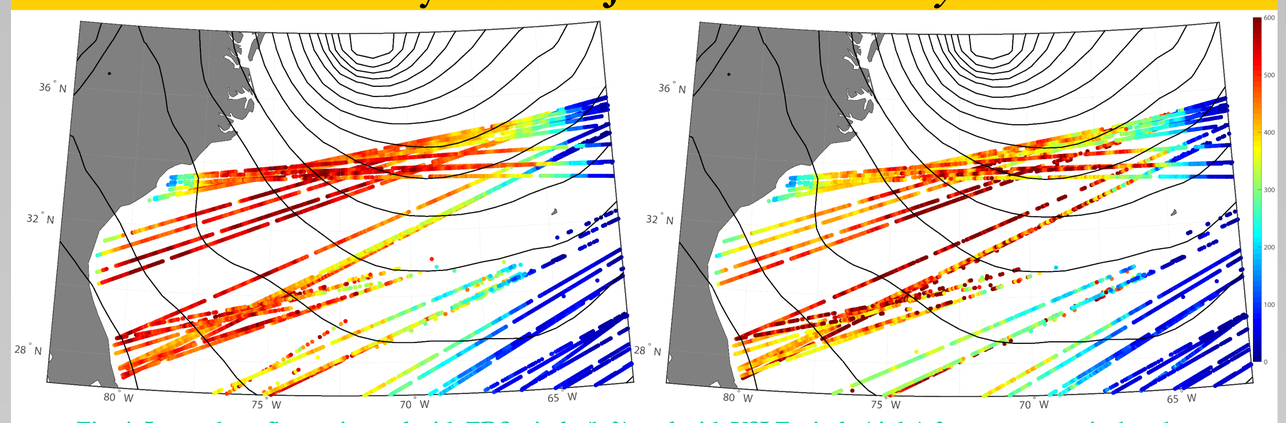

Fig. 4: Latent heat flux estimated with FDS winds (left) and with YSLF winds (right) for an extratropical cyclone on 2018-01-04. MSLP (black contours) at 1500 UTC, with CYGNSS Observations ±3 hours from this time.

In early January 2018, a rapidly developing extratropical cyclone (aka: '*bomb cyclone*') developed off the US East Coast, and produced a significant amount of snowfall. CYGNSS observed the equatorward side of the ETC, observing the large latent heat flux values (over 600 W/m^2) associated with this system (**Fig. 4**). While YSLF gives one higher fluxes than FDS, it can sometimes yield noisier results than the LHF/SHF product with FDS winds.

Comparisons with Buoy Data

- CYGNSS surface heat flux estimates compare well to LHF and SHF estimates from buoy data at lower flux values (LHF < 200 W/m^2, SHF < 100 W/m^2) (**Fig. 5**)
- Greater scatter and disagreement at higher fluxes between CYGNSS and the buoy data (**Fig. 5**)

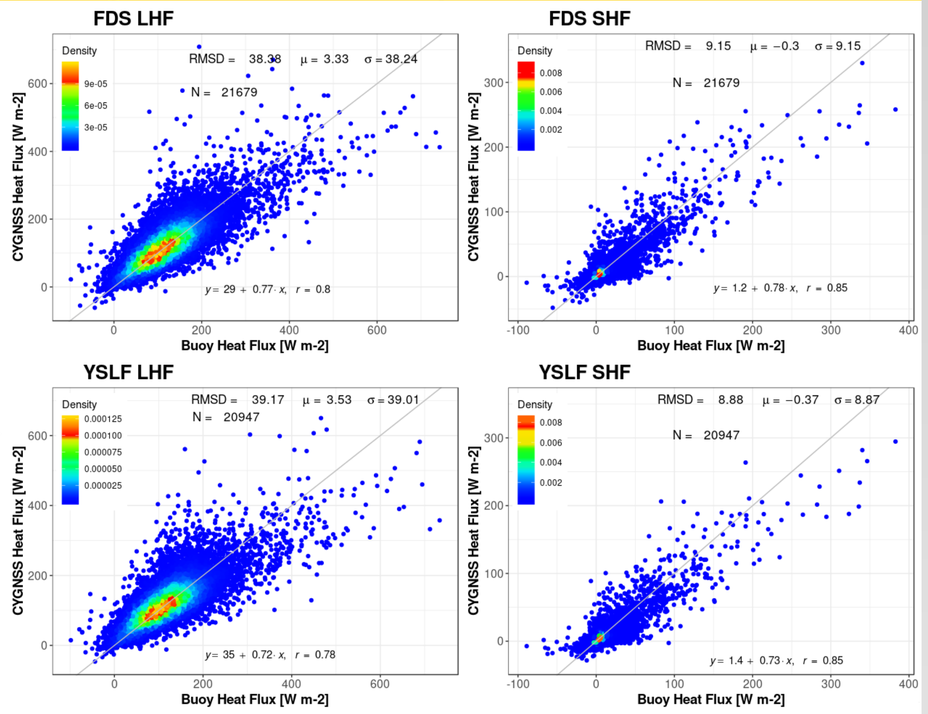

Fig. 5 (right): Buoy comparisons of CYGNSS LHF (left) & SHF (right) products that use FDS (top) & YSLF (bottom) surface winds.

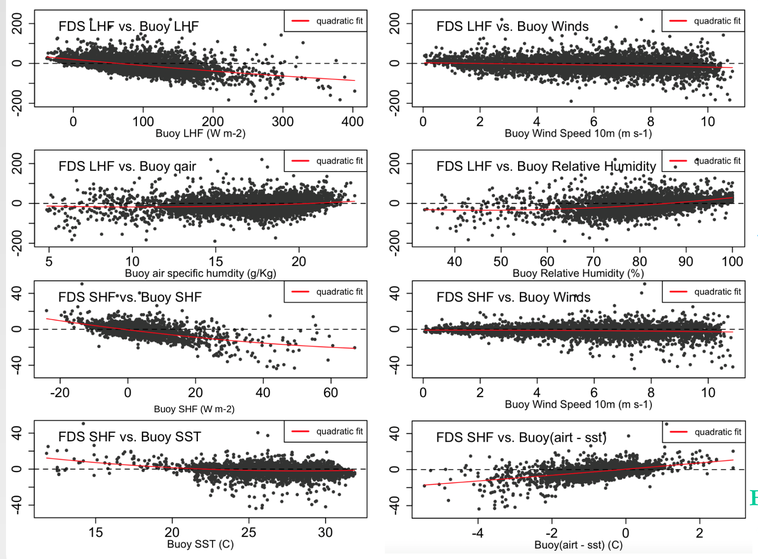

- Differences of LHF & SHF b/w CYGNSS & buoy estimate increase as buoy fluxes increase (**Fig. 6**)
  - CYGNSS underestimating higher wind speeds, but difference is minimal under 10 m/s (**Fig. 6**)
- Other factors (i.e. MERRA-2) could impact flux estimates
  - Difference b/w air temperature & SST (*airt-sst*) (**Fig. 6**)
  - Further analysis/more ground truth data at higher fluxes needed to address differences

Fig. 6 (left): How differences vary b/w LHF (top 4) & SHF (bottom 4) from CYGNSS & buoy data w/ different variables associated w/ flux estimations.

Conclusions

- **A Level-2 Surface Heat Flux Product has been developed for the entire CYGNSS mission by utilizing its L2 winds combined with MERRA-2 reanalysis data.**
  - Initial release through Physical Oceanography Distributed Active Archive Center (PO.DAAC) by Fall 2019
- **Surface Heat Flux Product offers good estimates of LHF and SHF at lower values.**
  - Greater scatter at higher valued fluxes due to errors in CYGNSS high wind speeds observations
  - Future improvements of CYGNSS L2 wind speed observations could improve higher heat flux estimates
- **Future development needed to estimate LHF/SHF at wind speeds >25 m/s**
  - Uncertainties regarding the drag coefficient (**Eq. 3**)
  - Impact of sea salt spray on LHF/SHF at high wind speeds
- **MERRA-2 suffices for initial version of the CYGNSS Surface Heat Flux product**
  - Limited as a reanalysis dataset and data latency (2-3 weeks after a month has ended).
  - Future versions may utilize different sources for temperature/humidity, though that is still being discussed.

Acknowledgements

We would like to thank **Dr. Jim Edson** at Woods Hole for his initial assistance with the COARE 3.5 algorithm. We would also like to thank **Dr. J. Brent Roberts** at NASA Marshall of the buoy data, and **Dr. Shakeel Asharaf** at JPL for producing **Figs. 5 & 6.**

This work was supported by NASA CYGNSS Science Team Grant **NNH17ZDA001N**, and by the CYGNSS mission under NASA Science Mission Directorate Contract **NNL13AQ00C**.

National Aeronautics and Space Administration
Jet Propulsion Laboratory
California Institute of Technology
Pasadena, California
www.nasa.gov

This work was carried out at the Jet Propulsion Laboratory, California Institute of Technology under a contract with the National Aeronautics and Space Administration

Poster No. EB-07

National Aeronautics and Space Administration

Testing the microphysics-dynamics coupling in the EDMF parameterization of clouds and turbulence.

Anna Jaruga (329E), Joao Teixeira (3292), Tapio Schneider (Caltech)

1. Motivation:

Clouds and rain are major sources of uncertainty in numerical models of climate.

2. General goals:

Build parameterization for boundary layer/cloud dynamics:
- For turbulence, shallow/deep convection (unified)
- Scale aware and with memory (prognostic)
- Validated with Large Eddy Simulation (LES) and observational data

3. Current work:

Couple microphysics parametrizations (build for LES) with the dynamics in the eddy-diffusivity mass-flux (EDMF) Single Column Model (SCM).

4. Future work:

- Test different microphysics parameterizations
- Prognostic rain formation, evaporation and fall speed,
- Partition rain between updrafts, environment, downdrafts(?)

5. EDMF dynamics:

The EDMF scheme represents sub-grid scale dynamics by decomposing it into:
- Vertical coherent updrafts represented by a single bulk plume or by multiple plumes (mass-flux scheme).
- Isotropic turbulent environment represented by joint-normal distribution of model variables with prognosed (co-)variance (eddy-diffusivity scheme).

$$\frac{\partial(\rho a_0 \overline{\phi'_0\psi'_0})}{\partial t} + \frac{\partial(\rho a_0 \overline{w}_0 \overline{\phi'_0\psi'_0})}{\partial z} + \nabla_h \cdot \left(\rho a_0 \langle \mathbf{u}_h \rangle \overline{\phi'_0\psi'_0}\right) =$$
$$2\rho a_0 K \frac{\partial \overline{\psi}_0}{\partial z}\frac{\partial \overline{\phi}_0}{\partial z} + \rho a_0 \overline{w}_0 \left(\sum_j \epsilon_{0j}(\overline{\phi}_j - \overline{\phi}_0)(\overline{\psi}_j - \overline{\psi}_0) - \delta_0 \overline{\phi'_0\psi'_0}\right)$$
$$+ \frac{\partial}{\partial z}\left(\rho a_0 K \frac{\partial}{\partial z}\overline{\phi'_0\psi'_0}\right) + \rho a_0 (\overline{S'_{\phi,0}\psi'_0} + \overline{S'_{\psi,0}\phi'_0}).$$

Cloud microphysics source terms are coupled with EDMF by:
- summing the source terms from plumes
- numerically integrating the source terms over the distribution in the environment

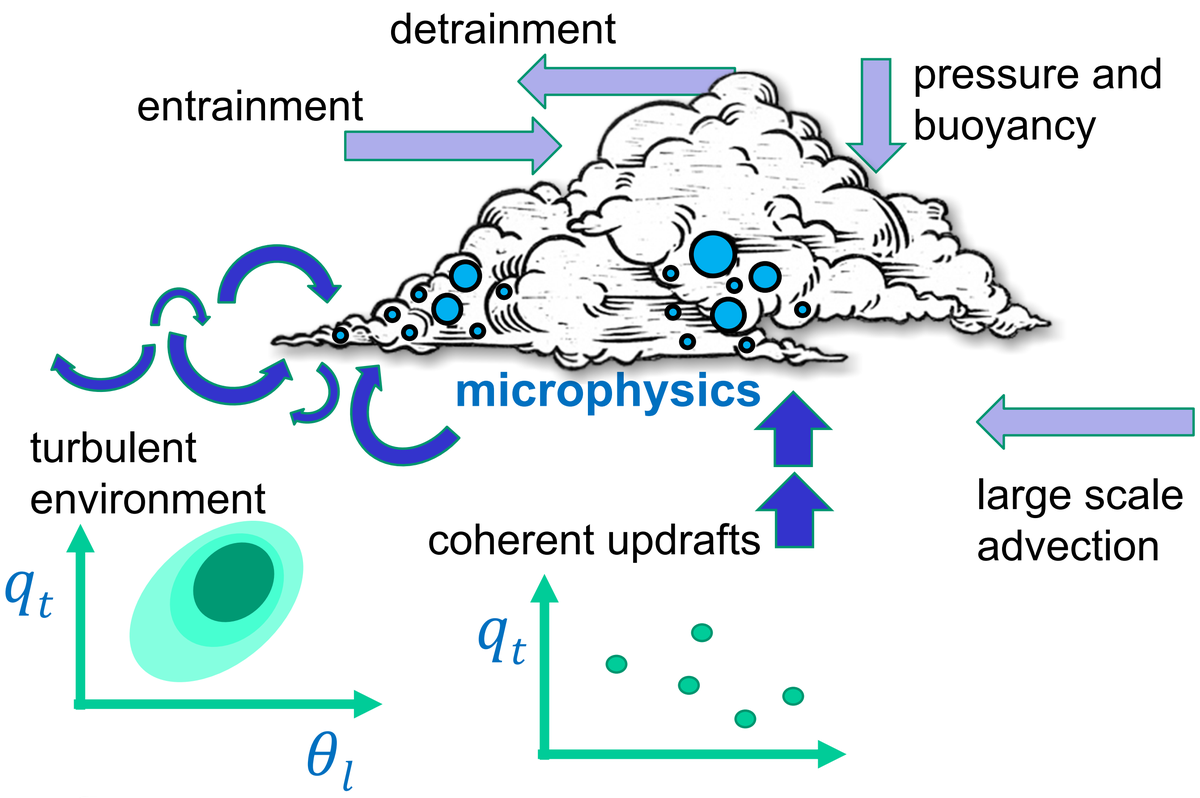

Benefits:
- Consistent coupling between dynamics and microphysics closures
- Ease of changing between different microphysics parameterization schemes

6. Results:

Prognostic (co-)variances of thermodynamic properties in the environment
- Bomex (shallow convection, no precipitation)
- Good agreement between the LES and SCM EDMF results
- The biggest discrepancies occur near the cloud tops where SCM EDMF covariances decrease too rapidly.

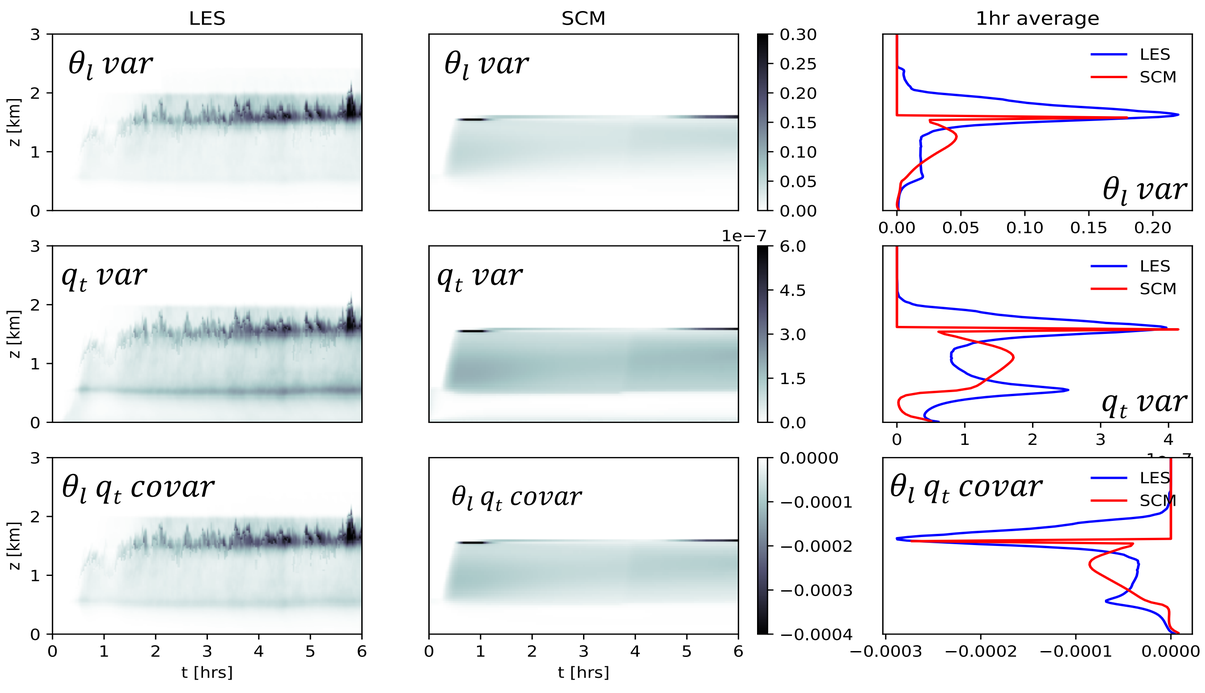

Figure 1: (Co-)variances of θ_l and q_t from LES (left column), SCM EDMF (middle column), 1 hour averages (right column).

Microphysics in EDMF
- Microphysics in the SCM EDMF uses (co)variances
- SCM EDMF q_l compares well with LES results in mean profile and in the updraft subdomain mean
- The biggest difference is in the environmental q_l, which peaks at lower levels in the SCM EDMF than in LES

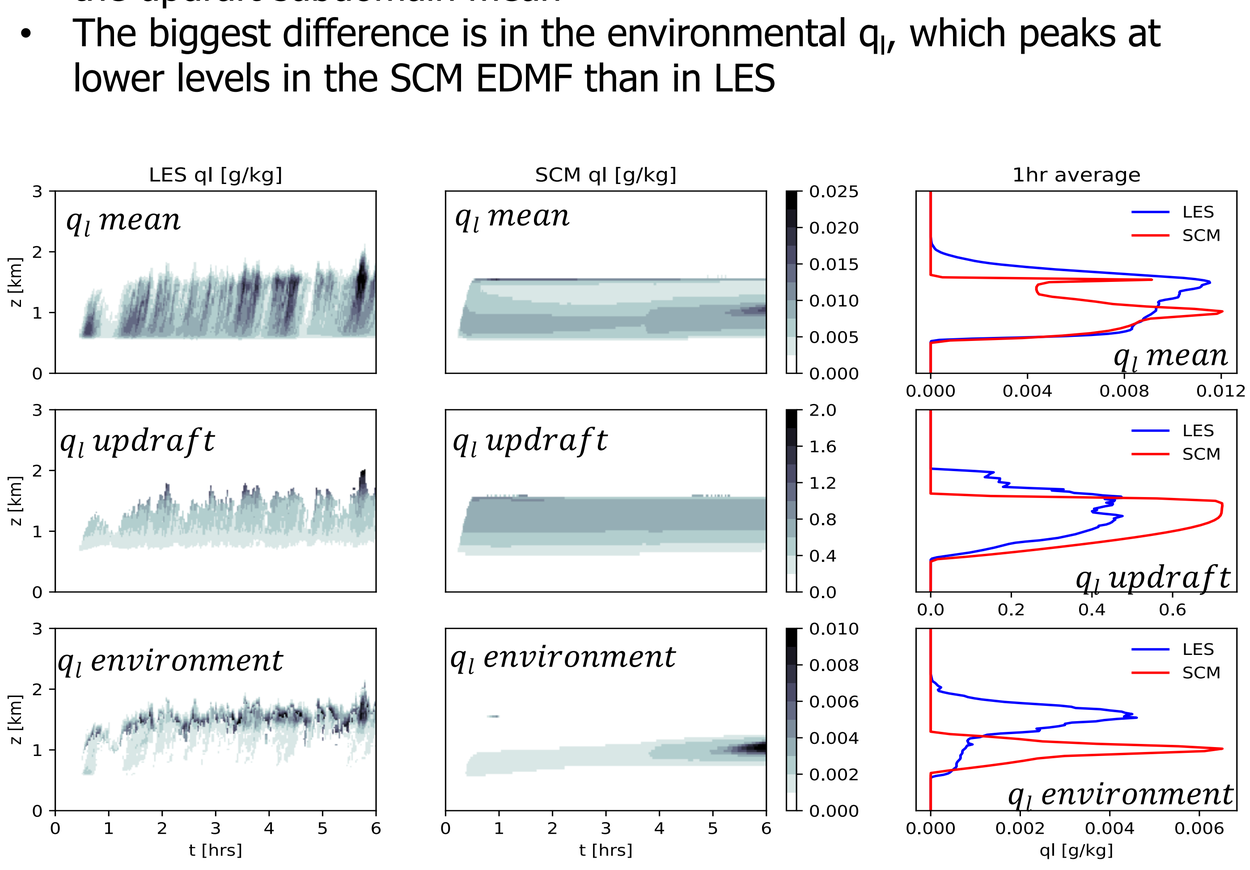

Figure 2: Liquid water specific humidity (q_l) from LES (left column) SCM EDMF (middle column) and 1 hour averages (right column). Top row shows domain mean. Middle row shows updraft and bottom row environment subdomain means.

National Aeronautics and Space Administration
Jet Propulsion Laboratory
California Institute of Technology
Pasadena, California

www.nasa.gov

Poster No. EB-08

National Aeronautics and Space Administration

Predictability of atmospheric moist convection revealed by all-sky infrared satellite radiance assimilation

Author: Masashi Minamide (329E)
Derek J. Posselt (329E)

1. Goal

- To understand **what are the key processes** of the development of atmospheric moist convection at the observed timing and location
- To reveal which of these processes **can/cannot be captured and predicted with program-of-record** observations
- To explore **what future mission/instrument will be effective** to further improve numerical weather predictions

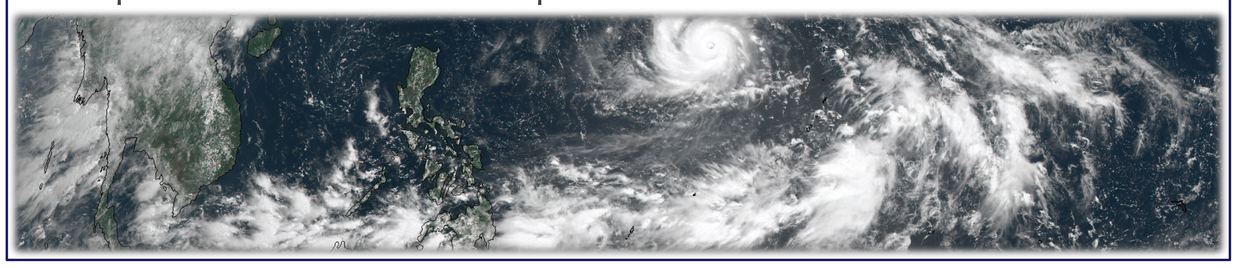

2. Introduction

- Atmospheric deep moist convection
  - **Multi-scale interactions**: plays critical role in developing severe weather events, such as thunderstorms and tropical cyclones.
  - **Limited predictability**: chaotic process of development prevents not only the prediction, but also the scientific understanding.
- 2017 Decadal Survey, Objective W-4
  - "Why do convective storms, heavy precipitation, and clouds occur **exactly when** and **where** they do"

3. Method

Program-of-record

- Geostationary Operational Environmental Satellite **(GOES)-16**

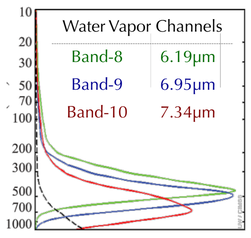

Band	One of Water Vapor bands: Mid-upper troposphere (6.19 μm)
Temporal frequency	15 mins (Full Disk scan)
Spatial resolution	~2 km (Full Disk scan)

Case

- **Meso-scale Convective System**
- CPEX field campaign (06/11/2017)

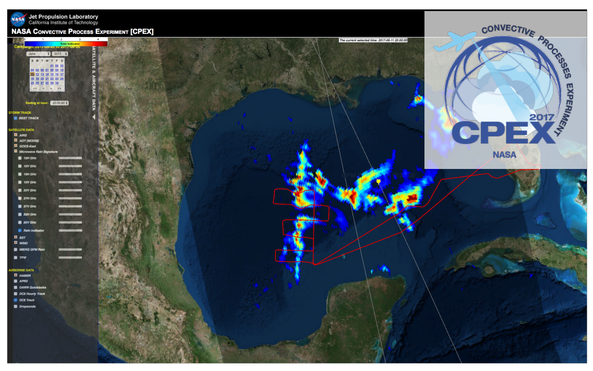

Advanced PSU Ensemble-Kalman Filter Data Assimilation System

- Developed at Pennsylvania State University (PSU) to **enable direct assimilation of all-sky infrared satellite radiances** with Weather Research and Forecast model (WRF) and Community Radiative Transfer Model (CRTM).
- State-of-the-art data assimilation system will be employed to asses
  - Mechanisms of the development of moist convection during CPEX
  - Contribution of GOES-16 to the improvement of the prediction

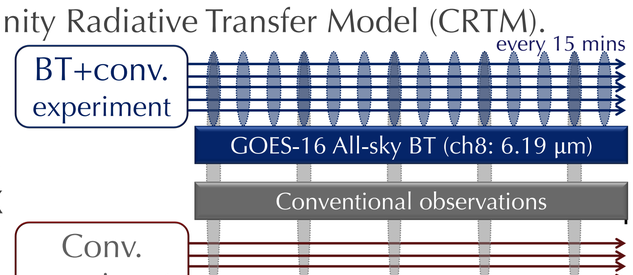

4. Result

Data assimilation performance

- Assimilation of GOES-16 all-sky infrared satellite radiances contributed to better capturing the atmospheric moist convective events during CPEX.

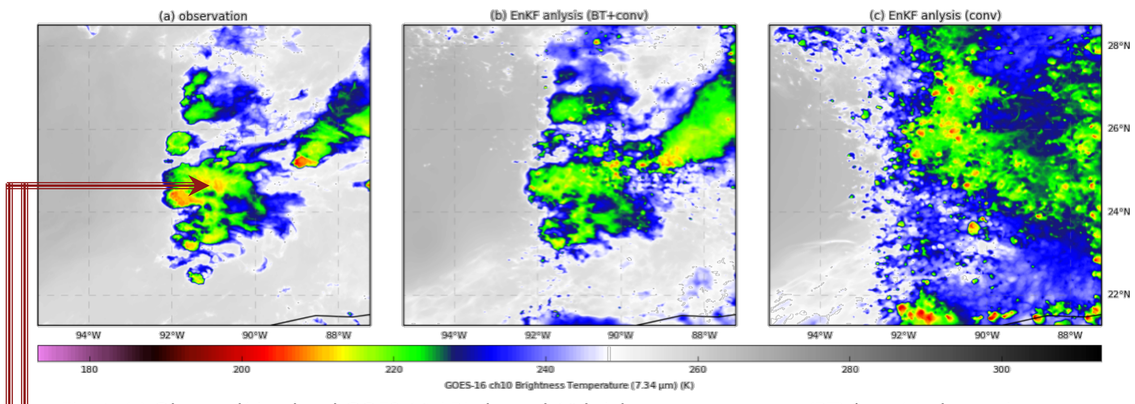

Fig. 1. (a) Observed/simulated GOES-16 ABI channel 10 brightness temperatures (BT) from (a) observation, (b) "BT+conventional" and (c) "conventional" experiment, at 1800 UTC June 2017 over Gulf of Mexico.

What improved the prediction of the convective system?

- Meso-α scale (2000-200km) background: moist mid-troposphere
- Meso-β scale (200-20km) features: convective system structure

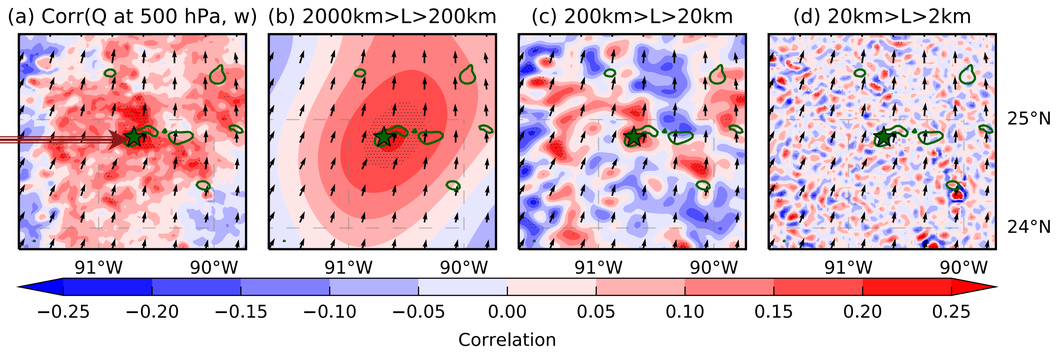

Fig. 2. (a) Ensemble correlation of the strength of updraft (i.e. mid-upper tropospheric average of vertical wind) **at star** with mid-tropospheric moisture amount of (a) all horizontal scales, (b) meso-α (2000-200km), (c) Meso-β scale (200-20km) and (d) meso-γ (20-2km) scale, at 1800 UTC June 2017. Vector: ensemble-mean horizontal wind at 500 hPa.

What will be necessary to capture an individual convection at the exact location and timing?

- Relatively drier (but moist enough) meso-α scale surrounding +
- Meso-β to **-γ (20-2km) scale** strongly concentrated moistening

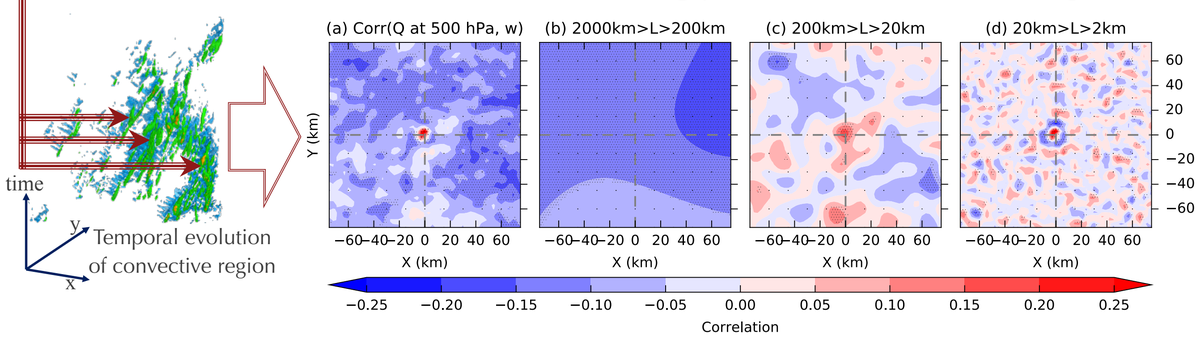

Fig. 3. As in Fig. 2 but for the strength of updraft **at the center of each convection**.

5. Conclusion

- New-generation geostationary satellites GOES-16 from program-of-record has contributed to the better prediction of convective events, but not perfect.
- Meso-α (2000-200km) to meso-β (200-20km) information helps to generally predict the location of convective system.
- Meso-β (200-20km) to **meso-γ (20-2km) scale** information will be indispensable to capture moist convection at the exact timing and location.
- Importance of temporal frequency will be further explored in future study.

National Aeronautics and Space Administration
Jet Propulsion Laboratory
California Institute of Technology
Pasadena, California

www.nasa.gov

Poster No. EB-09

National Aeronautics and Space Administration

Observationally-Constrained Ensembles & Uncertainty Quantification for Future Projections of Global Atmospheric Rivers

Elias Massoud (329F)
Bin Guan (329J) , Vicky Espinoza (UC-Merced / Past JPL Intern) , Duane Waliser (8000)

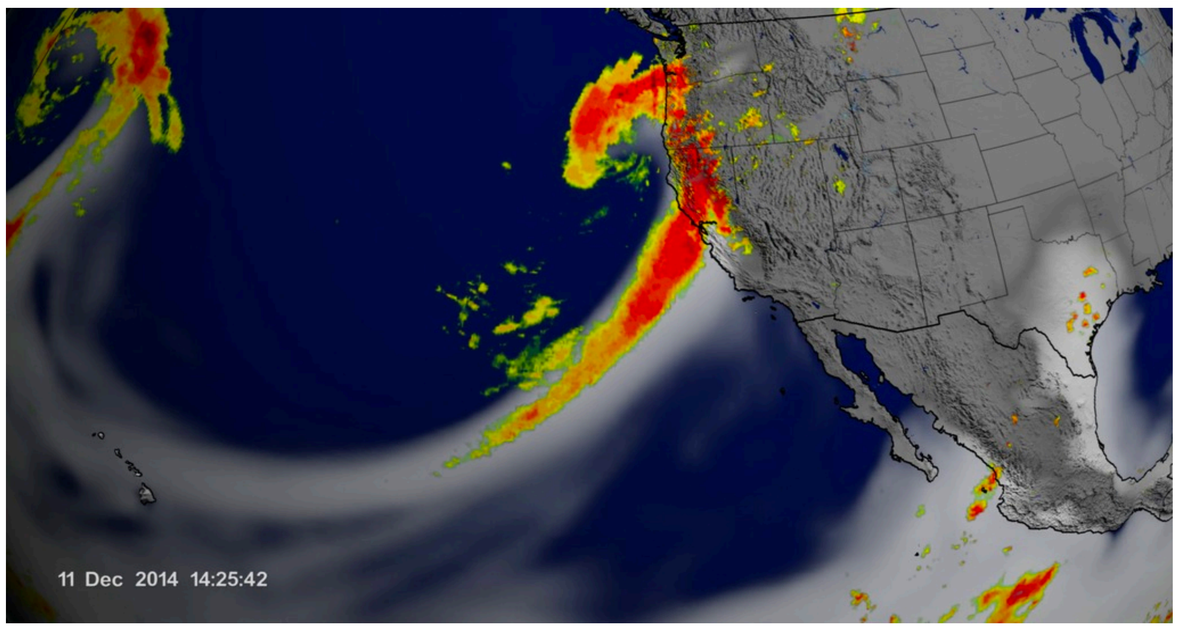

INTRODUCTION

Atmospheric rivers (ARs) are narrow jets of integrated water vapor transport that are important for the global water cycle, and also have large impacts on local weather and regional hydrology. Future climate projections from CMIP5 models indicate atmospheric river frequency will increase by ~50% globally by the end of the century. Model ensemble weighting strategies based on atmospheric river performance skill and model independence are considered and compared. Strategies based on skill and independence that differ from equal weighting result in lower uncertainties in the future estimates.

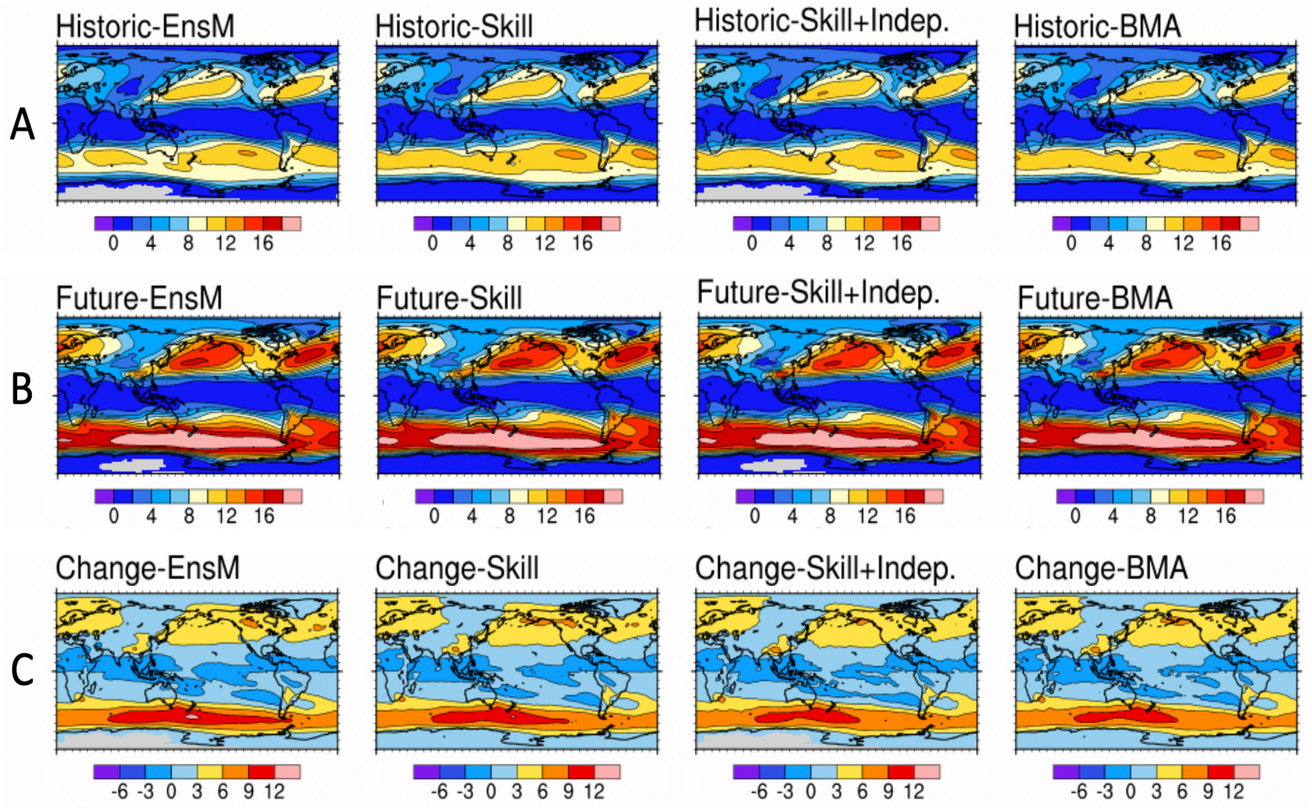

INTERPRETATION of RESULTS – FUTURE GLOBAL AR FREQUENCY

A) Global AR frequency map for the historical period (1979–2002) for the various weighted model averages chosen in this study: ensemble mean, skill weighting, skill and independence weighting, and the BMA model.
B) Future global AR frequency map for the RCP8.5 warming scenario (2073–2096) for the weighted model averages in this study: ensemble mean, skill weighting, skill and independence weighting, and the BMA model.
C) The difference between future and historic estimates of AR frequency, for the various weighted model averages in this study: ensemble mean, skill weighting, skill and independence weighting, and the BMA model.

All the figures in this plot are in units of frequency, or [% of timesteps].

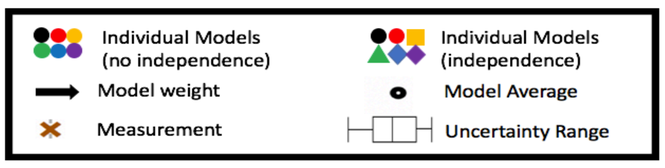

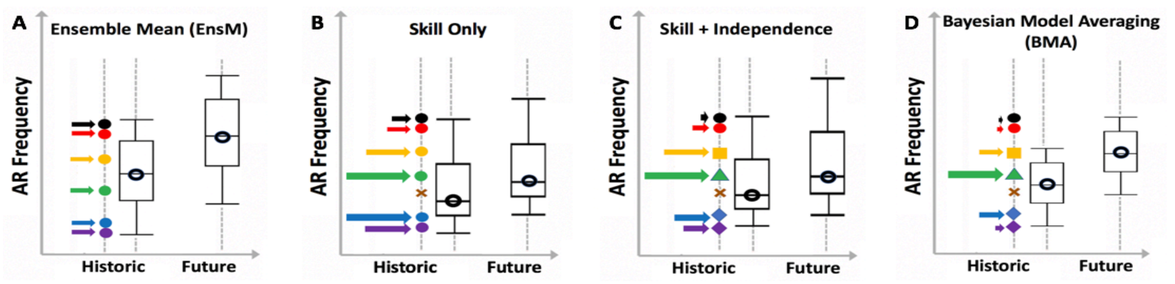

METHODS

Schematic illustration of model averaging using a six-member ensemble and single prediction of interest (AR frequency). The forecast of each model is displayed with the solid shapes, and the model average and its uncertainty are depicted with the open circle and the box-and-whisker plot, respectively.
A) The ensemble mean (EnsM) strategy showing each arrow is the same size for all models, indicating the same weight is applied for each model.
D) The Bayesian Model Averaging (BMA) method shows the weighted model average and its uncertainty range envelope the observation as closely as statistically possible. As a result, there is a higher weight on skillful and independent models.

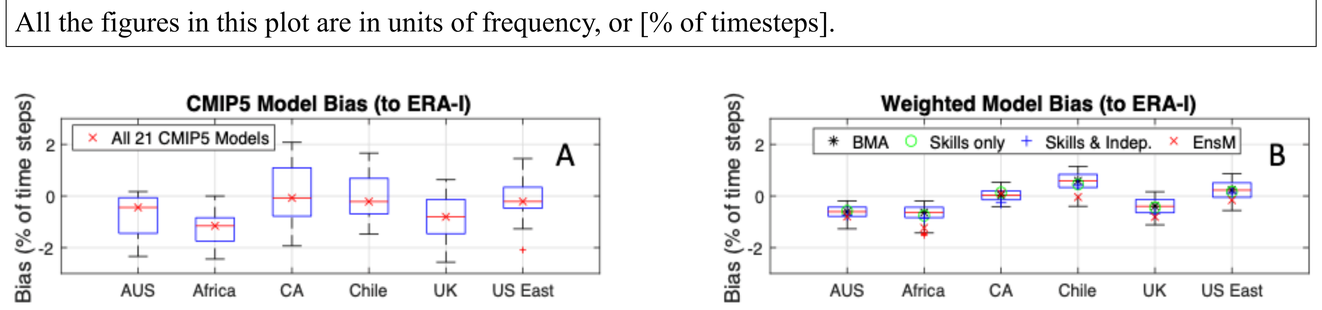

INTERPRETATION of RESULTS – REGIONAL BIAS AND FUTURE CHANGE

A) Model bias for select land falling regions compared to observations (ERA-Interim) for all 21 CMIP5 models.
B) Model bias for the same regions compared to observations (ERA-Interim) for the weighted model averages.
C) Future change in AR frequency for all 21 CMIP5 models. Relative percent changes are shown numerically with the uncertainty spread of the estimates.
D) Future change in AR frequency for the weighted model averages. Relative percent changes are shown numerically with the uncertainty spread of the estimates.

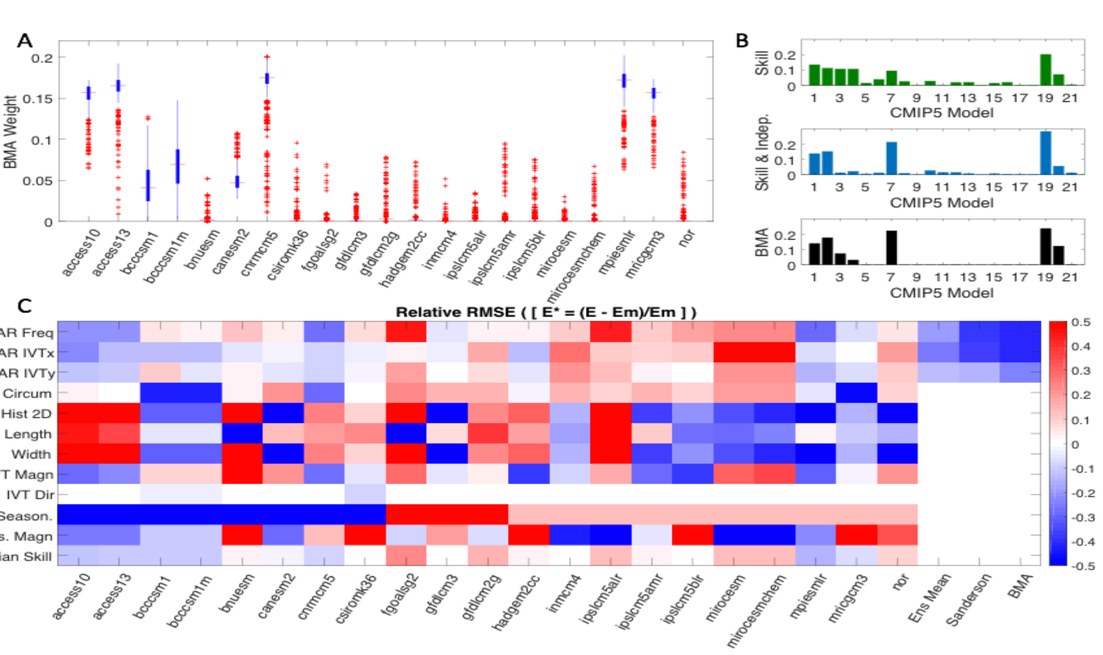

RESULTS – MODEL WEIGHTS

A) Distribution of the model weights calculated using the BMA method.
B) Estimated weights for each model using the various weighting strategies, (top) Skill, (middle) Skill & Independence, (bottom) BMA methods.
C) A graphical representation of the model skill matrix for a number of variables. Each column represents a single climate model, and rows represent the different AR metrics. The colors along each row represent the magnitude of model errors compared to observations (ERA-Interim). Blue generally means a skillful model, and red means a model with less skill.

CONCLUSIONS

Comparisons between the AR frequency simulated by the various weighting strategies builds confidence that relative AR frequency will increase by ~50% globally in the future. These results are constrained using observations (ERA-Interim), with the exception of the ensemble mean method. The ensemble mean overestimates the amount of increase throughout significant portions of the globe by about 1% in AR frequency, or 3-4 days of AR activity per year. However, the ensemble mean is consistent with other model ensemble approaches in areas of landfalling ARs, which show an increase in AR frequency for most regions, with high certainty. Furthermore, the weighting strategies introduced in this study produce future change estimates with lower uncertainties than the ensemble mean approach, especially for the BMA method.

References

- Espinoza, Vicky, Duane E. Waliser, Bin Guan, David A. Lavers, and F. Martin Ralph. "*Global analysis of climate change projection effects on atmospheric rivers.*" Geophysical Research Letters 45, no. 9 (2018): 4299-4308.
- Massoud, Elias C., Vicky Espinoza, Bin Guan, Duane E. Waliser. "*Global Climate Model Ensemble Approaches for Future Projections of Atmospheric Rivers.*" Journal of Earth's Future XX, no. X (2019): xxxx-xxxx. Submitted.

National Aeronautics and Space Administration /Jet Propulsion Laboratory
California Institute of Technology, Pasadena, California

Poster No. EB-10

National Aeronautics and Space Administration

Detecting methane point sources from space using hyperspectral surface imagers

Daniel Cusworth (329G), Andrew K. Thorpe (382B), Riley M. Duren (8000), David R. Thompson (382B), Christian Frankenberg (329I), Charles E. Miller (329G)

Project motivation

- Many new satellite imaging spectrometers will launch soon with sensitivity in the shortwave infrared (SWIR).
- Methane is powerful greenhouse gas with absorption features in the SWIR.
- **Will these satellites be able to detect large methane point sources?**

Table 1. SWIR remote sensors for observing methane

Instrument	Pixel size (km²)	SWIR spectral range (nm)	Spectral resolution (nm)	Signal-to-noise (SNR)	Observing epoch
Aircraft					
AVIRIS-NG	0.003 × 0.003	1600-1700; 2200–2510	5.0	200-400	Campaigns
Satellite					
Atmospheric sensors					
SCIAMACHY	30 × 60	1630–1670	1.4	1500	2002-2012
GOSAT	10 × 10	1630–1700	0.06	300	2009-
TROPOMI	7 × 7	2305–2385	0.25	100	2017-
AMPS	0.03 × 0.03	1990–2420	1.0	200-400	Proposed
Imaging spectrometers					
PRISMA	0.03 × 0.03	2200–2500	10	180	2019-
EnMAP	0.03 × 0.03	2200–2450	10	180	2020-
EMIT	0.06 × 0.06	2200–2510	7-10	200-300	2022-
SBG	0.03 × 0.03	2200–2510	7-10	200-300	2025-

Simulated satellite spectra

We use the EnMAP End-to-End Simulation tool (EeteS) to generate satellite radiance spectra.

We add methane plumes to images using the Weather & Research Forecasting Large Eddy Simulation model (WRF-LES)

Example EeteS + WRF-LES scenes over different surfaces

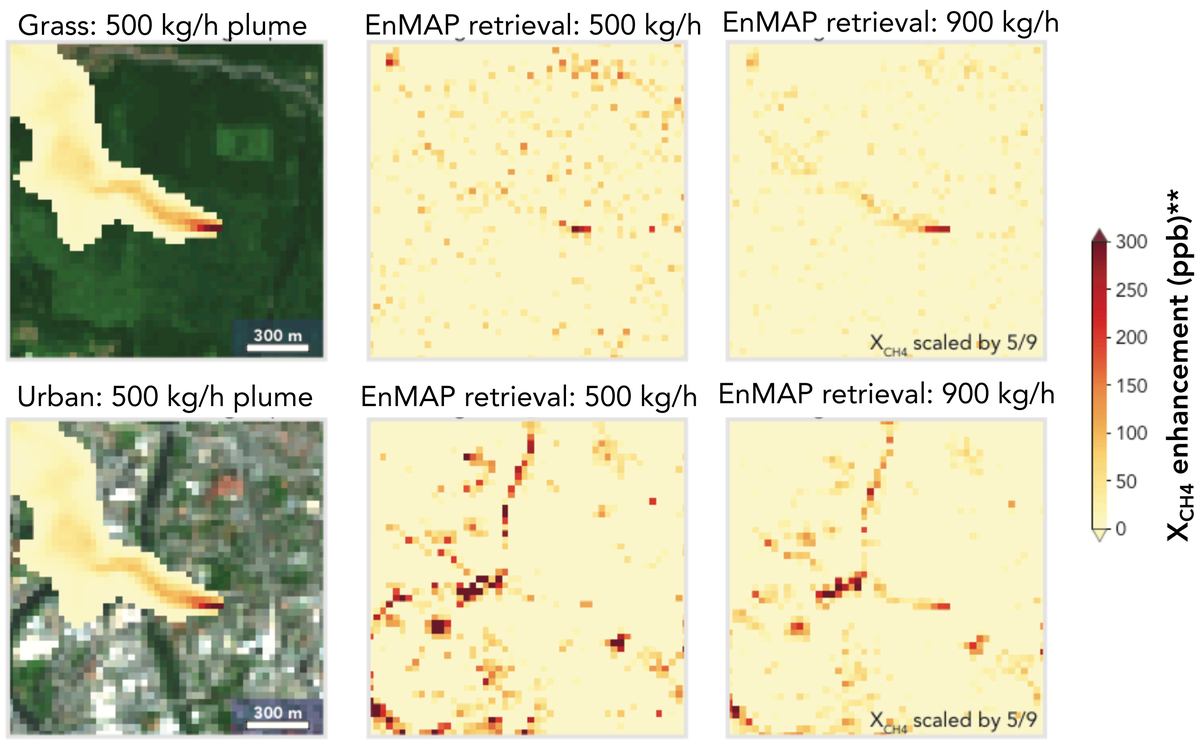

The methane plume structure is better retrieved over homogenous surfaces with larger emission rates.

Methane retrieval for imaging spectrometers

We employ the **IMAP-DOAS*** algorithm to infer methane columns from satellite radiance spectra:

Modeled radiance — Gas scaling factor — Surface scattering

$$F^h(\mathbf{x},\lambda) = I_0(\lambda)\exp\left(-A\sum_{n=1}^{3} s_n \sum_{l=1}^{72} \tau_{n,l}\right)\sum_{k=0}^{K} a_k P_k(\lambda)$$

Solar spectrum — Airmass factor — Gas optical depth

An iterative Bayesian inversion retrieves atmospheric state ($\hat{\mathbf{x}}$) and optimized error characteristics ($\hat{\mathbf{S}}$).

We assess error two ways: 1) Relative Root-mean squared error (RRMSE) of EeteS retrievals vs. truth. 2) Posterior error covariance $\hat{\mathbf{S}}$:

Precision of methane retrievals for imaging spectrometers

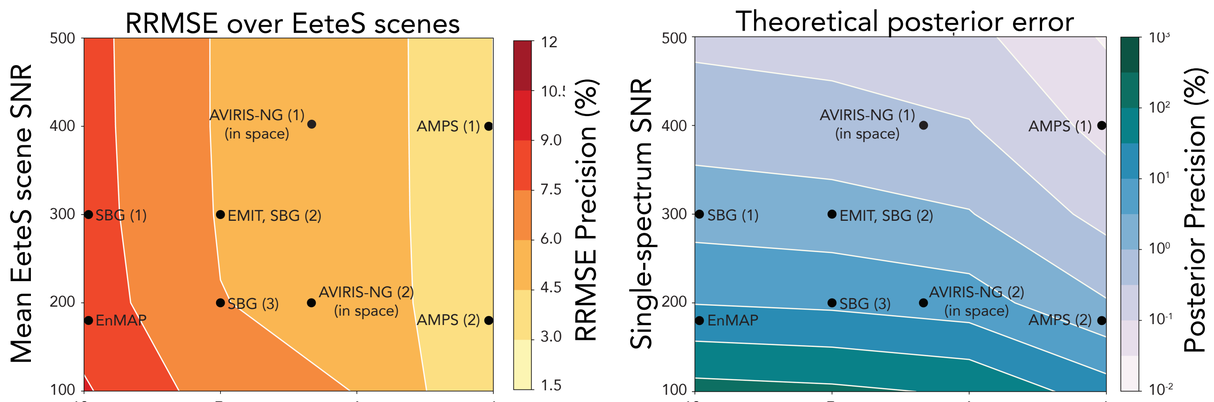

Depending on how error is quantified, either increasing SNR or spectral resolution is more effective at constraining methane emissions.

Validation on AVIRIS-NG images

We downsample airborne AVIRIS-NG images that were flown over California oil/gas facilities to match EnMAP's spectral and spatial resolution.

We infer an emission rate (Q) by masking the plume structure, integrating the methane enhancement, and analyzing the wind speed***.

Methane retrievals over oil/gas facilities in California

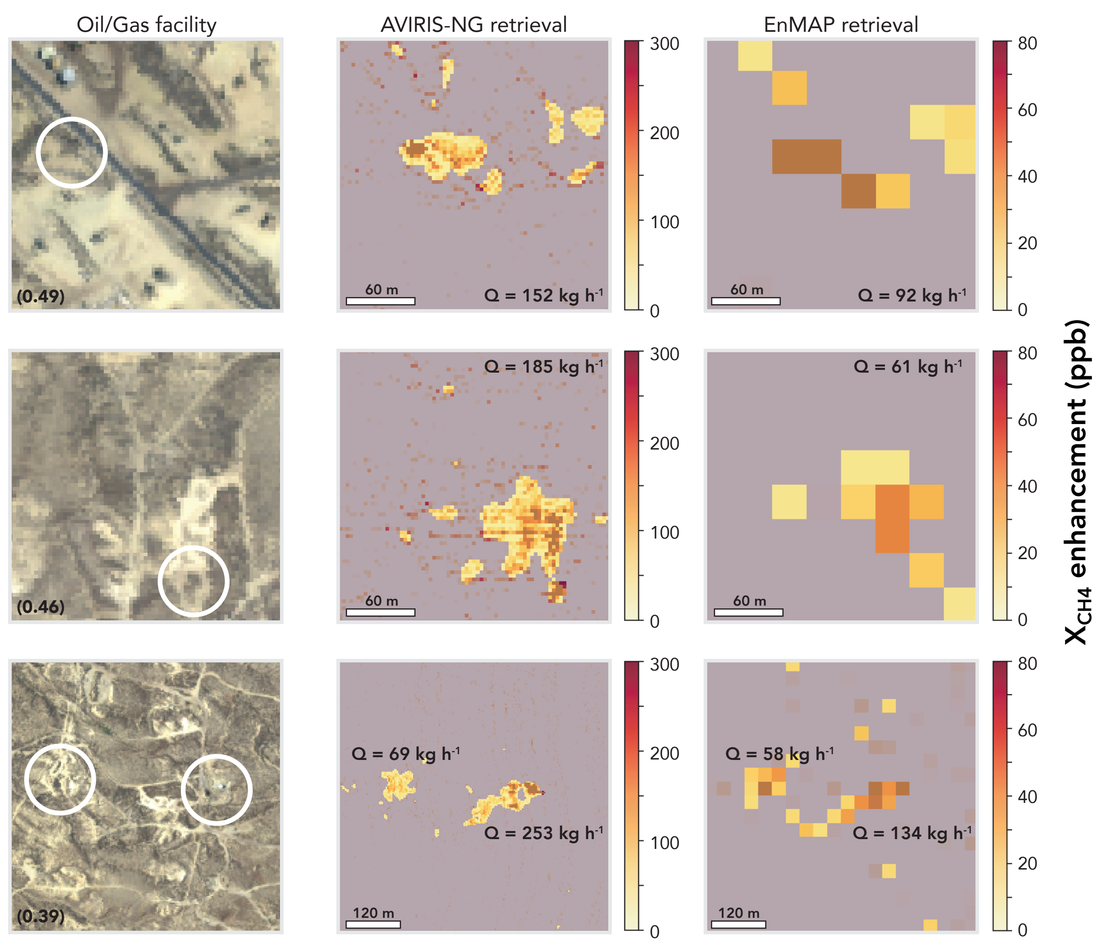

AVIRIS-NG derived emission rates agree with EnMAP within a factor of 1-3.

Poster No. EB-11

National Aeronautics and Space Administration
Jet Propulsion Laboratory
California Institute of Technology
Pasadena, California

www.nasa.gov

*IMAP-DOAS: Iterative Maximum A Posteriori - Differential Optical Absorption Spectroscopy
**Methane retrievals in units of dry air column methane mixing ratio
*** Plume mask derived by applying median and gaussian filter to pixels greater than the 85th percentile of XCH4. Emission rate derived using method of Varon et al. (2018): *Quantifying methane point sources from fine-scale satellite observations of atmospheric methane plumes.*

National Aeronautics and Space Administration

CYGNSS Surface Wind Validation over the Tropical Ocean using Moored Buoy Observations

Author: Shakeel Asharaf (329J-Affiliate)
Duane E. Waliser (8000)

1. Introduction

- *Surface wind plays a crucial role in many local/regional weather and climate processes and helps to shape the global climate system.*
- *The NASA Cyclone Global Navigation Satellite System (CYGNSS) mission provides near surface wind speed over the tropical ocean with sampling that accounts for the diurnal cycle and heavy precipitation conditions.*
- *Our project includes a validation effort using Tropical buoy data to quantitatively characterize and validate CYGNSS surface wind data.*
- *Using the CYGNSS validated wind speeds, we will then use the data for diagnostic and model evaluation studies on multi-scale interactions in the Maritime Continent (MC) region of the Tropics, with a particular focus on the Madden-Julian Oscillation (MJO), equatorial waves, and the diurnal cycle.*
- *This presentation shows our validation results between CYGNSS and in-situ global oceanic wind data.*
- *This validation will help account for low wind speed mission level requirements (Ruf et al. 2019).*

2. Data and Methods

•CYGNSS level-2 (v2.1; CYGNSS, 2018) surface wind speeds from March 18th, 2017 to Dec 31st, 2018.
•Tropical Moored Buoy Arrays (**Fig. 2**) were incorporated to validate the CYGNSS surface winds.
•For the validation, CYGNSS data were matched and compared to the nearest station within 25 km radii and +/- 30 minutes as follows:

$$CYGNSS_{wind}(x) = \sum_{i=1}^{n} wix\, i \,/\, \sum_{i=1}^{n} wi$$

$$w = 1/(x^2 + U^2 x\, t^2)0.5$$

Boutin & Etcheto (1990)

x – distance from the satellite measurement to the buoy location
U – buoy wind speed (hourly averaged here)
t – time difference between the measurements

- Buoy wind speed adjusted to 10m height following Monin-Obukhov similarity theory.
- CYGNSS QC-Flags:
  RCG <=3 & Block II-F excluded

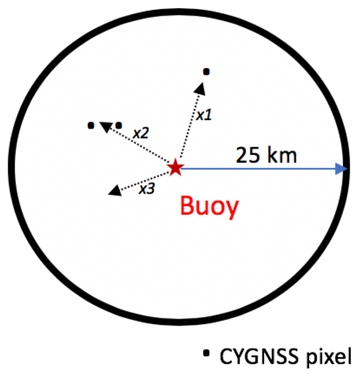

***Figure 1**. Schematic diagram showing the CYGNSS and Buoy matchup criteria within +/- 30 minutes threshold*

3. Validation Results

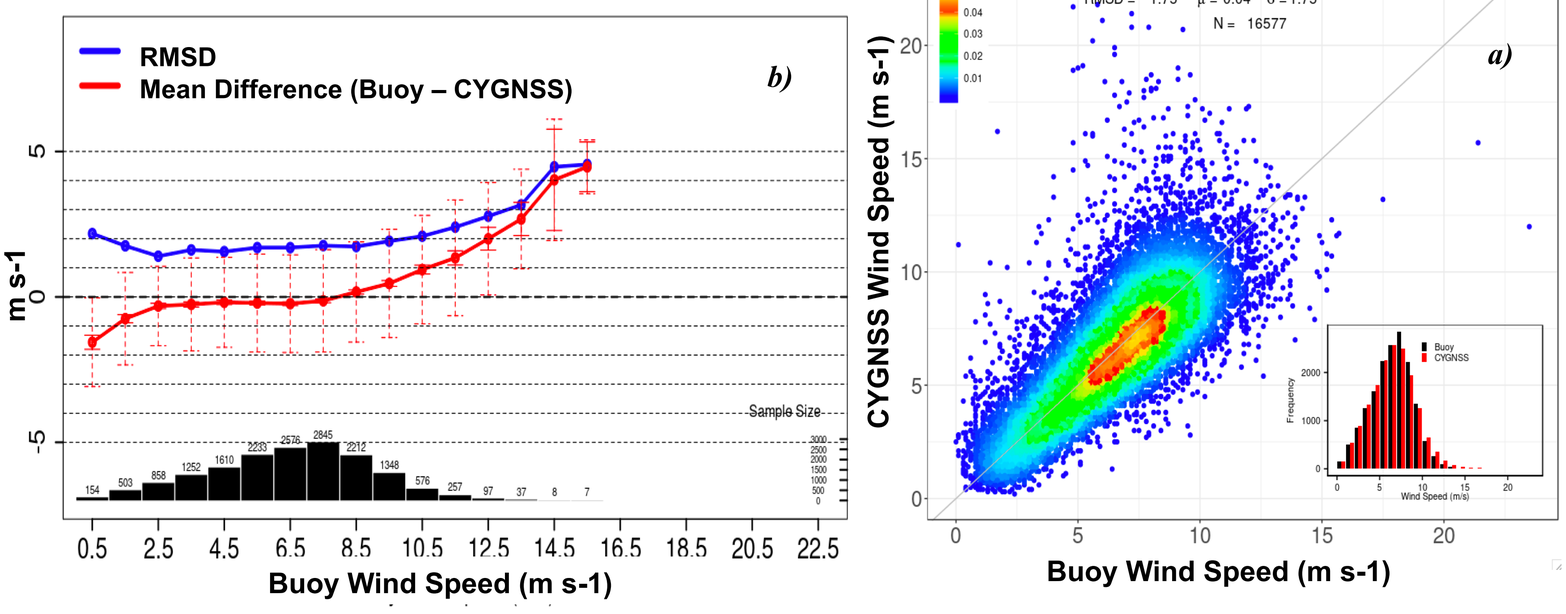

Fig 4. (a) 2D-density plot of collocated CYGNSS and tropical buoy wind speeds. The diagonal gray line is the 1:1 agreement. The statistical parameters RMSD, μ, σ, and N are the root mean square difference (Buoy – CYGNSS), mean bias, standard deviation of the difference, and the total sample size of the collocated CYGNSS and buoy wind data, respectively. (b) RMS (blue line) and mean (red line) difference between collocated buoy and CYGNSS wind speeds as a function of buoy wind speed. The error bars correspond to the 95 % confidence limit (solid line) and one sigma level (dotted). These metrics were computed over a ±0.5 m s-1 bin width for every 1 m s-1 buoy wind speed. Dashed horizontal lines tick the y-axis at 1 m s-1 wind interval. The light gray bars and label on top of each bar indicate the sample size in each group of ±0.5 m s-1 bin-width.

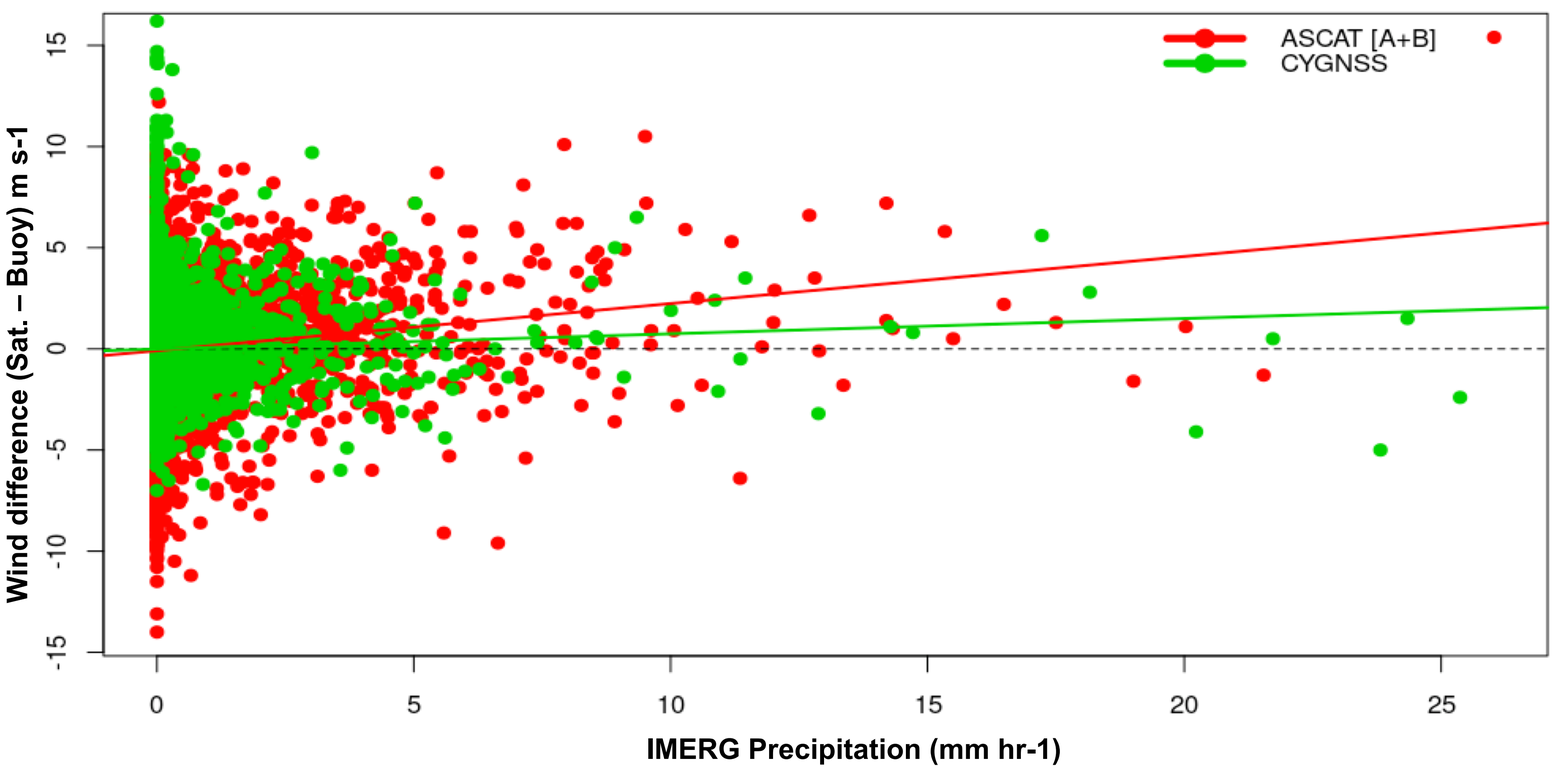

***Figure 5**. Scatterplot of CYGNSS and ASCAT (both A and B) winds at the analyzed buoys (negative means buoy values are higher) as functions of IMERG (v05, March 18th, 2017 to June 30th, 2018) precipitation rate at the same locations. Also shown are best-fit lines.*

3. Validation Results (*Contd..*)

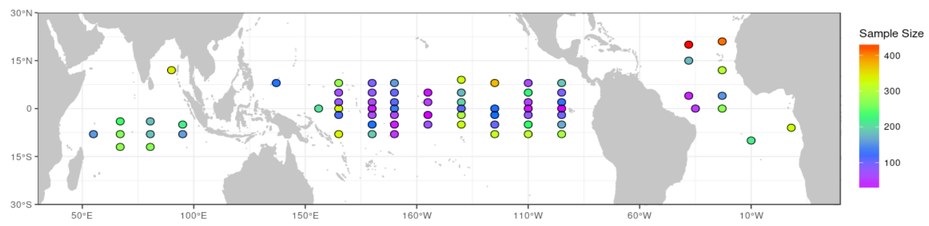

***Figure 2**. Collocated CYGNSS and buoy (March 18th 2017 to August 23rd 2018) sample size in Tropical Moored Buoy Array: PIRATA (Prediction and Research Moored Array in the Tropical Atlantic), RAMA (Research Moored Array for African-Asian-Australian Monsoon Analysis and Prediction), and TAO (Tropical Atmosphere Ocean)/TRITON (Triangle Trans-Ocean Buoy Network). More details on the tropical buoys are given on the NOAA/PMEL website <https://www.pmel.noaa.gov/gtmba/mission>*

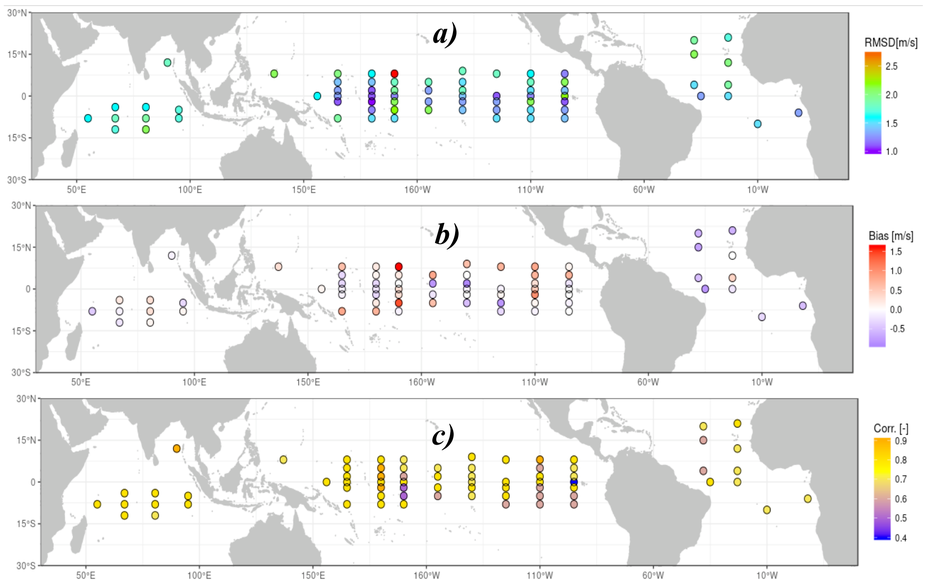

***Figure 3**. Statistical parameters: **(a)** root mean square difference **(b)** bias [CYGNSS-Buoy] **(c)** Correlation Coefficient between CYGNSS & Buoy winds at each matchup location*

4. Summary

- In many cases CYGNSS surface winds observation are consistent with co-located buoy data, although there are some differences
- Compared to the buoy values, CYGNSS exhibits a slight overestimation at lower wind speeds and an underestimation in the higher wind range
- The errors in CYGNSS, largely at the higher range, are wind dependent
- CYGNSS has least effect in rain compared to ASCAT
- More validation analyses are in progress (Asharaf et al., 2019)

Poster No. EB-13

National Aeronautics and Space Administration
Jet Propulsion Laboratory
California Institute of Technology
Pasadena, California

www.nasa.gov

References

- Asharaf S., D.E. Waliser, C. Zhang, A.W. Putra, D. J. Posselt, and C. Ruf: CYGNSS Ocean Surface Wind Validation in Tropics, J. Ocean Atmos. Tech., In preparation.
- Boutin, J., J. Etcheto, 1990: Seasat scatterometer versus scanning multichannel microwave radiometer wind speeds: A comparison on a global scale. J. Geophys. Res., 95(C12), 22275–22288, doi: 10.1029/JC095iC12p22275.
- CYGNSS. 2018. CYGNSS Level 2 Science Data Record Version 2.1. Ver. 2.1. PO.DAAC, CA, USA. Dataset accessed [2019-01-28] at https://doi.org/10.5067/CYGNS-L2X21.
- Ruf C., S. Asharaf, R. Balasubramaniam, S.Gleason, T. Lang, D. McKague, D. Twigg, and D. Waliser, 2019: On-Orbit Performance of the CYGNSS Hurricane Satellite Constellation. BAMS, in press.

National Aeronautics and Space Administration

Deep Convective Evolution from Shallow Clouds over the Tropical Rainforests

Author: Sudip Chakraborty (329J) Jonathan H Jiang (329J), Hui Su (329D)

Motivation:

- Amazon and Congo are the two largest rainforests that are vulnerable to droughts, deforestation, and climate change. Rainfall is tremendously important for the sustainability of these rainforests.
- It is expected that the African drylands might intrude southward under a warming climate [*Feng and Fu*, 2013].
- Thus, it is important to understand the mechanism behind the evolution of afternoon shallow convection to evening deep convection over the two regions.

Data and Methodology:

- After Shallow clouds are detected from Cloudsat.
- Evening-time deep convection is detected from the Global Precipitation Measurement (GPM)

Afternoon Cloud Information:	
Detect cloud top height of shallow clouds ($CTH_{afternoon}$)	CloudSat
Calculate rain rate associtaed with shallow clouds	GPM Imerg
Aerosol optical depth, Aerosol Pixels	MODIS, CALIPSO
Water vapor surrounding shallow clouds	AIRS
Evening Cloud Information:	
Convective available potential energy	MERRA -2
Relative Humidity	MERRA-2
Deep convective top height ($CTH_{evening}$)	GPM 2BCMB
deep convective latent heating	GPM 2SH

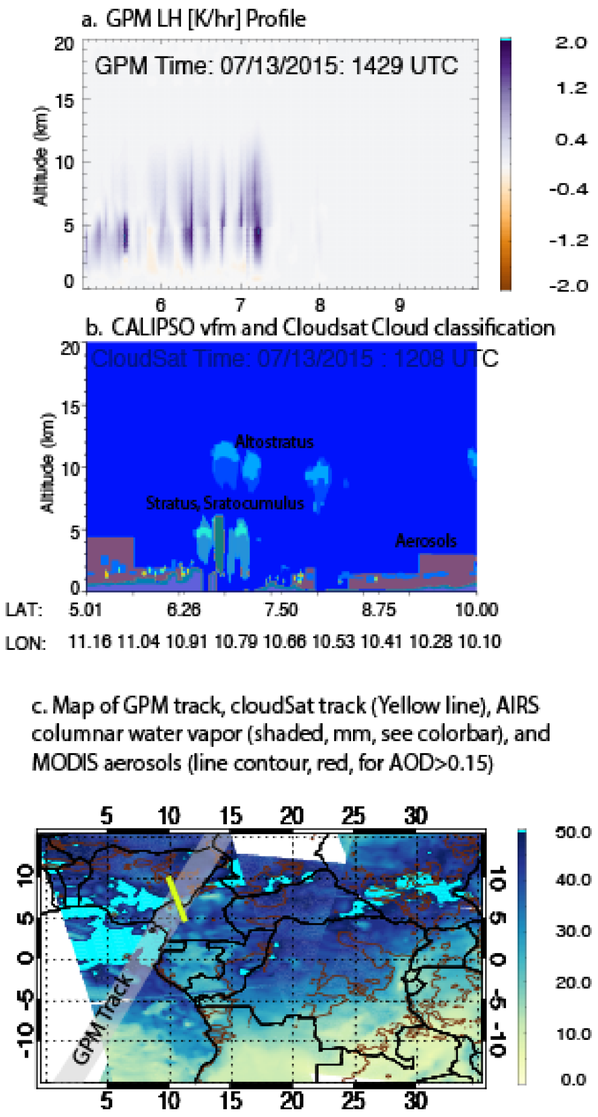

Figure 1

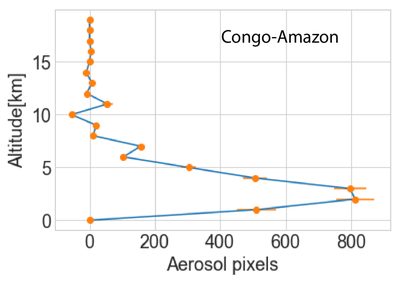

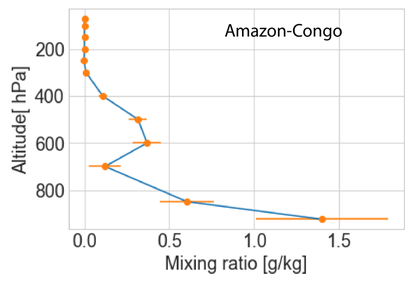

Figure 2

Differences in (a) Number of aerosol pixels from CALIPSO (Congo –Amazon) and (b) AIRS mixing ratio [g/kg] (Amazon-Congo) associated with shallow convection. Percentage of error bars are shown.

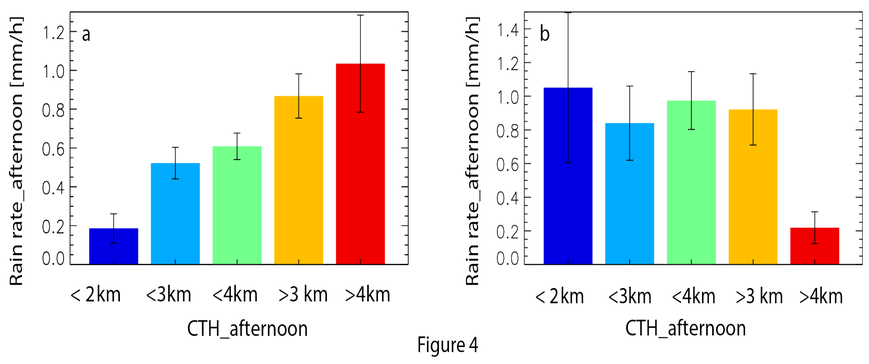

Figure 4

Mean and standard errors of GPM IMERG rain rate ($RR_{afternoon}$, mm/h) at 1330, 1400, and 1430 pm over (a) Congo and (b) Amazon within ± 0.1° from the location of CloudSat stratocumulus and stratus clouds.

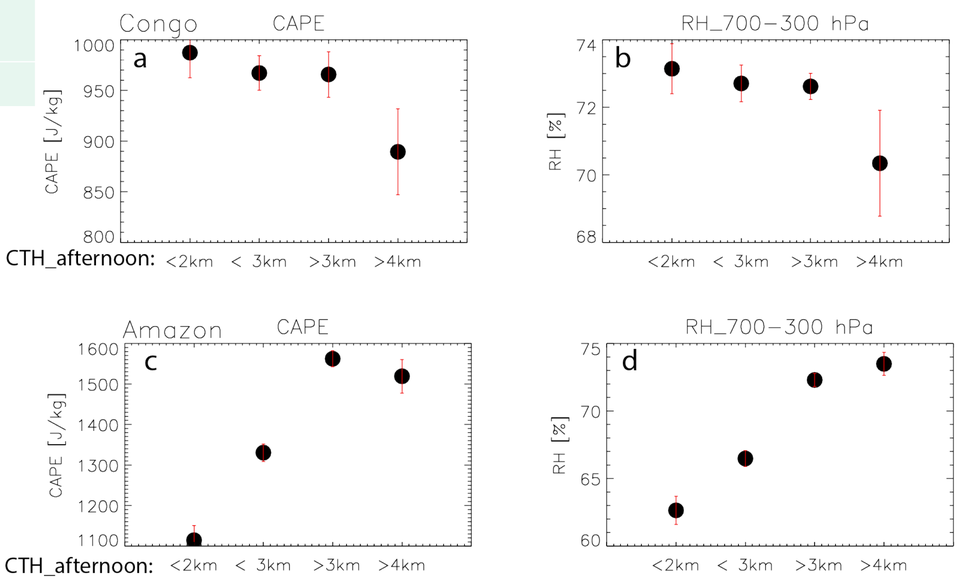

Figure 5

Mean and standard errors of CAPE (a, c), and $RH_{700\text{-}300}$ (b, d) over the Congo (a, b) and Amazon (c, d) regions at 3 pm local time for $CTH_{afternoon}$ < 2km, $CTH_{afternoon}$ < 3 km, and $CTH_{afternoon}$ > 3km.

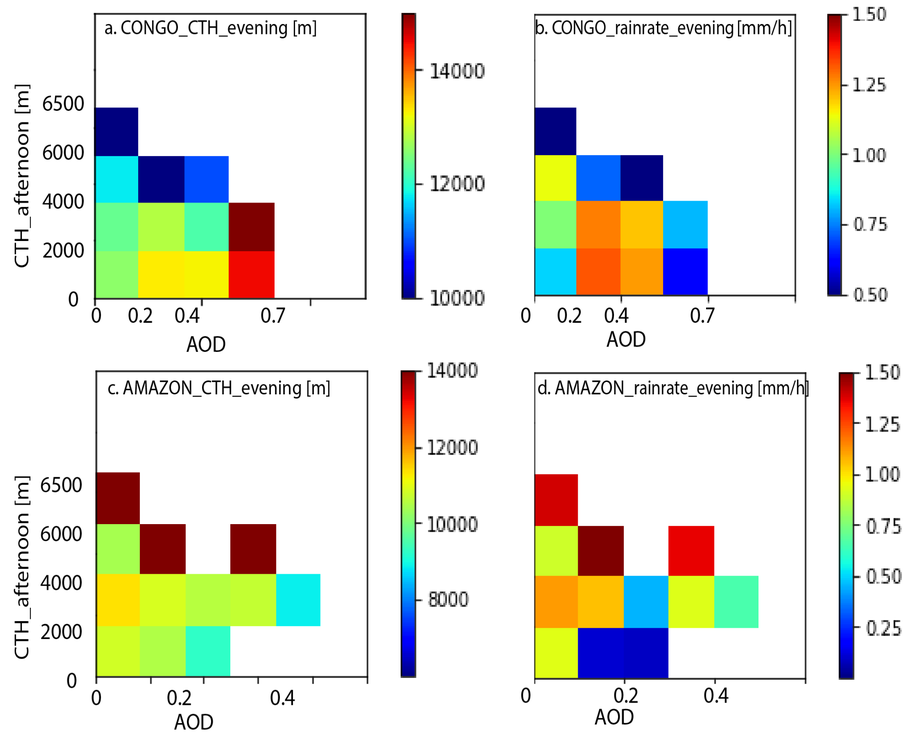

Figure 3.

Contours of $CTH_{evening}$ in meter (a, c) and $RR_{evening}$ in mm/h (b, d) over the Congo (a, b) and Amazon (c, d) regions as a function of CloudSat Cloud top height in m (Y axis) and TERRA AOD (X axis).

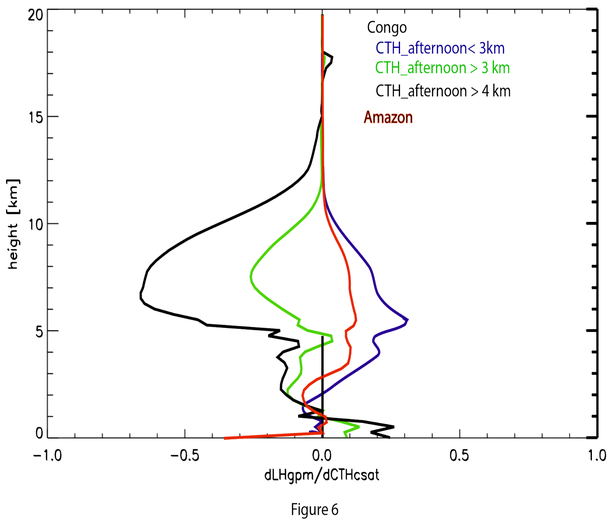

Figure 6

The rate of change of GPM LH with CloudSat $CTH_{evening}$ over the Congo region for $CTH_{afternoon}$ < 3km (blue line), $CTH_{afternoon}$ > 3km (green line), $CTH_{afternoon}$ > 4km (black line) and over Amazon (red line) region.

Take Home:

- ❑ Our results suggest that the afternoon shallow clouds over the Congo region suppress evening deep convection, weaken the evening storm top height and rain rate.
- ❑ On the contrary, shallow clouds over the Amazon region promote growth of the evening deep convective cloud.

Congo: Deeper clouds Rain more between 130:230 pm → Stronger rainfall in the afternoon could deplete moisture in the troposphere, cool down the ground and the surrounding atmosphere due to the evaporation of hydrometeors → **SCMP** is absent over the Congo basin owing to 1. dry air intrusion from Sahara above 850 hPa. 2. shallow clouds are surrounded in a dry environment over → CAPE and Free tropospheric humidity decrease around 4-5 pm. → condensation inside deep convection decreases as $CTH_{afternoon}$ increases. → Deep convective top height ($CTH_{evening}$) reach 10-12 km.

Amazon: Deeper clouds Rain doesn't change with $CTH_{afternoon}$ → Shallow clouds moistens the free troposphere and increase instability, and destabilize the free troposphere due to **shallow convective moisture pump (SCMP)** mechanism (Wright et al. 2017). → CAPE and Free tropospheric humidity increase around 4-5 pm. → condensation inside deep convection increases as $CTH_{afternoon}$ increases. → Deep convective top height ($CTH_{evening}$) reach higher (>14 km) altitude

National Aeronautics and Space Administration
Jet Propulsion Laboratory
California Institute of Technology
Pasadena, California

www.nasa.gov

Poster No. EB-14

National Aeronautics and Space Administration

3D cloud tomography using MISR data: defining the "veiled" core

Author: Linda Forster (329J and LMU, Munich)
Anthony B. Davis, David J. Diner (329J), Bernhard Mayer (LMU, Munich)

Motivation: Gap in operational cloud property retrievals

State of the art:
Operational satellite **retrievals of global water cloud** optical thickness τ and droplet effective radius r_{eff} are based on the dual-wavelength Nakajima-King method [1], **assuming horizontally uniform (1D) cloud layers**.
→ This assumption leads to **retrieval failure for 3D convective clouds** with failure rates up to 60% [2].

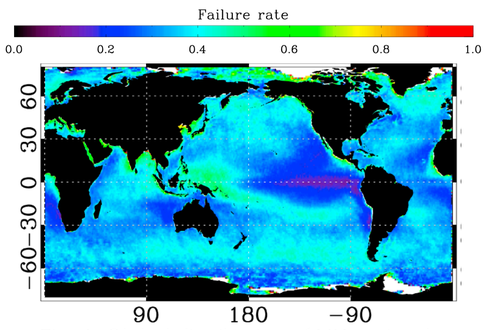

Fig. 1: Global distribution of NK retrieval failure rates at MODIS 2.1 μm channel [2].

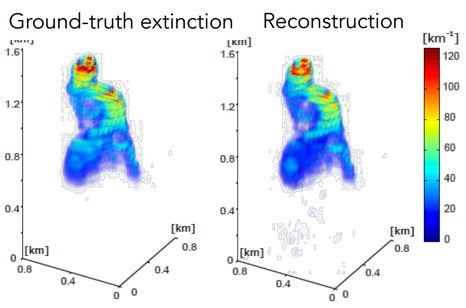

Fig. 2: Demonstration of cloud reconstruction using JPL LES cloud from synthetic AirMSPI observations [3].

Shift of paradigm:
- **Retrieve 3D volume** of cloud properties using **tomographic reconstruction** from **multi-angle observations** as demonstrated by [3].
- The **reconstruction** is treated as a large **inverse problem** with a **3D radiative transfer (RT) solver** as a forward model.

Objective: 3D cloud tomography from space

Adapt existing 3D cloud reconstruction method to satellite observations of MISR

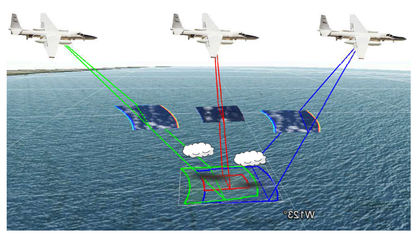

Fig. 3: AirMSPI on ER2 aircraft [3].

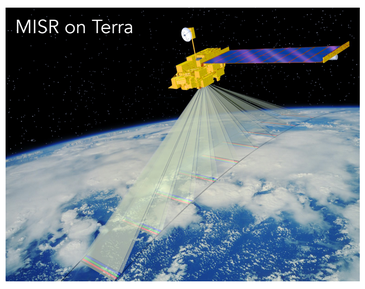

Fig. 4: MISR orbit, Source: NASA.

Spatial resolution increases 14-fold from 20 m (AirMSPI [4]) to 275 m (MISR [5]).

Challenges:
- **Optically thick pixel volumes** pose a challenge for 3D radiative transfer model
- **Unresolved spatial variability** of cloud microphysics increase the number of unknowns of this already ill-posed inverse problem.

Approach: Find and exploit "veiled" core inside convective clouds for 3D reconstruction

Finding the veiled core: systematically manipulate the core of the reference cloud at selected optical distances and compare observed MISR radiances.

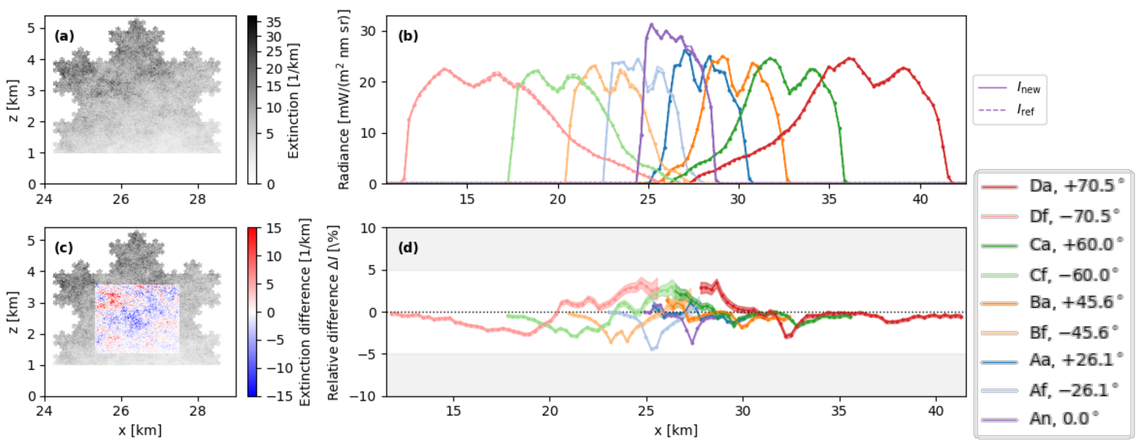

Fig. 4: (a) Extinction field of **idealized convective cloud with Brownian turbulence**. (b) **Observed MISR radiances simulated with** 3D Monte-Carlo radiative transfer model **MYSTIC** [6] ($\lambda = 670nm$, $r_{eff} = 10\mu$m, $\tau = 20$, $SZA = 0°$). Line widths correspond to a Monte-Carlo noise with 2σ standard deviation. (c) Extinction difference and (d) relative **difference between manipulated and reference cloud radiances**.

- The **relative differences** of the MISR radiances **decrease with increasing optical distance** between cloud surface and manipulated core (Fig. 5).
- The **veiled core** is defined **where** the **relative differences** of the radiances fall **below** MISR's **sensitivity to** change, set here at 5%.

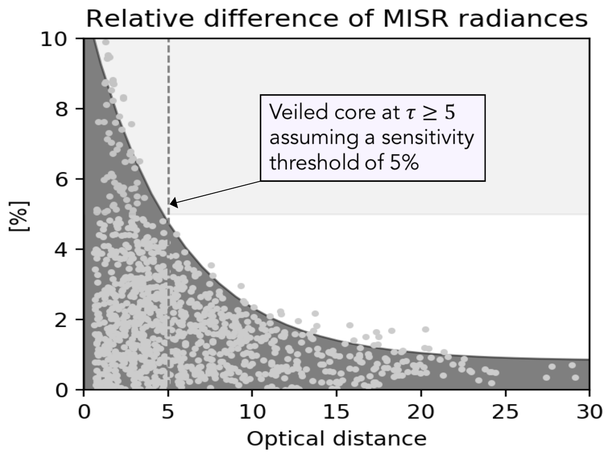

Fig. 5: Relative difference of MISR radiances as a function of optical distance inside the cloud along the camera's line of sight.

Hypothesis

Optically thick clouds have a **"veiled" core,** where **details** of the liquid water distribution **do not significantly contribute** to satellite observations.

→ Details are smoothed out **by multiple scattering** in the cloud.

Results

Assuming a **sensitivity threshold of 5% for MISR, the veiled core is located at an optical distance $\tau \geq 5$** inside the cloud.

→ Changes in the **details of the liquid water distribution inside this zone are within the instrument's noise**, as long as mean, variance and correlations are preserved.

Application: Efficient radiative transfer … and dimensionality reduction

Details of the liquid water distribution inside "veiled" core do not contribute significantly to observations.

→ **Photon Diffusion Theory (PDT)** can be applied inside the core **to speed up the radiative transfer** (RT) **forward model** of the tomographic cloud reconstruction.

→ Compare detailed RT to **Hybrid model:** DISORT [7] for detailed RT in the cloud shell & PDT inside the "veiled" cloud core (Fig. 6).

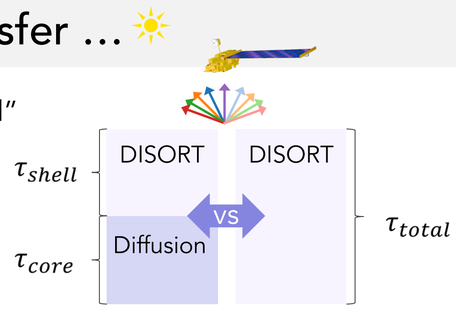

Fig. 6: Hybrid model vs. pure DISORT.

Simulations (Fig. 7): Optical thickness of cloud shell τ_{shell} is increased from 0 (pure PDT) to τ_{total} (pure DISORT) for different parameters.

→ For $\tau_{shell} \geq 6$ the relative error between the hybrid model and DISORT is $\leq 5\%$, i.e. within instrument noise: veiled core!

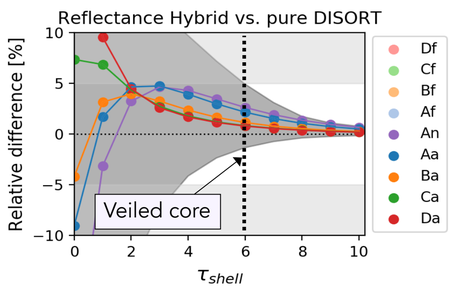

Fig. 7: RT simulations for $\tau_{total} = 10, 20, 40$; $r_{eff} = 5, 10, 15\ \mu$m; $SZA = 0°, 60°$.

Save computational time for solving the inversion by reducing number of unknowns.

The veiled core in 3D:

→ The veiled core covers **more than 10% of the cloud volume** (black voxels in Fig. 8) for the LES cloud, shown in Fig. 2.

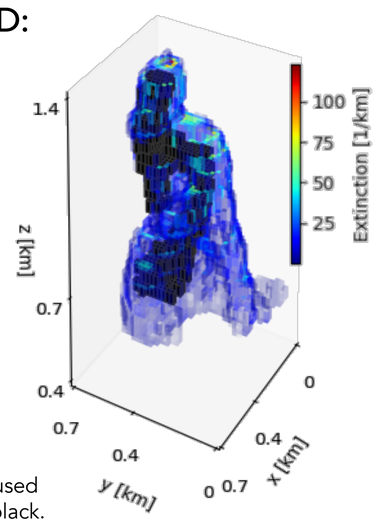

Fig. 8: Extinction of LES cloud used in [3]. Veiled core indicated in black.

Conclusions

Knowledge of the veiled core can **increase the efficiency of 3D cloud tomography** by:
- **Fast yet accurate radiative transfer** by applying Photon Diffusion Theory inside the veiled core.
- **Significant reduction of the number of unknowns.**

Acknowledgements: Funding acknowledged from the Horizon 2020 program for research and innovation under the Marie Skłodowska-Curie Grant Agreement No. 754388 and LMUexcellent No. ZUK22, and from NASA ROSES – TASNPP element (grant #105357).

National Aeronautics and Space Administration
Jet Propulsion Laboratory
California Institute of Technology
Pasadena, California

www.nasa.gov

References:
[1] Nakajima, T., and M. King, 1990: Determination of the optical thickness and effective particle radius of clouds from reflected solar radiation measurements. Part I: Theory. J. Atmos. Sci., 47, 1878–1893.
[2] Cho, H.-M., et al. (2015), Frequency and causes of failed MODIS cloud property retrievals for liquid phase clouds over global oceans, J. Geophys. Res. Atmos., 120, 4132–4154.
[3] Levis, A., Y. Y. Schechner, A. Aides, and A. B. Davis, 2015: Airborne Three-Dimensional Cloud Tomography. The IEEE International Conference on Computer Vision (ICCV).
[4] Diner, D. J., and Coauthors, 1998: Multi-angle Imaging Spectro Radiometer (MISR) instrument description and experiment overview. IEEE Transactions on Geoscience and Remote Sensing, 36, 1072–1087.
[5] Diner, D. J., and Coauthors, 2013: The Airborne Multiangle Spectro Polarimetric Imager (AirMSPI): a new tool for aerosol and cloud remote sensing. Atmos. Meas. Tech., 6 (8), 2007–202.
[6] Mayer, B., 2009: Radiative transfer in the cloudy atmosphere. European Physical Journal Conferences, 1, 75–99.
[7] Stamnes, K. and Coauthors, 1988: Numerically stable algorithm for discrete-ordinate-method radiative transfer in multiple scattering and emitting layered media. Appl. Opt. 27, 2502-2509.

Poster No. EB-15

National Aeronautics and Space Administration

NASA Satellites and a JPL Parameterization Constrain Physics Required for Accurate Simulation of Low Clouds and Rain

Author: Mark Smalley (329J)
Kay Sušelj (398K), Matthew Lebsock (329J), Joao Teixeira (3290)

I. Introduction

The Problem

- The representation of shallow maritime clouds in global circulation models constitutes a leading source of uncertainty in projections of Earth's future climate.
- What model physics are needed to capture relationships between low clouds and weather regime?

Our Solution for the JPL EDMF

- We adjust model physics of the JPL Eddy-Diffusivity/Mass-Flux (EDMF) in order to accurately simulate the relationship between low clouds and atmospheric stability.
- Global observations of cloud properties provided by NASA missions (CloudSat/CALIPSO, MODIS, CERES, AMSR-E) are used as a benchmark for model simulations of low clouds.

II. JPL Eddy-Diffusivity/Mass-Flux Parameterization

- JPL EDMF parameterizes sub-grid scale atmospheric physics (Smalley et al. 2019) within a large-scale model.
- A single-moment microphysics package is coupled to updraft dynamics, with prognostic total H_2O and θ_L.

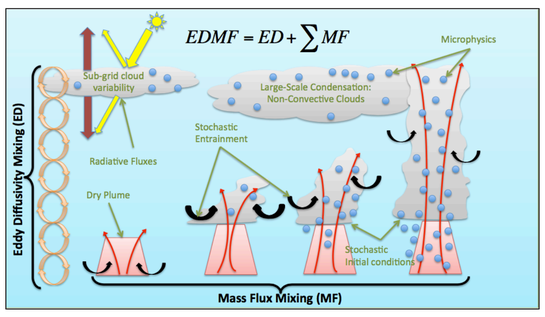

III. Which Parameters Control Cloud and Radiation Budgets?

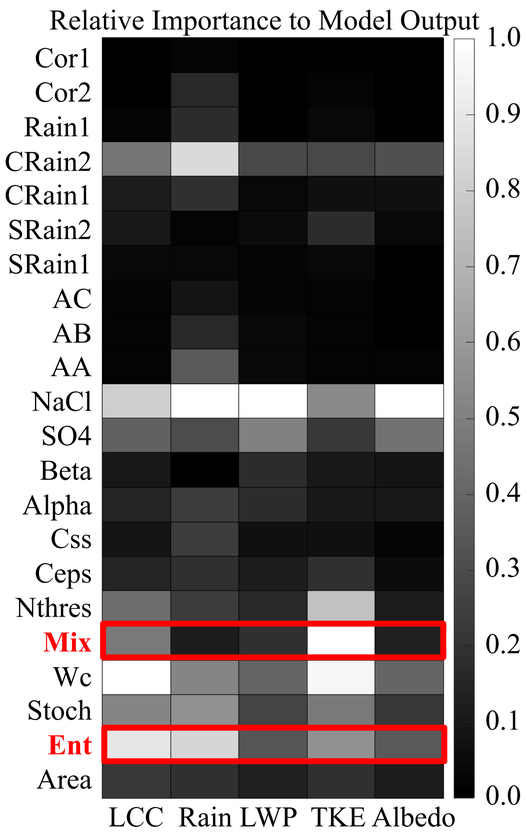

- Morrison One At a Time (MOAT) analysis reveals several parameters that are important to model outputs (Low Cloud Cover (LCC), Rain Rate, Liquid Water Path (LWP), Turbulent Kinetic Energy, and Top-of Atmosphere Albedo).
- For now, we investigate the behavior of two parameters.
- Ent controls entrainment in updrafts and is most important in unstable conditions.
- Mix controls turbulent mixing and is most important in stable conditions.

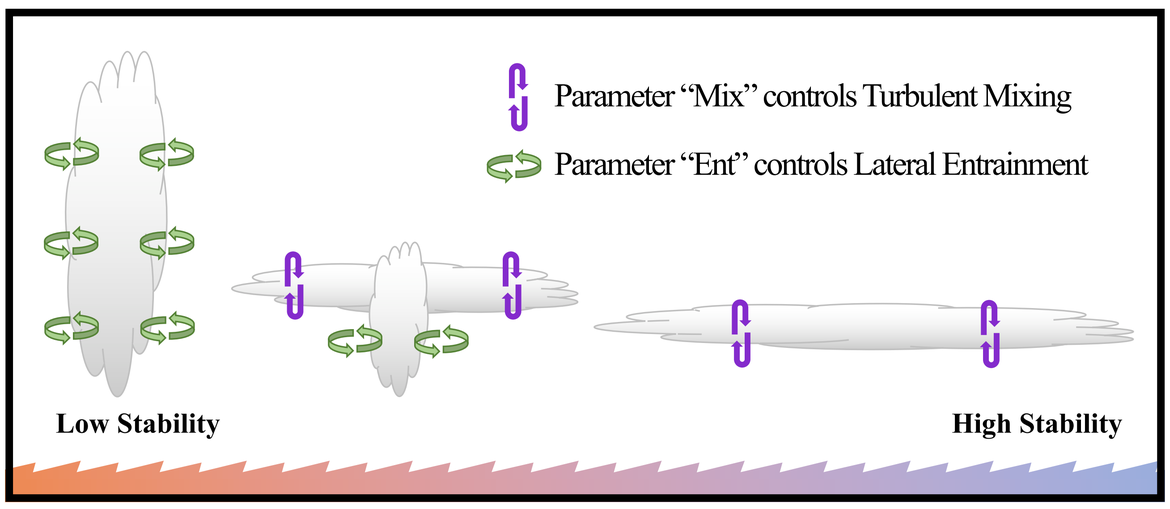

IV. Model Evaluation Strategy

- Initial conditions are provided by the NASA MERRA2 reanalysis along the orange polygon.
- 2000 individual EDMF profiles are run for 3 model hours within a single column model for each candidate parameter value.
- Assessment is performed at the end of the simulation by comparison to co-located NASA observations.

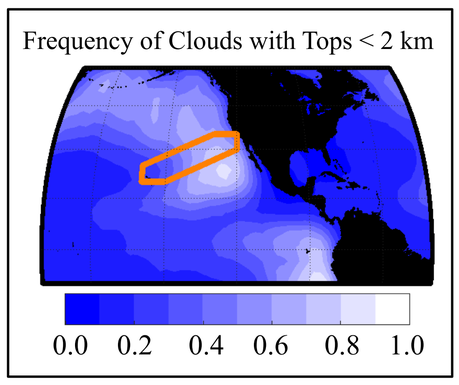

V. Parameter Selection

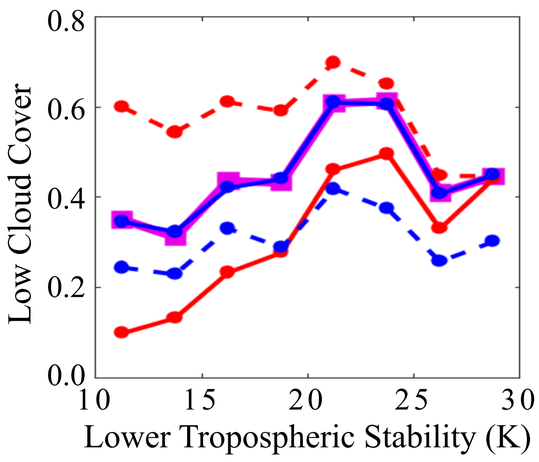

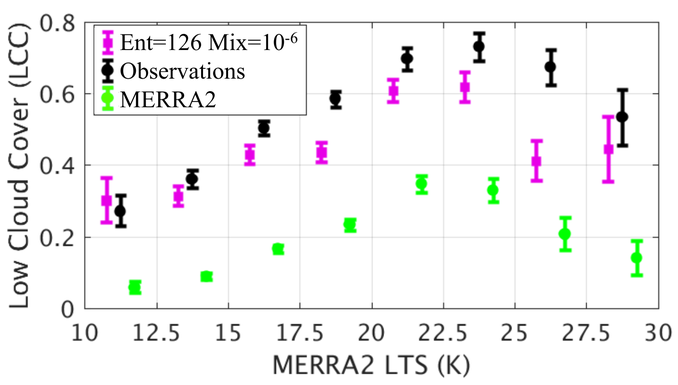

Inspection of low cloud cover as a function of stability reveals a winner with mid-range Ent and low Mix!

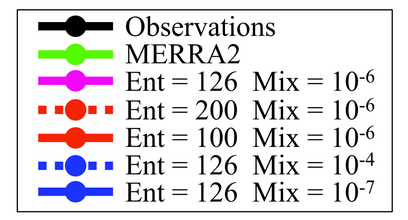

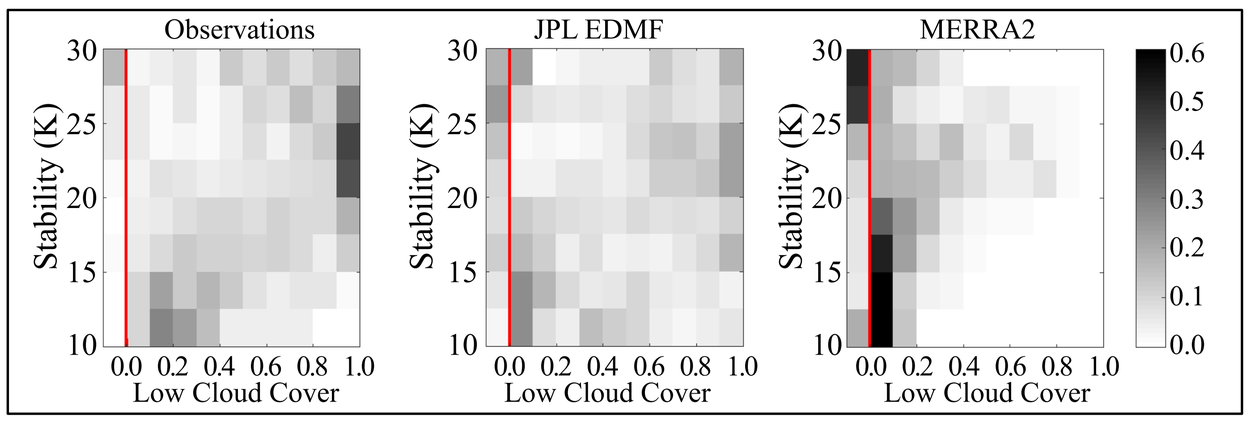

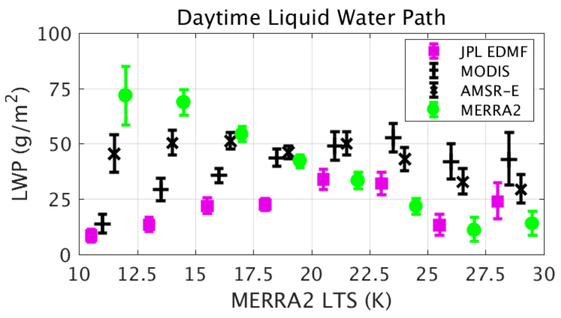

JPL EDMF clouds, rain, and radiation from JPL EDMF show improvement over MERRA2.

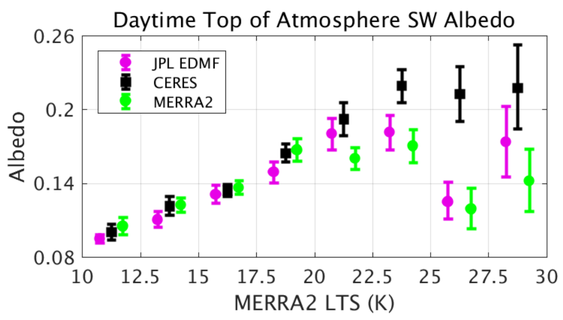

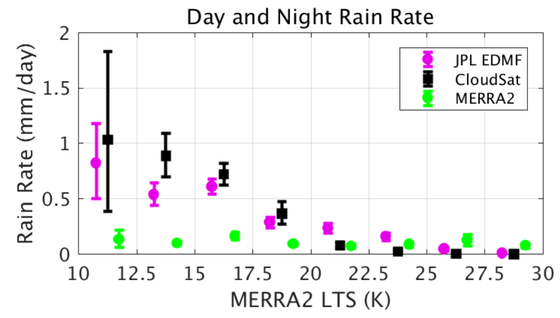

VI. Conclusions

- ✓ Accurate parameterization of both entrainment and turbulent mixing are required for reliable simulations of low cloud cover, a key element in understanding climate change.
- ✓ MOAT sensitivity analyses (MOAT) identified several important model parameters.
- ✓ Two parameters were tested and the ideal parameter combination was identified.
- ✓ JPL EDMF shows improvement over MERRA2, which produces too few clouds.

References

Smalley, M. A., K. Sušelj, M. D. Lebsock, and J. Teixeira, 2019. A novel framework for evaluating and improving parameterized subtropical marine boundary layer cloudiness, *Monthly Weather Review*. In Review.

This research is funded by NASA CloudSat/CALIPSO science team funding to JPL under RTOP/WBS (105357/ 967701.02.01.02.08)

Poster No. EB-16

National Aeronautics and Space Administration
Jet Propulsion Laboratory
California Institute of Technology
Pasadena, California

www.nasa.gov

National Aeronautics and Space Administration

Ice dynamics and mass balance of Denman Glacier, East Antarctica

Author: V. Brancato (334)

E. Rignot (334), P. Milillo (334), M. Morlighem, J. Mouginot, L. An, B. Scheuchl, S. Jeong, P. Rizzoli, J. Bueso-Bello, P. Prats

Introduction

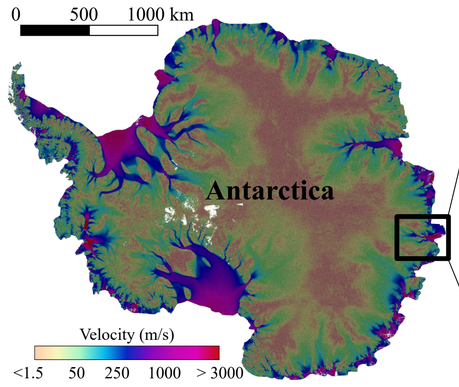

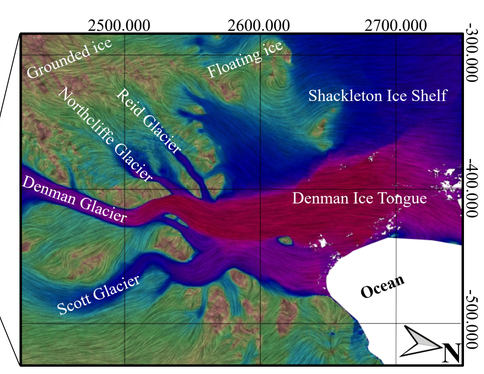

- Denman Glacier (DG) holds an ice volume equivalent to **1.5 m of sea level rise**
- thinned at 0.4±0.2 m/year in 2002-2011 and melts at 3.1±0.7 m/year [*1*]
- Information on its **grounding line** dates to 1996.

Methods

Grounding line mapping

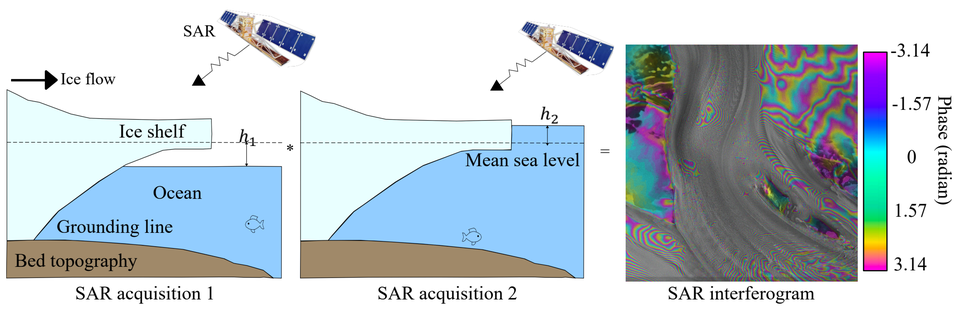

- SAR stands for Synthetic Aperture Radar
- Differencing SAR interferograms reveals **the vertical motion of ice in response to changes in oceanic tides** (Hp: steady horizontal ice motion) [*2*]
- Manual identification of inward limit of detection of ice tidal flexure

Ice velocity mapping

- **Feature tracking** using optical remote sensing (Landsat-4/7 legacy) [*3*]
- **Speckle tracking** for SAR remote sensing products from different missions

Elevation change rate

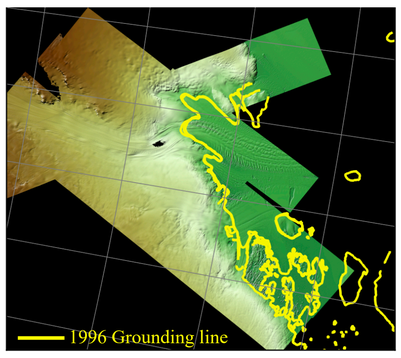

- Differencing **Digital Elevation Models** (DEMs) to compute [*4*]:
  - Changes in ice dynamics (grounded ice)
  - Ocean-induced melt (floating ice)
- TanDEM-X DEMs from 2011-2014
- DEMs calibrated to surface height with **NASA Operation Ice Bridge** altimetry

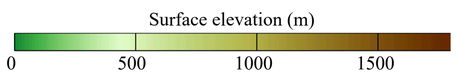

Materials

Used data

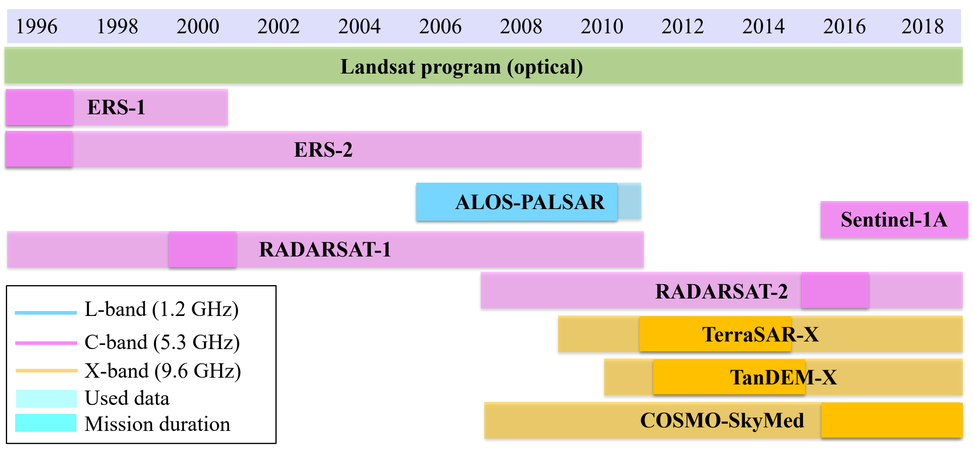

Oceanographic data

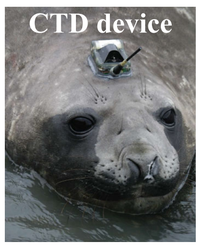

- Sea mammals instrumented with Conductivity, Temperature and Depth (CTD) devices [*5*]
- Time frame of observations:2004-2015
- Positioning accuracy ~ 4 km
- Temperature accuracy ~ 0.005°C
- Conductivity accuracy ~ 0.005 mS cm^{-1}
- Data publicly available: http://www.meop.net

Results

Grounding line and grounding zone mapping

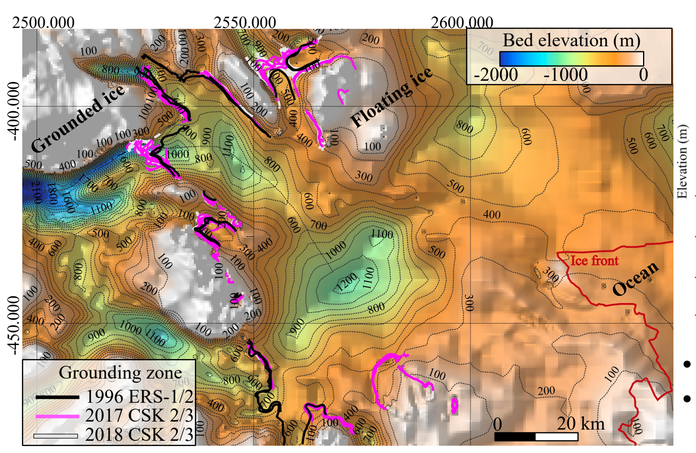

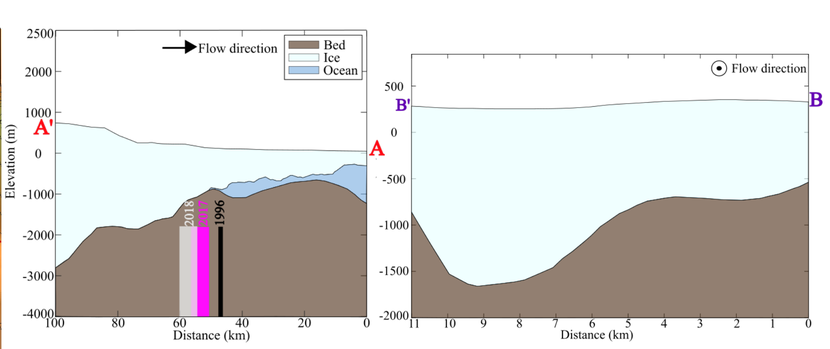

- Bed topography reconstructed using **mass conservation method** [*6*]
- Multiple grounding line measurements lead to a **grounding zone** i.e., a region when ice transitions from grounded to floating.

Elevation change rate

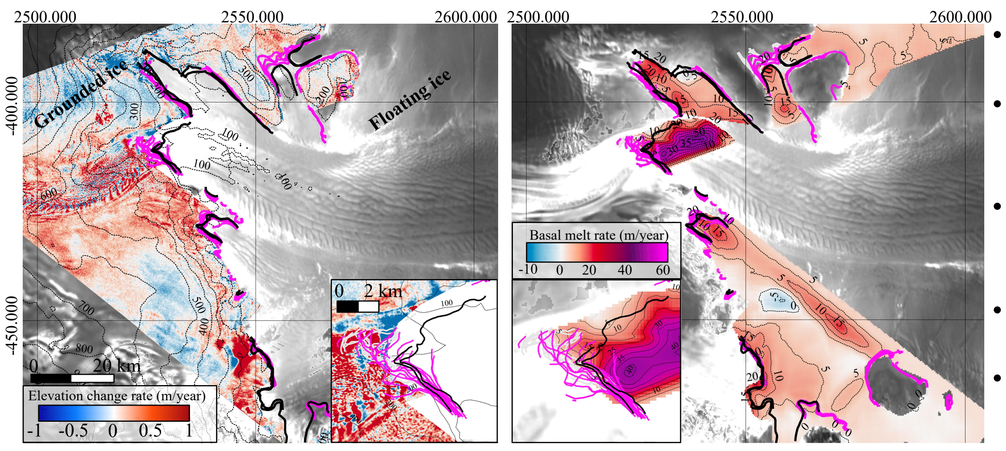

- DG main trunk **thinned at 0.4±0.1** m/year between **2011 and 2013**
- Thinning confined in the last 50-100 km coincident with speed-up (see below) i.e., **dynamic thinning**
- Ocean-induced ice shelf melt **exceeding 40 ± 4 m/year in 2011-2014** (Lagrangian approach)
- Average melt rate in East Antarctica is 0.7 **±0.4 m/year**
- Signature of the presence of **warm water** surrounding the ice shelf?

Difference in ice velocity 2017-1996

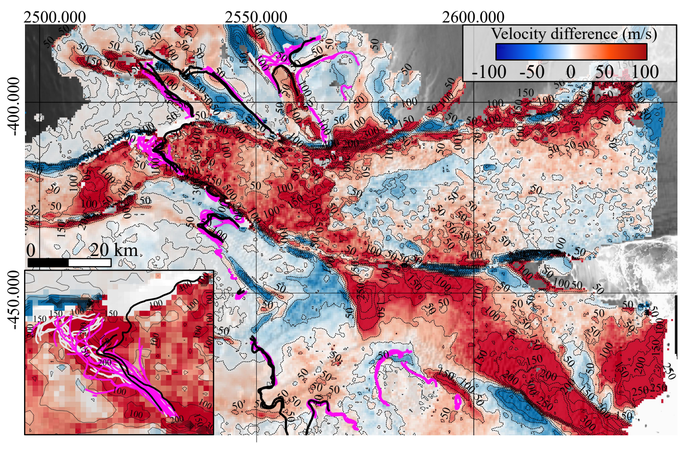

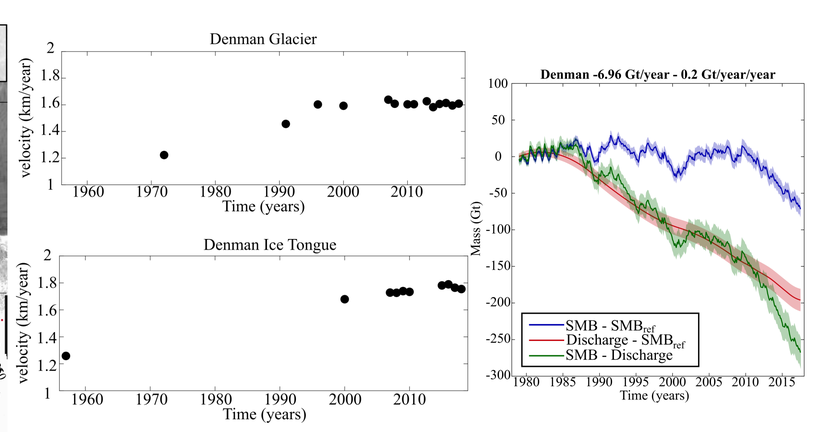

- DG has been speeding up by 16±2% since 1970 and the glacier is, at present ,10±2% out of balance
- Denman Ice Tongue sped up by 15% between 1996 to 2017, i.e. the ice shelf is **thinning dynamically**

Ocean temperatures

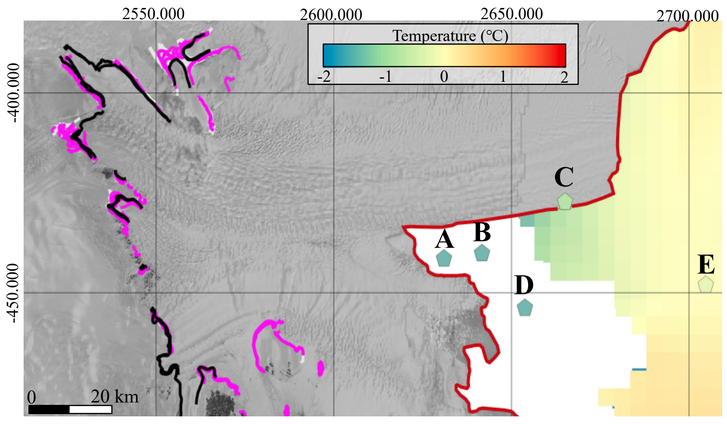

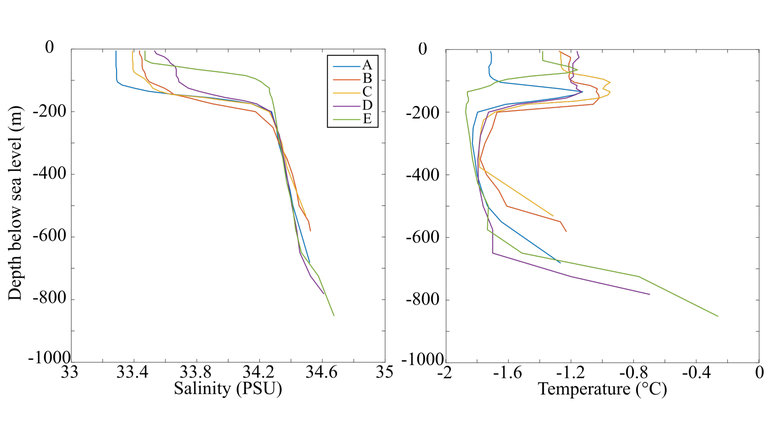

- Background ocean temperature is from *Southern Ocean State Estimate* at 310 m water depth
- **Few data in front of the ice shelf** all acquired in 2011 with maximum water depth between -600 to -800 m below sea level

Conclusions

- The extent of the grounding zone (±4km) indicate regular infiltration of ocean water on DG main trunk:
  - Pronounced migration magnitude not consistent with a hard bed: viscoelastic response of the bed?
- The observed warm water near Denman Ice Tongue can explain the high melt rate observed with TDX data
  - Is there a pathway for this **warm water** to infiltrate the sub-ice shelf cavity and melt the glacier from below?
  - No bathymetric data in the surrounding of Denman Ice Tongue: using MEOP depth data to reconstruct the bathymetry?

References

[1] T. Flament, F. Remy, Dynamic thinning of Antarctic glacier from along-track repeat radar altimetry. *J. Glaciol*. **58,** 830-840 (2012).
[2] E. Rignot, J. Mouginot, B. Scheuchl, Antarctic grounding line mapping with differential SAR interferometry. *Geophys. Res. Lett.* **38**, L10504 (2011).
[3] J. Mouginot, E. Rignot, B. Scheuchl, R. Millan, Comprehensive annual ice sheet velocity using Landsat-8, Sentinel-1, and RADARSAT-2 data. Rem. Sens. **9**, 364-374 (2017).
[4] P. Milillo, E. Rignot, P. Rizzoli, B. Scheuchl, J. Mouginot, J. Bueso-Bello, P. Prats, Heterogeneous retreat and ice melt of Thwaites Glacier, West Antarctica, *Sci. Adv.* **5,** eaau3433 (2018).
[5] F. Roquet, G. D. Williams, M. A. Hindell, R. Harcourt, C. McMahon, C. Guinet, J. B. Charassin, G. Reverdin, L. Boehme, P. Lovell, M. Fedak, A Southern Indian Ocean database of hydrographic profiles obtained with instrumented elephant seals. *Nature Sci. Data* **1**, 140028 (2014).
[6] M. Morlighem. E. Rignot, J. Mouginot, B. Scheuchl, E. Larour, H. Ben Dhia, D. Aubry, A mass conservation approach for mapping glacier ice thickness. *Geophys. Res. Lett.* **44**, L19503 (2011).

EB-17

National Aeronautics and Space Administration

Jet Propulsion Laboratory
California Institute of Technology
Pasadena, California

www.nasa.gov

National Aeronautics and Space Administration

Improving Satellite-Based Subhourly Surface Rain Estimates Using Vertical Rain Profile Information

Nobuyuki Utsumi (334H)
Hyungjun Kim (Univ. of Tokyo), F. Joseph Turk (334H), Ziad. S. Haddad (334H)

1. Motivation

- Accumulation (or average) of rain for appropriate time scales (e.g., 30-minutes) is important for various applications.
- However, low Earth orbit (LEO) satellite can provide only instantaneous observations.

2. Objective

To propose a new idea to estimate sub-hourly (~30min) surface rain averages using LEO-based instantaneous observations.

3. Projecting Vertical Rain Information over Temporal Domain

- Rain rate at upper levels can be correlated to the surface rain rate with time delays.
- If the effects of microphysical processes (e.g., evaporation of rain particles) are sufficiently small, the time variation of surface rain can be approximated by the vertical variation of rain profile.

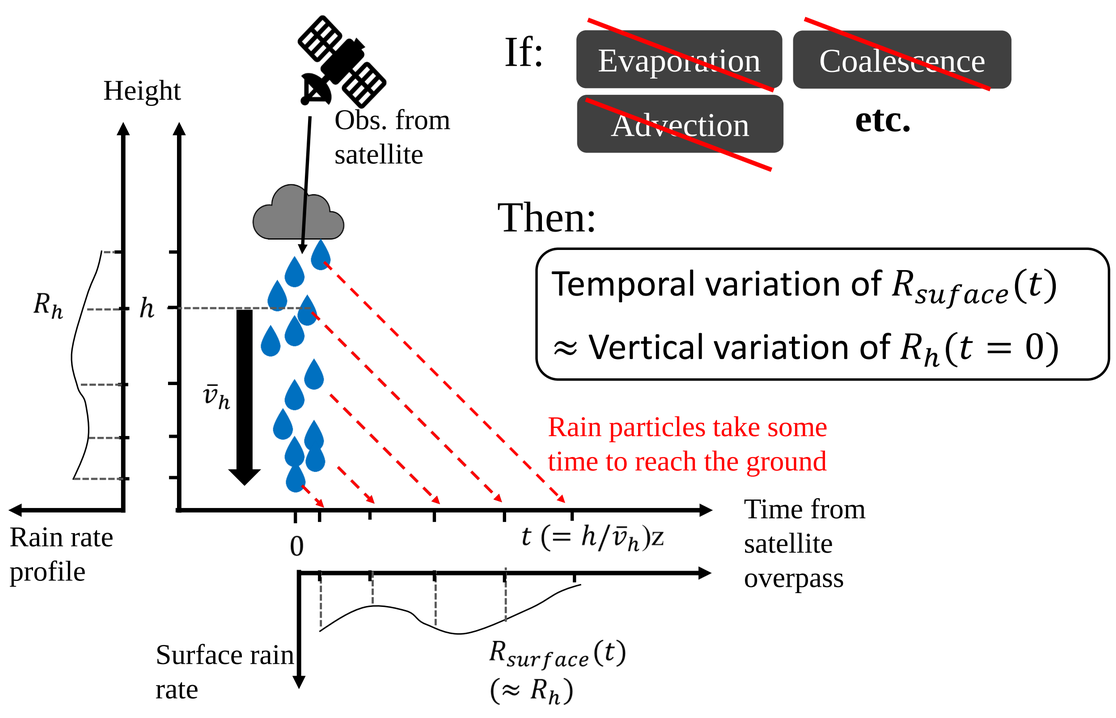

Fig. 1 Schematic image of the relationship between rain profile and surface rain rate (under idealized condition). t is the time from satellite overpass timing. R_h is the rain rate at h [km] at the satellite overpass timing (t=0). $R_{surface}(t)$ is the surface rain rate at the time of t. $\bar{v}_h$ is the mean falling velocity of the raindrops at the height of h falling to the surface.

4. Data and Method

- TRMM/PR 2A25 V7
  (rain vertical profile & inst. surface rain)
- 1-minute rain gauge data over over US
  (TRMM Ground Validation gauge data)
- April – October, 2005 – 2014.
- Rain gauge observations near the PR footprint are averaged and matched with TRMM/PR

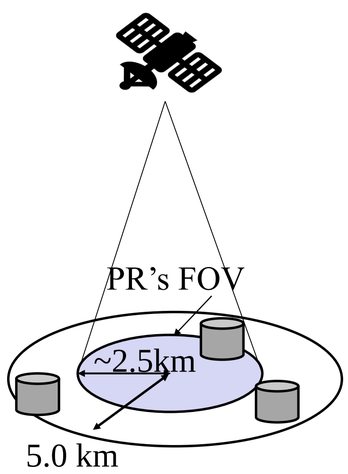

Fig. 2 Schematic image of TRMM/PR and gauge match up.

5. Time-lagged correlations

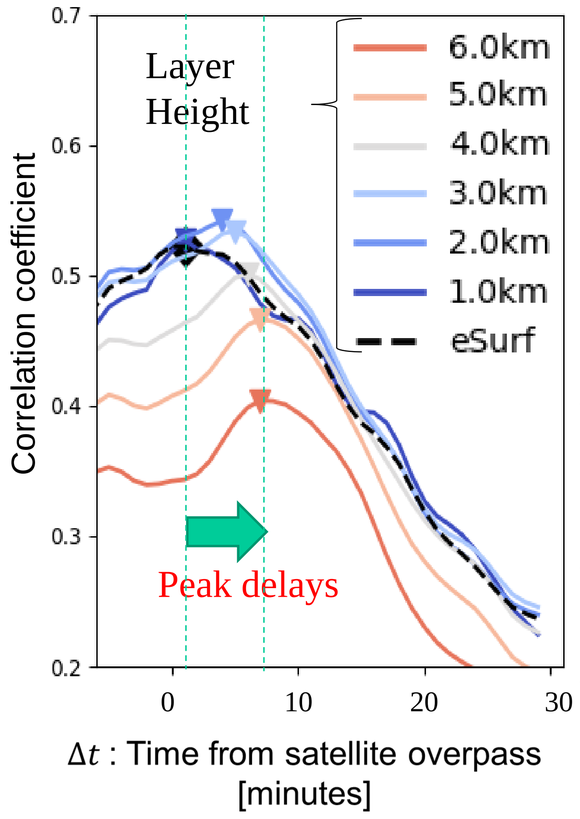

Figure 3. Correlation coefficient between rain rate at h [km] ($R_h(t=0)$) and the surface rain rate at time of t= Δt after the satellite overpass($R_{surface}(t=\Delta t)$).

Correlations for various h (1.0 ~ 6.0km) and Δt (-5 ~ +30 minutes) are investigated.

- Rain rate at upper levels are correlated to surface rain rate with time delays.
- Correlation peak delays for upper layer rain rate.
- Upper layer rain rate has skills to infer "near future" surface rain rate.

6. Performance of proposed method

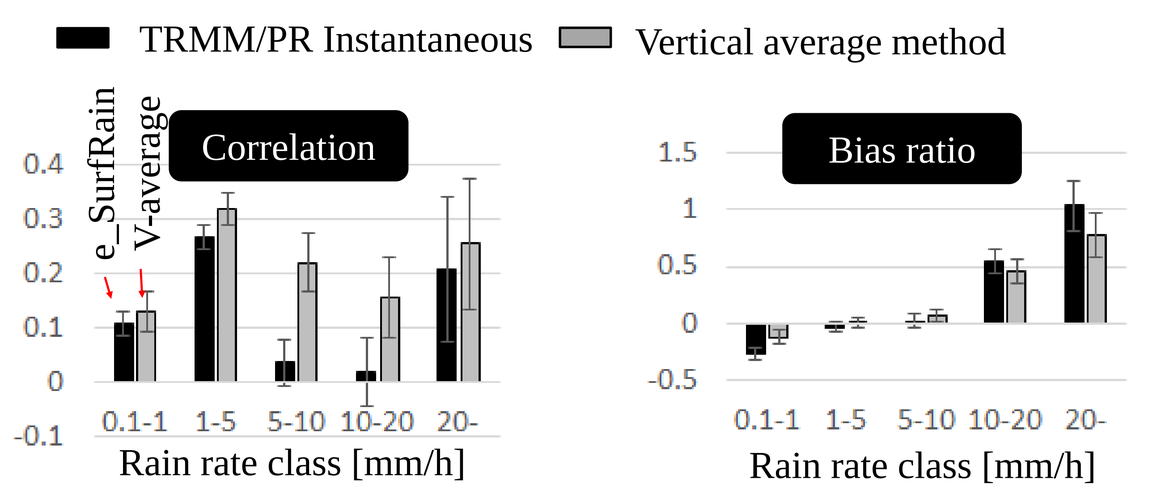

Figure 4. Performance of vertical average rain rate (surface to 4.5km) for representing time average (30min) surface rain rate.

Temporal average of $R_{suface}(t)$
≈ Vertical average of $R_h(t=0)$
?

Proposed method (vertical average) outperforms TRMM/PR instantaneous surface rain rate product for representing 30-min average of rain gauge rain rate.

7. Conclusion and Potential Applications

- Upper level rain rate has skills to infer near future (1 – 30 minutes) surface rain rate.
- Vertically-averaged rain rate outperforms e_SurfRain to represent sub-hourly surface rain rate.
- Potentially applicable to rain profile estimates from passive microwave (PMW) based retrievals.

Reference

Utsumi, N., H. Kim, F. J. Turk, and Ziad. S. Haddad, 2019: Improving Satellite-Based Subhourly Surface Rain Estimates Using Vertical Rain Profile Information. J. Hydrometeor., 20, 1015–1026

National Aeronautics and Space Administration
Jet Propulsion Laboratory, California Institute of Technology, Pasadena, California
www.nasa.gov

National Aeronautics and Space Administration

Patterns and dynamics of SST fronts in the California Current System

Yackar Mauzole (329B), Hector Torres Gutierrez (329C) and Lee-Lueng Fu (3200)

1. Context

CCS The California Current System (CCS) is one of the four major Eastern Boundary Current Systems in the ocean, along with the Peru/Chile Current System, the Canary Current System and the Benguela Current System. It typically extends from 50ºN to 20ºN, and up to 135ºW offshore. The CCS has been extensively studied over the last 50 years, and most of the dynamics of the region are well-known, especially regarding coastal upwelling.

Coastal upwelling From Spring to Fall, winds blow equatorward along the West Coast, displacing surface waters offshore. Waters at depth, which are cold and rich in nutrients are then brought up to the surface to replace the displaced waters. The combination of nutrient-rich waters with sunlight results in high biological productivity, making the region one of the major marine ecosystems of the US.

Science question Sea surface temperature (SST) fronts are narrow boundaries that separate waters with distinct SST, and are typically associated with coastal upwelling in the CCS, which occurs mainly off the Northwestern US and California. However satellite observations challenge the notion that the CCS dynamics are confined to the context of coastal upwelling. In fact, they show that SST fronts may be detected off Baja California, in late Summer and Fall - when the upwelling season ends. It is thus thought that **distinct frontal dynamics may be at play in the CCS**.

Objective The aim of this study is to **investigate the patterns of the SST fronts in the CCS, with an emphasis on the fronts observed outside of the coastal upwelling framework.**

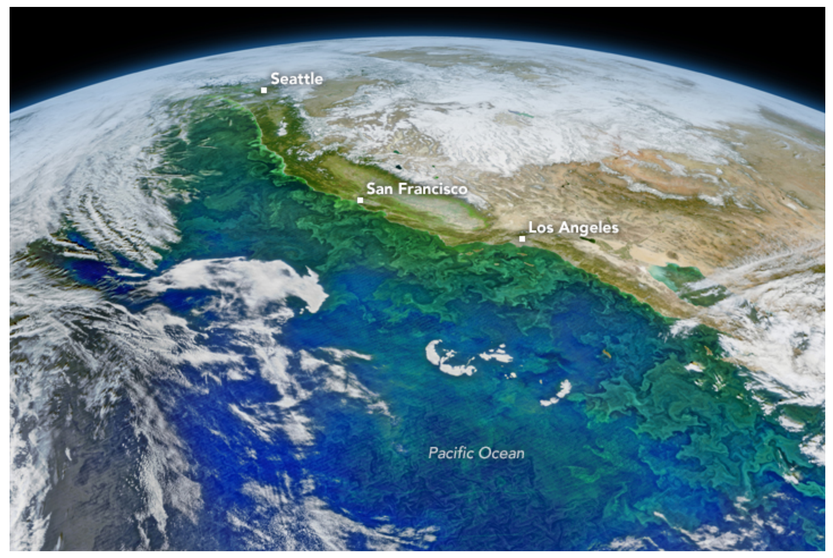

Fig. 1: Phytoplankton blooms off US West Coast, derived from VIIRS data. Credit**:** NASA image by Norman Kuring, NASA's Ocean Color Web.

2. Methodology

Satellite observations

- **SST data** Thermal fronts were detected from Pathfinder AVHRR (Advanced Very High Resolution Radiometer) Level-3 SST fields, with a spatial resolution of 4km.
- **SSH data** Sea level anomalies data is a multi-mission altimeter satellite Level-4 product, distributed by CMEMS (Copernicus Marine Service Information - formerly AVISO), and with a spatial resolution of ¼ degree.

Numerical simulations

- **LLC4320** Based on a Latitude/Longitude/polar-Cap (LLC) configuration of the MIT general circulation model, the numerical simulations have a horizontal resolution of 1/48º (nominally 2km).

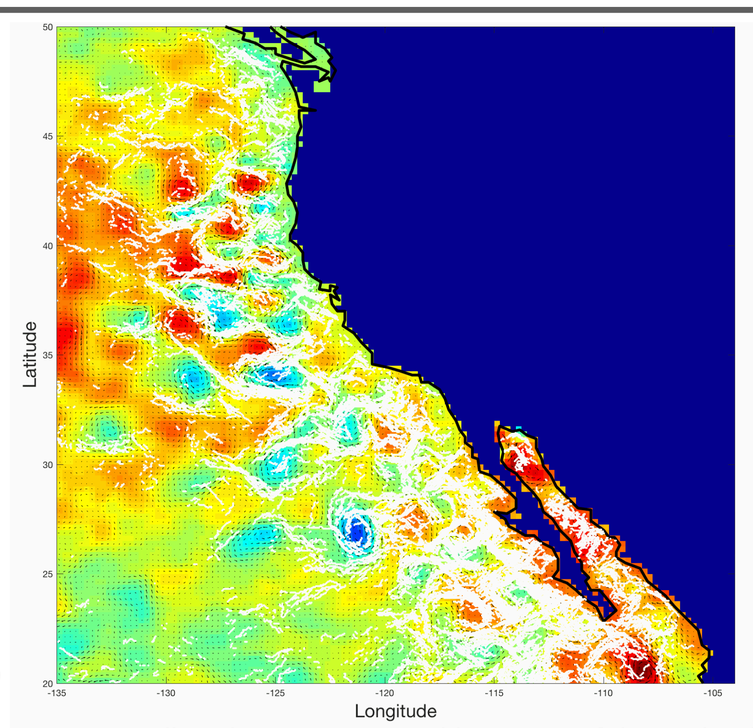

Fig. 2: Satellite observations: monthly average of the sea level anomaly (color field) + location of SST fronts detected over a month (white lines) - for the month of October 2008.

3. Results

Frontal patterns

- SST and SST fronts (black lines): SST fronts are observed in the southern CCS despite little coastal upwelling off Baja California.
- Density fronts (white lines) are plotted with SST fronts (black lines). Density fronts do not always coincide with temperature fronts in southern CCS.

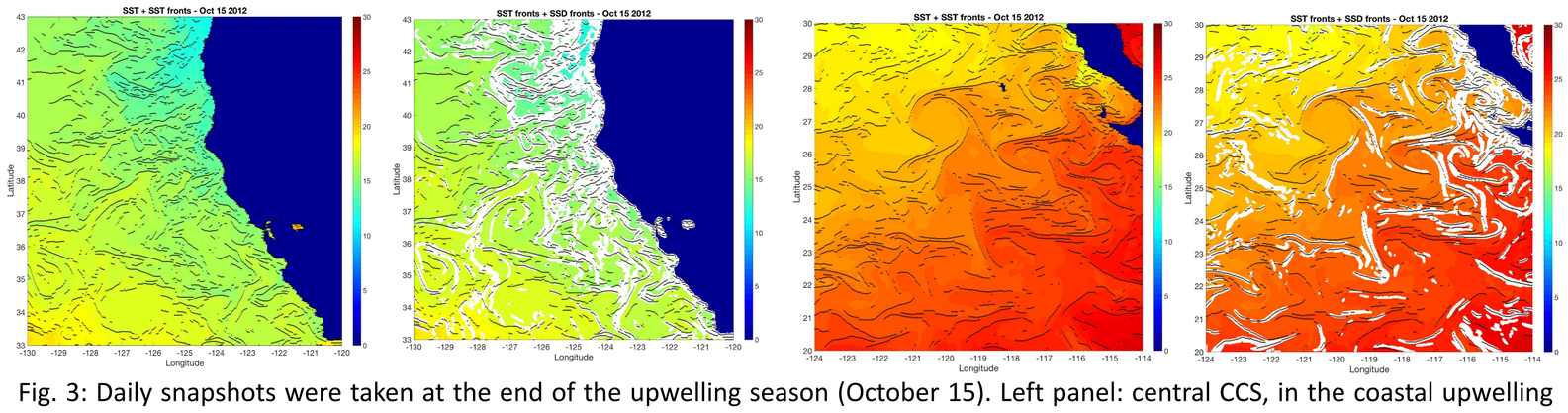

Fig. 3: Daily snapshots were taken at the end of the upwelling season (October 15). Left panel: central CCS, in the coastal upwelling region, right panel: southern CCS, outside the coastal upwelling region.

Frontal patterns

- Vertical velocities at 50m depth are much weaker in the southern CCS than in the central CCS.

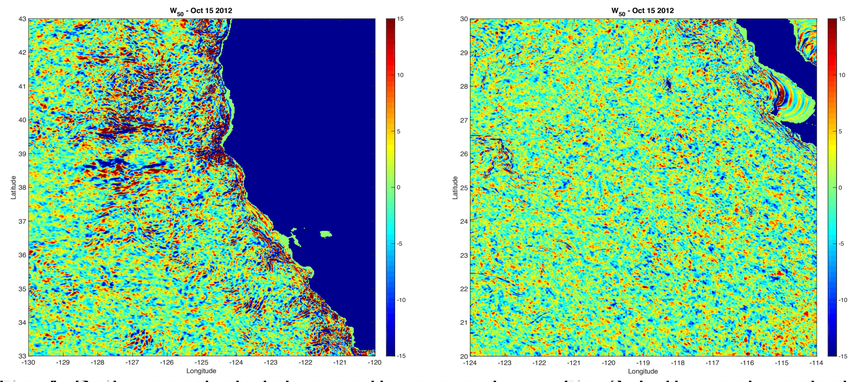

Fig. 4: Daily snapshots taken on the same day as Fig. 3. Left panel: central CCS, right panel: southern CCS.

Thermohaline compensation

Temperature and salinity gradients sometimes oppose each other's effects on density, resulting in little to no density gradients at the ocean's surface.

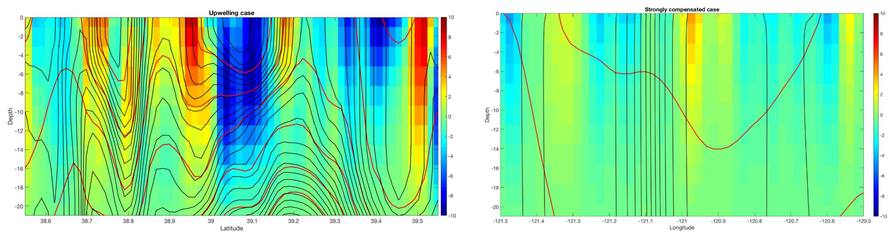

Fig. 5: Left panel: off California, upwelling case, with no compensation. Right panel: off Baja California, with compensation. Color field: vertical velocity, from -10/10m per day, taken over the first 20m depth. Black contours: isotherms. Red contours: isopycnals.

4. Conclusions

- Although coastal upwelling is the main process occurring in the CCS, frontal dynamics may not be explained fully through upwelling.
- Part of the fronts appear to be affected by thermohaline compensation, and exhibit distinct patterns: they behave as passive features, advected by the background flow; in contrast with the fronts observed in the coastal upwelling region which are active and contribute to the ocean biology and marine ecology off California.
- By combining various NASA satellite datasets (here altimetry and sea surface temperature), new science questions may emerge, which ultimately will expand our understanding of Earth's oceans.

National Aeronautics and Space Administration
Jet Propulsion Laboratory
California Institute of Technology
Pasadena, California

www.nasa.gov

CL#19-3514 **Poster No. EB-19**

National Aeronautics and Space Administration

How anomalous is contemporary ice mass loss in Southwest Greenland? Gaining a longer term perspective through model-data comparison.

Author: Joshua Cuzzone (329C-Affiliate)
Nicole Schlegel (329C), Mathieu Morlighem (329C), Eric Larour (329C)

1. Introduction

Motivation for work: ***Figure 1A:*** **Contemporary ice mass loss from the Greenland Ice Sheet (GrIS**). Short observational records provide limited context as to how anomalous contemporary ice mass loss is when compared to the longer term ice history.

Figure 1B: **Southwest GrIS Summertime (JJA) temperature anomaly from present day for the past 12,000 years.** Climate underwent significant changes during the past with periods up to 12ºC colder and 3ºC warmer than preindustrial.

How did SW Greenland respond to these climate variations during the past?

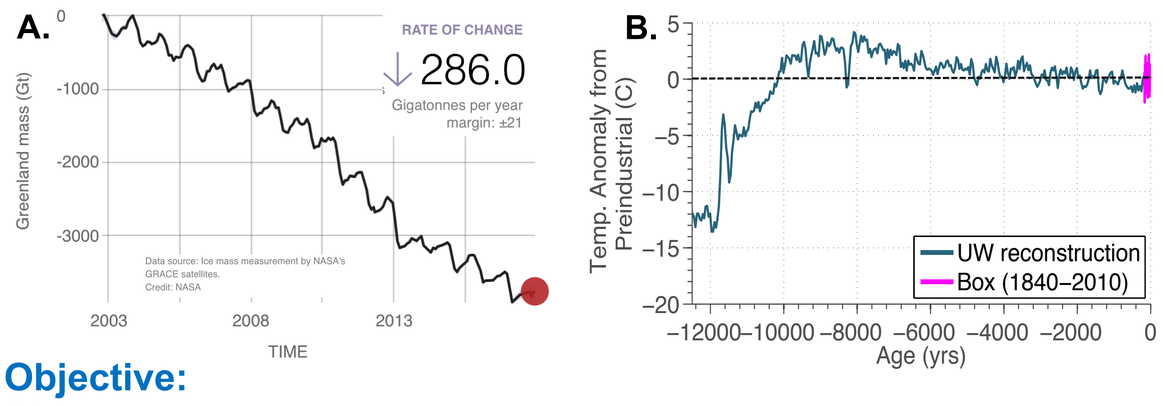

Objective:

1.) Model ice retreat across SW Greenland for the past 12,000 years using the Ice Sheet System Model (ISSM) and state-of-the-art climate reconstructions.
2.) Constrain the simulated retreat by the geologically reconstructed retreat.
3.) Infer ice mass loss across SW Greenland for the past 12,000 years and compare this with contemporary and projected ice mass loss for the same area.

2. Methods

1.) Observations: past ice retreat (Target for Ice Sheet Model):

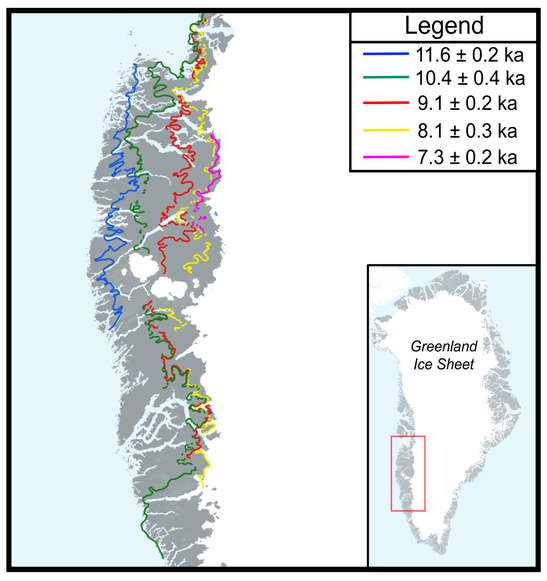

- We use geologic reconstructions** detailing the timing and spatial migration of the ice margin across SW Greenland. (Data was collected by our colleagues over the span of 3 field seasons)

Figure 2.
Ice retreat history across *SW* Greenland

- Colored lines indicate the ***time*** when ice retreated from the position shown in the map (***ka = thousand year***).

2.) Past climate reconstructions

- **A State-of-the-art** gridded temperature (***Figure 1B***) and precipitation dataset ^^ across Greenland for the last 12,000 years is used to drive the ice Sheet Model. It is derived using data assimilation that combines information from ice core records and coupled climate simulations of the past.

3.) Ice Sheet System Model (ISSM)

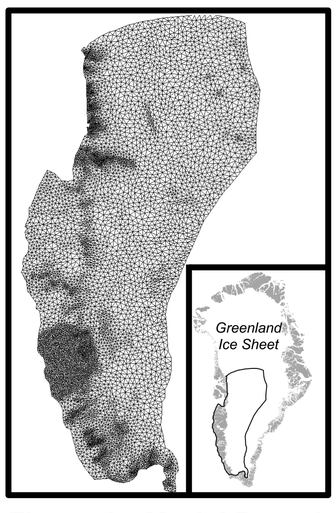

Figure 3: Model Domain

We use JPL's ice sheet model, ISSM.

- non-uniform mesh (**Figure 3**), with mesh resolution varying from 2 km to 20 km.
- Uses a Higher Order ice flow approximation.
- Ice temperature/rheology computed through time.
- Friction at the bed varies as a function of the simulated basal temperatures.
- Positive degree day model is used to construct the surface mass balance forcing through time.
- Simulations begin 12,000 years ago when the ice margin was located along the present day coastline and continue to 2012.

3. Results

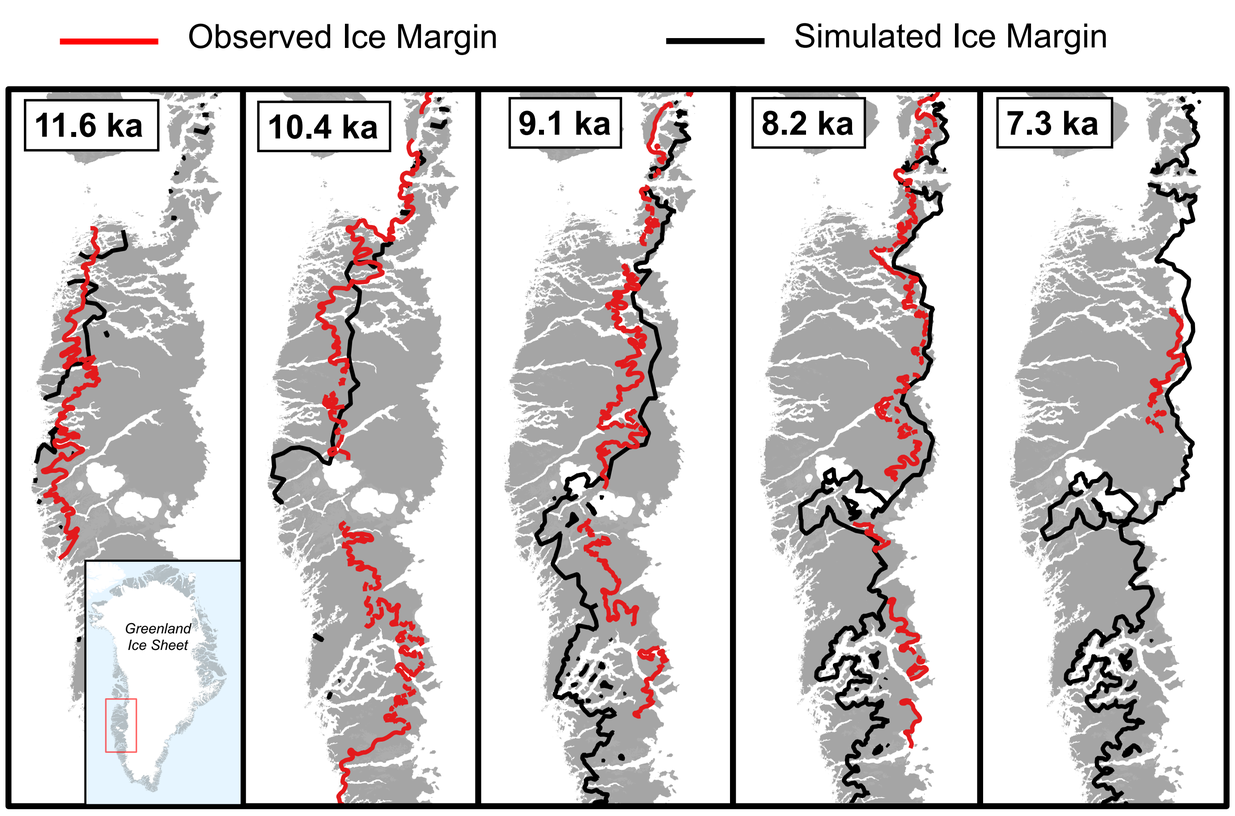

Figure 4. The extent and timing (***ka = thousand years***) of the simulated ice margin retreat (black line) shown against the reconstructed historical ice retreat (red line). Overall ISSM performs well, capturing the spatial and temporal retreat patterns providing confidence in determining the ice mass loss in this region over the past 12,000 years.

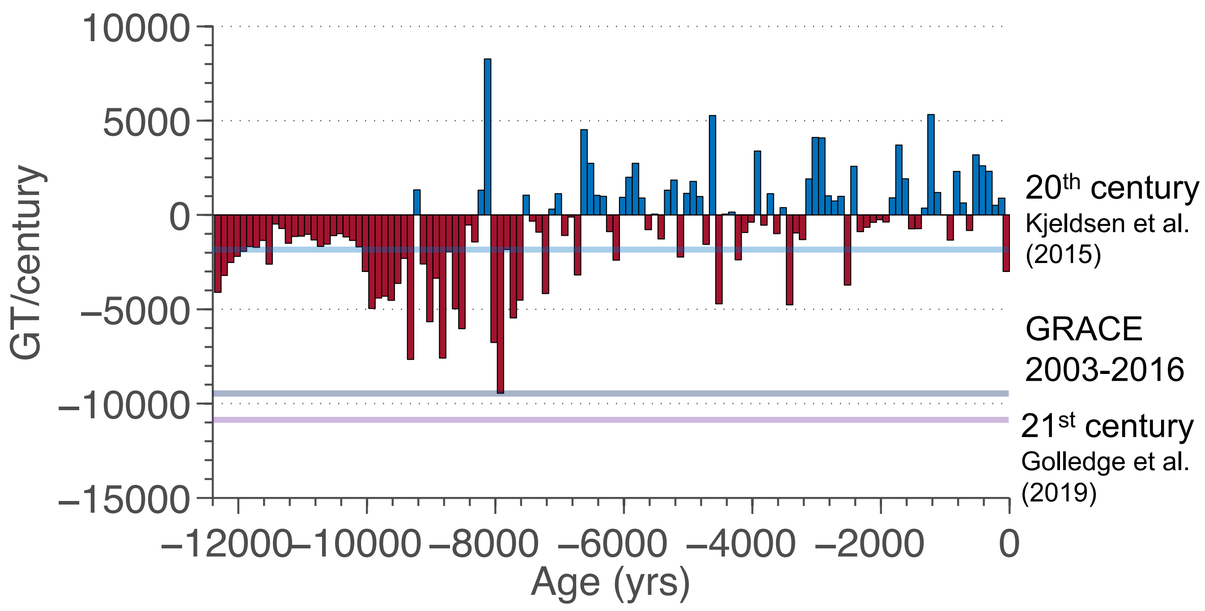

Figure 5. Simulated ice mass change (*GT/century*) over SW Greenland for the past 12,000 years. Ice mass loss (Red bars) and ice mass gain (Blue bars). Solid lines show contemporary estimates of ice mass loss over SW Greenland for the 20th century (1900-2010), 2003-2016 (GRACE), and for a 21st century simulation.

4. Conclusions

Contemporary ice mass loss over SW Greenland is at the fringe of the maximum ice loss experienced during the past 12,000 years.

- **Ice mass loss across SW Greenland during the remainder of the 21st century is expected to exceed the maximum ice mass loss over the past 12,000 years.**
- **Newly developed capabilities in ISSM has allowed for long term ice sheet simulations and opens new avenues towards computing past ice loading which will be beneficial for many applications at JPL (e.g. GRACE).**

National Aeronautics and Space Administration
Jet Propulsion Laboratory
California Institute of Technology
Pasadena, California
www.nasa.gov

Acknowledgments: We thank our colleagues **Jason Briner, Alia Lesnek, and Nicolas Young for providing geologic reconstructions of the past ice retreat. We thank our colleagues ^^ Jessica Badgeley, Eric Steig, and Greg Hakim for providing the gridded temperature and precipitation datasets used to force the ice sheet model through time.

The Cryosphere, 13, 879–893, 2019
https://doi.org/10.5194/tc-13-879-2019

The Cryosphere

The impact of model resolution on the simulated Holocene retreat of the southwestern Greenland ice sheet using the Ice Sheet System Model (ISSM)

Joshua K. Cuzzone[1,2], Nicole-Jeanne Schlegel[2], Mathieu Morlighem[1], Eric Larour[2], Jason P. Briner[3], Helene Seroussi[2], and Lambert Caron[2]

Geosci. Model Dev., 11, 1683–1694, 2018
https://doi.org/10.5194/gmd-11-1683-2018

Geoscientific Model Development

Implementation of higher-order vertical finite elements in ISSM v4.13 for improved ice sheet flow modeling over paleoclimate timescales

Joshua K. Cuzzone[1,2], Mathieu Morlighem[1], Eric Larour[2], Nicole Schlegel[2], and Helene Seroussi[2]

Poster No. EB-20

National Aeronautics and Space Administration

Acetonylperoxy and Hydroperoxy Kinetics from the Perspective of Hydroxyl Radicals

Author: Kristen Zuraski

Fred Grieman, Aileen Hui, Frank A. F. Winiberg, Carl J. Percival, Stanley P. Sander

Chemistry of Peroxy Radicals (RO_2) in the Troposphere

In the troposphere, atmospheric oxidation of volatile organic compounds leads to the formation of organic peroxy radicals (RO_2). Peroxy radicals play a vital role in the budgets of ozone, NO_x, NO_y and HO_x throughout the troposphere and the importance of these families in determining atmospheric composition, the earths radiative balance and any future change in climate cannot be over-emphasized. The major pathway of RO_2 + HO_2 is thought to be the hydroperoxide, ROOH. These generally have lifetimes of 1 day or longer where they work as a sink for HO_x radicals and thus mediate the oxidizing capacity of the troposphere.

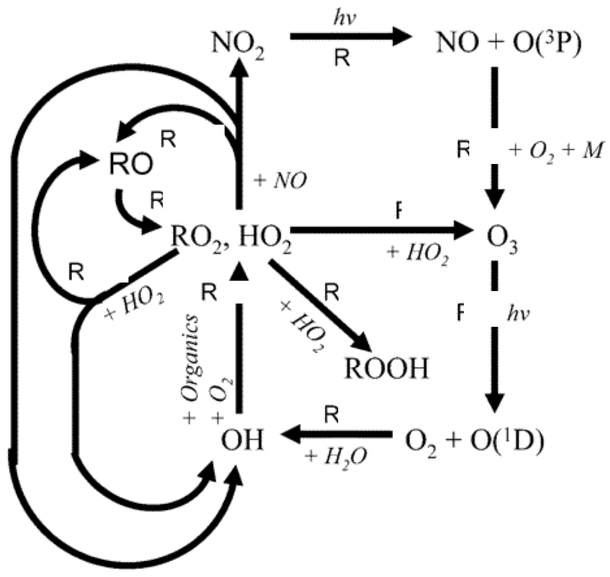

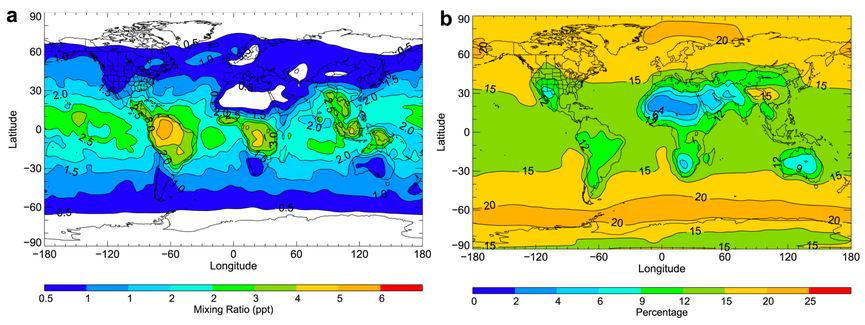

Role of water in RO_2 atmospheric chemistry

Recent theoretical work (STOCHEM models) suggests that 17% of organic peroxy radicals in the upper troposphere could be complexed with water. Water has been shown to effect the rate of these reactions.

Hasson, A.S.; Tyndall, G.S.; Orlando, J.J. *J. Phys. Chem. A,* **2004,** *108, 5979-5989*

Khan, M. A. H.; Cooke, M. C.; Utembe, S. R. ; Archibald, A. T. ; Derwent, R. G.; Jenkin, M. E.; Morris,W.C.; South, N.; Hansen, J. C.;Francisco, J. S.; Percival, C. J.; Shallcross, D. E. *Atmos Environ*, **2015**, *106*, 278–287

Project Objectives and Significance of Results

- Observe the kinetics and end-product ratios for the reaction between acetonylperoxy and hydroperoxy.
- Observe the effects of water on this reaction to aid in the overall understanding of the profound effects of water in atmospheric chemistry. This becomes increasingly important as the atmosphere continues to heat up and hold more water.
- These results will address key uncertainties in the NASA Data Evaluation database of kinetic parameters used by tropospheric models. These models are used in the analysis of atmospheric composition data from all past and present NASA suborbital missions and satellite instruments and missions. These include TOMS, UARS, TES, OMI, MLS, MOPITT, AIRS, DISCOVER-AQ, and future missions such as TEMPO and GEO-CARB. By expanding the basis of knowledge currently provided by the NASA Data Evaluation to account for parameter changes due to temperature and humidity levels, substantial progress will be made that is congruent with the NASA Science Plan and Atmospheric Composition program objectives.

Reactions of Interest

In low NO_x/high HO_x environments, acetone is among the most abundant oxygenated VOC. Following oxidation of acetone to form acetonylperoxy, reactions with HO_2 impact the HO_x balance by removing HO_2 and working as a HO_X radical sink through the formation of hydroperoxides or the generation of hydroxyl radicals (OH):

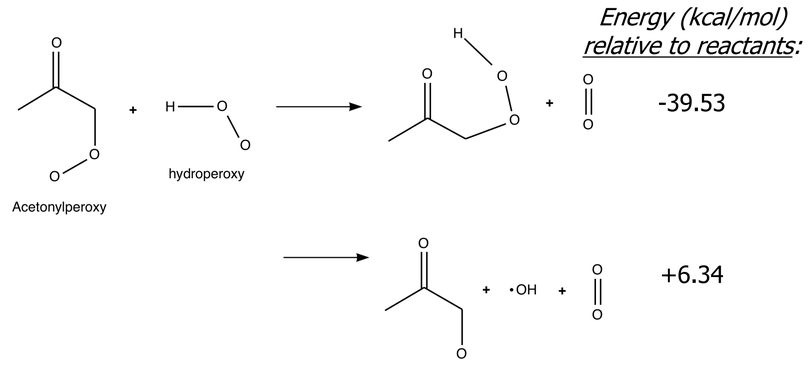

The ROOH channel is expected to be dominate. However, despite the OH channel being endothermic, theory demonstrated that hydrogen bonding in the carbonyl group of acetonylperoxy stabilizes the hydrotetroxide intermediate that can lead to OH formation.

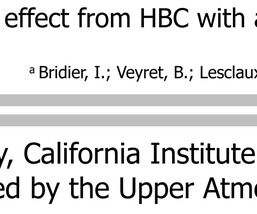

The strong effect of hydrogen bonding on the product yields reinforces the need to investigate the water dependence for the reaction. There are currently no previous studies involving water and this reaction.

Hasson, A. S.; Kuwata, K. T.; Arroyo, M. C.; Peterson, E. B. *J. of Photochem. and Photobio. A: Chemistry* **2005**,*176,* 218-230.

Experimental Methods:

Hydroperoxy and acetonlyperoxy radicals are generated by reaction of chlorine atoms with methanol and acetone, respectively, followed by an addition reaction with O_2

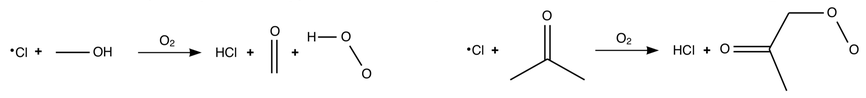

The setup achieves simultaneous detection of HO_2, OH, and acetonylperoxy radicals through the use of two infrared diode lasers and an ultraviolet laser driven light source (LDLS), respectively. The infrared lasers make thirty passes through the cell using Herriot-type optics and have further increased detection sensitivity by utilizing frequency modulated (FM) spectroscopy.

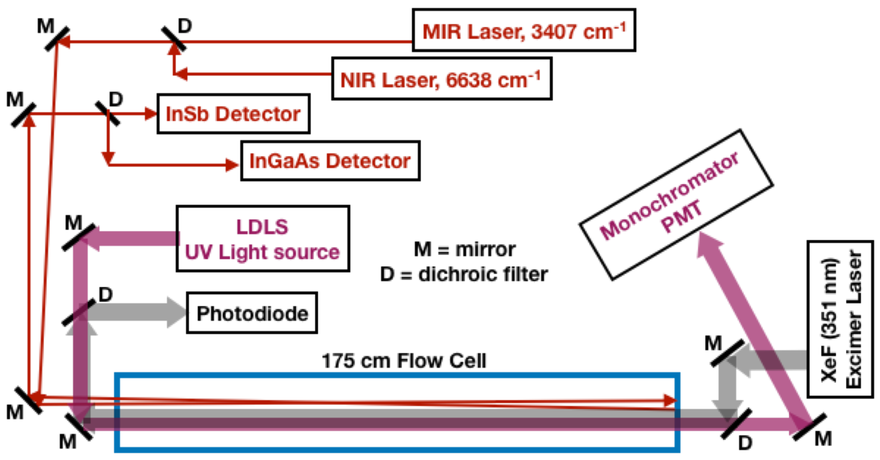

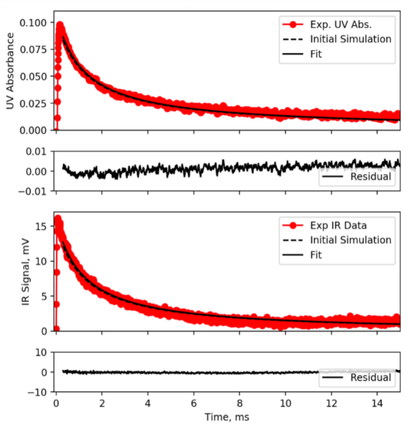

The NIR laser is calibrated using known reactions, HO_2 + HO_2, in comparison to the UV absorption of HO_2 (example shown above). The MIR laser is then calibrated using the known reaction, HO_2 + NO, with the comparison to the HO_2 decay and a modeled fit for the reaction.

Preliminary Results:

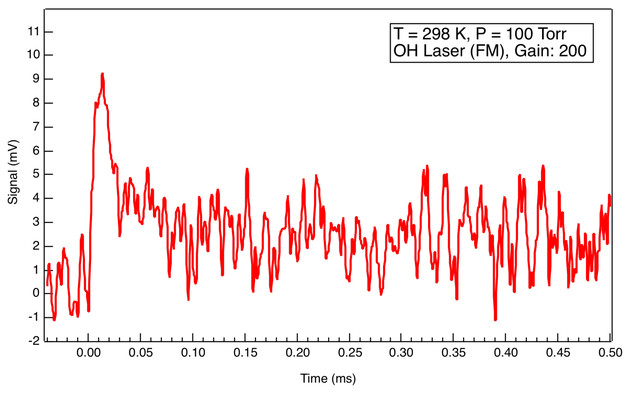

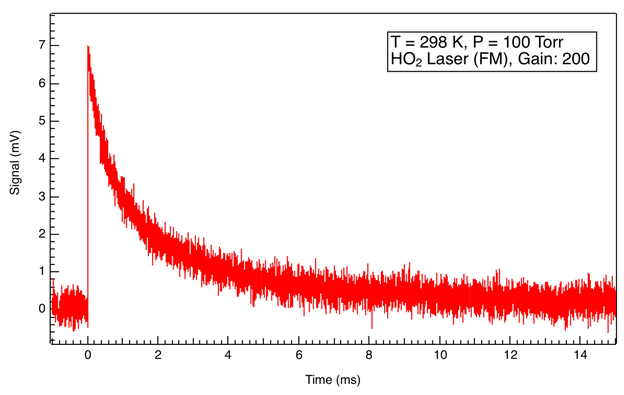

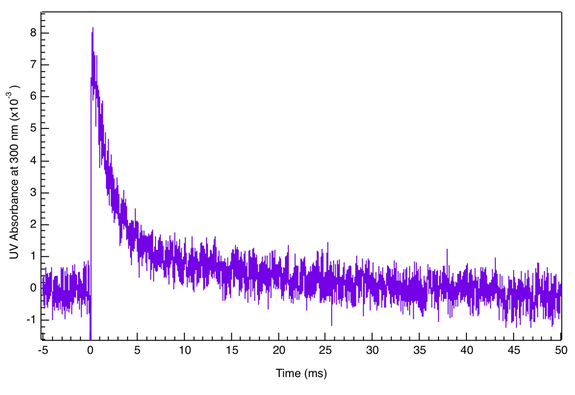

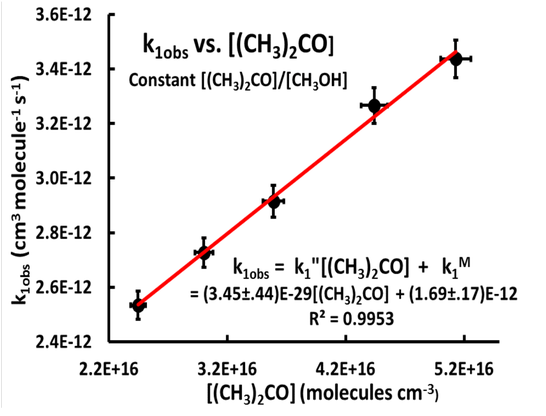

Table of Room Temperature Results:

Parameter	Recommended	This work (in progress)
Acetonylperoxy self-rxn rate	[a](9.0 ± 1.0) x 10^{-12}	(5.9 ± 0.9) x 10^{-12}
HO_2 + Acetonylperoxy Rate	[a](9.0 ± 1.0) x 10^{-12}	(3.0 ± 0.45) x 10^{-12}
Branching Ratio for OH formation	Ranges from 15–67 %	*Under investigation*

* Rates expressed in cm^3 $molecule^{-1}$ s^{-1}

The Chaperone Effect:

An increase in the HO_2 decay is observed as a result of the formation of hydrogen bond complexation (HBC) with HO_2 to form HO_2-CH_3OH and HO_2-$CH_3C(O)CH_3$. Accounting for this loss in modeling/fitting the data is critical in order to extract accurate rate constants and branching ratios for the reaction. The HBC with methanol was expected, however, the strong effect from HBC with acetone was unexpected prior to this study.

[a] Bridier, I.; Veyret, B.; Lesclaux, R.; Jenkin, M. E. *Chem. Soc., Faraday Trans.* **1993**, *89*, 2993-2997.

National Aeronautics and Space Administration

Jet Propulsion Laboratory
California Institute of Technology
Pasadena, California

Acknowledgements: This research was carried out at the Jet Propulsion Laboratory, California Institute of Technology, under a contract with National Aeronautics and Space Administration (NASA). Financial support was provided by the Upper Atmosphere Research and Tropospheric Chemistry programs and the NASA Postdoctoral Program.

www.nasa.gov

Poster No. EB-21